Dynamic Analysis of Multiply Connected Bodies for Magnetic Resonance Elastography

BY

Benjamin L. Schwartz
B.S.E. Arizona State University 2006
M.S. University of Vermont 2009

THESIS

Submitted as partial fulfillment of the requirements
for the degree of Doctor of Philosophy in Bioengineering
in the Graduate College of the
University of Illinois at Chicago, 2014

Chicago, Illinois

Defense Committee:

Richard L. Magin, Ph.D., Chair and Advisor
Thomas J. Royston, Ph.D.
James L. Patton, Ph.D.
Urmila M. Diwekar, Ph.D.
Jun Cheng, Ph.D.

To Leon, Ethel, Harry, and Taki

ACKNOWLEDGMENTS

None of this would have been possible without the cooperation of some really great scientists and engineers whom I'm also privileged to call my friends. They are Ziying, Allen, Altaf, Yifei, mon capitaine Kaya, Aman, Steve, Nagehan, Zoujun, Ying, Amelia, and Shan. My students probably taught me the most. They are Vivian, Lora, Kelley, Heta, Lara, and Kruti.

I offer many thanks to those who took the time to evaluate my work on behalf of the university as a committee member or otherwise. They are Urmila Diwekar, Jim Patton, Maj. Tom Royston, Percival McCormack, Rob Kleps, and Jun Cheng. Special mention goes to my mentor and reason I came to UIC in the first place, Richard Magin.

Three friends with whom I struggled through many classes are Moria, Carson, and Laura-Jane. Your friendships mean more to me than any degree. I made friends ourside of class, too, i.e. Sam, Josh, and John. I'll not forget Jessica, Susan, Jay, and Łukasz. You are the reason the department functions at all.

The most important part of campus, though, is the Port Center Cafe. Thanks go to all the staff, especially Elle, Kylie, Maura, and Monica. I have been honored to call the coolest gentlemen in all Chicago my friends. They are Eli and Trevor.

I certainly couldn't have survived the Midwest, so distant from my beloved Sonoran Desert, without the cheers from back home. That chorus includes Mayo, Mickey, Meg, The Hoe, Monsieur Brown, The Beatlnik, Carla, WillBabe, The Glass Vernagerie, Little Lindsey, Katie, Jessica, B-rad, Maggie, Debbie, Monsieur Malone, Beeca, Joe, Pauli, Elizabeth, Genie, The

ACKNOWLEDGMENTS (Continued)

Phactor, Kristen, WernDogg, Thew, Clemi, BigWill, Colleen, Egg, Heather, Mr., Sara, Mick, Meathead Dave, Katey, Ben, Peter, Chris, Jake, Tanesha, Nick, Katie the Thrash Compactor, Lady Becca & Chris, Nirav the ILM, Lady Ana & Gentle Joseph, & Baby Thomas, Chris & Kate, Veronica & Ralph, the three wise men of Vermont: Jason, Jeff, and Peter, GoodWalten, Max, Crocker, the three wise men from ASU: Jit, Mike, and Vince. I would be remiss if I didn't mention my friend Takayori Ataumi, one of the greatest teachers to ever live and one of four to whom this work is dedicated. The other dedicatees are my Opa Leon, Grandma Ethel, and Grandpa Harry.

My family is as important to me as my friends. I'm lucky to have a large and supportive one. Thanks go to Aunt Judy & Uncle Tony, Aunt Carolyn & Uncle Joe, Aunt Adonna, Aunt Robin, Aunt Mimi, Aunt Leonette, and Aunt Marla & Uncle Arnie. Thanks go to Megan & Daniel, Michael, Aimee & Toivo, Geoff, Barbara, Clifford & Camille, Kathleen, Jonathan, Donna Marie, Tonya, Anthony, Gina, Lindsey, Brendan, Rena & Michael, and Alex. I am proud to be an uncle to Dariane, Sara, and Ryan. My brothers and sisters are Pami & Joe, Alison & Graham, Jack, Karen & Dave, Amanda, and Ian. My momme & dadde are Pamela & Albert, and my oma is Maxine. I've missed you all so very much.

BLS

TABLE OF CONTENTS

TABLE OF CONTENTS (Continued)

CHAPTER **PAGE**

LIST OF TABLES

LIST OF FIGURES

LIST OF FIGURES (Continued)

FIGURE **PAGE**

LIST OF FIGURES (Continued)

LIST OF FIGURES (Continued)

LIST OF ABBREVIATIONS

MRI	magnetic resonance imaging
MRE	magnetic resonance elastography
μMRE	microscopic scale MRE
SE	spin-echo
MSG	motion-sensitizing gradient
TR	repetition time
TE	echo time
FOV	field of view
LFE	local frequency estimation
ROI	region of interest

SUMMARY

This work centers around the design, manufacturing, analysis, and experimental use of hydrogel phantoms in magnetic resonance elastography. The first chapter is an introduction to some basic concepts in engineering math and medical imaging that the reader might find useful to understand the rest of the work. In the second chapter, the solution to a concentric cylindrical body undergoing harmonic oscillations is derived. Then the phantom construction, experimental procedure, parameter estimation, and the forward problem are described. To validate the model, the shear moduli estimates are used as inputs to solve the forward problem with a finite element model (FEM) which is compared with experimental results. The immediate consequences of this work as well its implications for future research are considered. In the third chapter, the scattering and diffraction of a cylindrically converging transverse shear wave in a viscoelastic isotropic medium by a spherical heterogeneity is analytically solved. The wave field is determined for a hydrogel bead suspended in a different hydrogel that fills a glass test tube. Numerical examples showing the effect on displacement fields of varying the stiffness of the inclusion are presented. The fourth chapter is very similar to the second chapter, save that the phantom has a spherical heterogeneity rather than a concentric cylinder. Further, only the results of the forward problem are compared to the experiment to validate the mathematical model. The concluding chapter re-states what has preceded it, ending with some remarks on future work. The works cited section includes every source referenced in this document. Finally, my vita describes my educational history as well as my publications.

CHAPTER 1

PRELUDE

The natural world is a vast and mysterious place that could be described, not incorrectly, as having an infinite complexity on all levels, domains, scales, ranges, aspects, times, perspectives, etc. Those who call themselves scientists, engineers, mathematicians–philosophers, in short–have taken on the charge of solving these mysteries and then communicating these knowledges that all may benefit and that some may even follow suit, building on what spoke to their individual passions. I wish to join the august society of natural philosophers. I offer, then, this document as proof of my ability to do good science, and to contribute to the body of work that is the collective knowledge of all humanity. My favorite subjects in grade school were math, biology, chemistry, and physics. Bioengineering and imaging in particular seemed to encapsulate all four most equally. The three studies herein center around the art of mathematical modeling the dynamic behavior of materials designed to be not unlike living tissue. Through these pen-and-paper analyses we glean insights about the composition and interaction of these tissue-mimicking substances and, by extension, our own flesh and blood. The first study is about an object made of two concentric cylinders of different composition and stiffness. The second study is the mathematical framework for a sphere encased in a cylinder. The third study is the experimental work that uses the analyses of the second study. Before all that, though, is some background information about the math, imaging techniques, and materials used in all the studies. Those already familiar with the vector wave equation, magnetic resonance imaging

and elastography, and hydrogels can probably skip the rest of this chapter, going straight to the novel work. And now let us begin.

1.1 Mathematic Preliminaries

All too often I found a paper on vibrations that relied heavily on math that the reader was just assumed to have known. I never want to be such an author. At the very least, I won't start now. What follows is a description with some derivations, of the math used in this work. It is not meant to be a rigorous treatment, but a general summary with an intuitive tone, that you may understand the tool used throughout.

1.1.1 The Wave Equation

In the vibrations of solids let us define the displacement vector, $\vec{U}$, as

$$\vec{U} = u\hat{x}_1 + v\hat{x}_2 + w\hat{x}_3 \tag{1.1}$$

where u, v, and w are the magnitudes along three orthogonal unit vectors, $\hat{x}_i$. In this work, we focus on the cylindrical (ρ, ϕ, z) and spherical coordinates (r, θ, ϕ), depicted in Figure 1 and Figure 2, respectively. In cylindrical coordinates, Equation 1.1 becomes

$$\vec{U}(\rho, \theta, z) = u_\rho\hat{\rho} + u_\phi\hat{\phi} + u_z\hat{z}, \tag{1.2}$$

and, in spherical coordinates,

$$\vec{U}(r, \theta, \phi) = u_r\hat{r} + u_\theta\hat{\theta} + u_\phi\hat{\phi}. \tag{1.3}$$

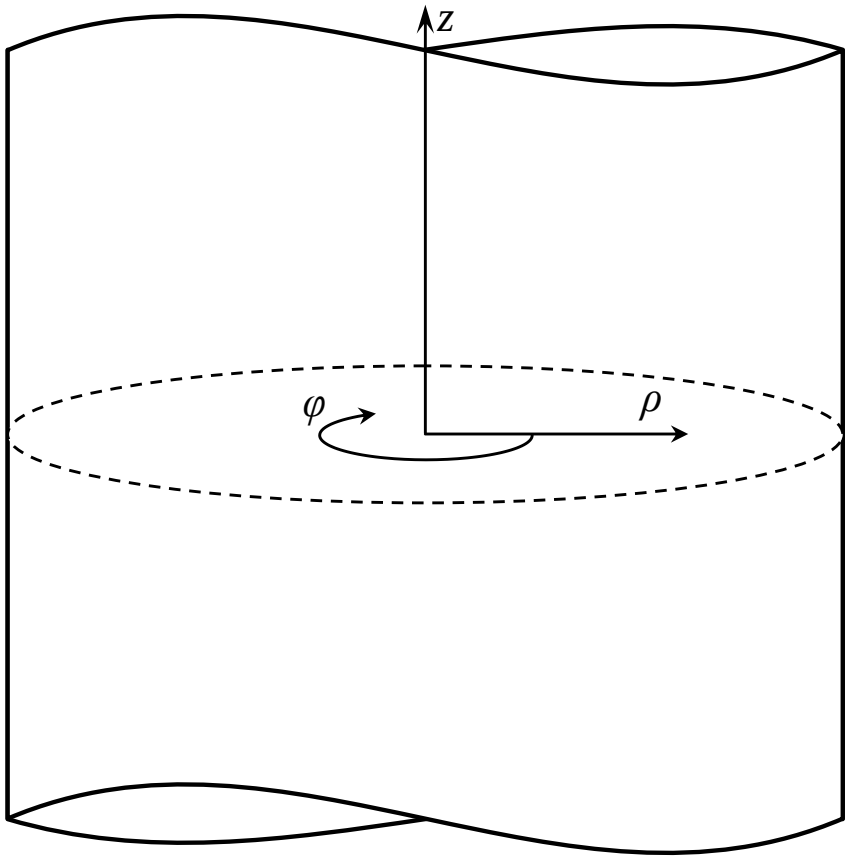

Figure 1. Cylindrical Coordinates

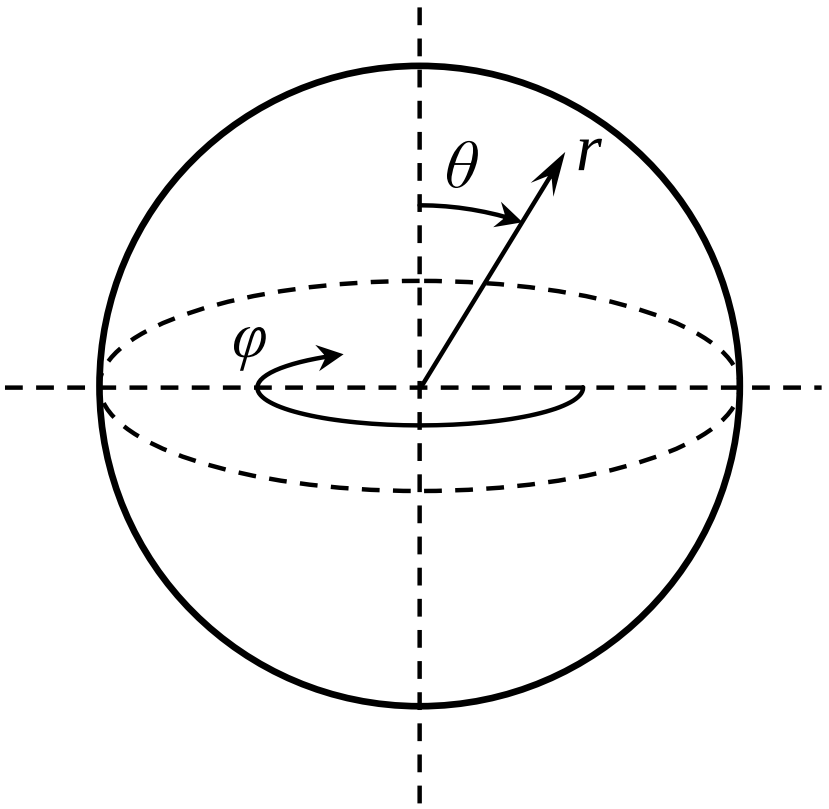

Figure 2. Spherical Coordinates

Suppressing time dependence, the governing equation for a homogeneous isotropic elastic solid is a linear, second-order, partial, differential equation, given, in terms of displacement, in vector notation as (1)

$$\alpha^2 \nabla\nabla \cdot \vec{U} - \beta^2 \nabla \times \nabla \times \vec{U} + \omega^2 \vec{U} = 0. \tag{1.4}$$

Here α and β are, respectively, the longitudinal and transverse wave speeds, given, in terms of the elastic material constants (the Lamé constants), λ and μ, as

$$\alpha^2 = \frac{\lambda + 2\mu}{\gamma} \tag{1.5}$$

and

$$\beta^2 = \frac{\mu}{\gamma}, \tag{1.6}$$

where γ, due to obvious notational constraints, is the material density. The second Lamé constant, μ, is also called the shear modulus, and ω is the angular frequency of vibrations. To solve for $\vec{U}$, we turn to the fundamental theorem of vector calculus, also called Helmholtz decomposition, which states that a vector field may be decomposed into longitudinal and transverse components (1), called vector potential functions, and given as

$$\vec{U} = \nabla\Phi + \nabla \times \hat{e}\Psi + \beta_i^{-1} \nabla \times \nabla \times \hat{e}\mathrm{X}. \tag{1.7}$$

The first term on the right side of Equation 1.7 is the longitudinal component and the second and third terms are the transverse components. The constant vector, $\hat{e}$, in Equation 1.7 depends on the coordinate system, as do the gradient and curl operators.

Let there be given a scalar function of three orthogonal coordinates, $\mathfrak{f}(x_1, x_2, x_3)$, and vector function, also of three orthogonal coordinates, $\vec{\mathfrak{F}}(x_1, x_2, x_3)$. In cylindrical coordinates the gradient and curl operations on $\mathfrak{f}$ and $\vec{\mathfrak{F}}$, respectively, are given as

$$\nabla \mathfrak{f}(\rho, \phi, z) = \frac{\partial \mathfrak{f}(\rho, \phi, z)}{\partial \rho}\hat{\rho} + \frac{1}{\rho}\frac{\partial \mathfrak{f}(\rho, \phi, z)}{\partial \phi}\hat{\phi} + \frac{\partial \mathfrak{f}(\rho, \phi, z)}{\partial z}\hat{z}, \tag{1.8}$$

and

$$\nabla \times \vec{\mathfrak{F}}(\rho, \phi, z) = \left(\frac{1}{\rho}\frac{\partial \mathfrak{f}_z}{\partial \phi} - \frac{\partial \mathfrak{f}_\phi}{\partial z}\right)\hat{\rho} + \left(\frac{\partial \mathfrak{f}_\rho}{\partial z} - \frac{\partial \mathfrak{f}_z}{\partial \rho}\right)\hat{\phi} + \left(\frac{1}{\rho}\frac{\partial}{\partial \phi}\left(\rho \mathfrak{f}_\phi\right) - \frac{1}{\rho}\frac{\partial \mathfrak{f}_\rho}{\partial \phi}\right)\hat{z}. \tag{1.9}$$

In spherical coordinates, Equation 1.8 and Equation 1.9 become

$$\nabla \mathfrak{f}(r, \theta, \phi) = \frac{\partial \mathfrak{f}(r, \theta, \phi)}{\partial r}\hat{r} + \frac{1}{r}\frac{\partial \mathfrak{f}(r, \theta, \phi)}{\partial \theta}\hat{\theta} + \frac{1}{r\sin(\theta)}\frac{\partial \mathfrak{f}(r, \theta, \phi)}{\partial \phi}\hat{\phi}, \tag{1.10}$$

and

$$\nabla \times \vec{\mathfrak{F}}(r, \theta, \phi) = \frac{1}{r\sin(\theta)}\left(\frac{\partial}{\partial \theta}\left(\mathfrak{f}_\phi \sin(\theta)\right) - \frac{\partial \mathfrak{f}_\theta}{\partial \phi}\right)\hat{r} + \left(\frac{1}{r\sin(\theta)}\frac{\partial \mathfrak{f}_r}{\partial \phi} - \frac{1}{r}\frac{\partial}{\partial r}\left(r\mathfrak{f}_\phi\right)\right)\hat{\theta}$$

$$+\frac{1}{r}\left(\frac{\partial}{\partial r}\left(r\mathfrak{f}_\theta\right) - \frac{\partial \mathfrak{f}_r}{\partial \theta}\right)\hat{\phi}. \tag{1.11}$$

The scalar potentials, Φ, Ψ, and X, each solves the scalar helmholtz equation (1), i.e.

$$\left(\nabla^2 + \frac{\omega}{\alpha^2}\right)\Phi = 0 \tag{1.12a}$$

$$\left(\nabla^2 + \frac{\omega}{\beta^2}\right)\Psi = 0 \tag{1.12b}$$

$$\left(\nabla^2 + \frac{\omega}{\beta^2}\right)\mathrm{X} = 0. \tag{1.12c}$$

Like the gradient and curl operations, the Laplacian operation depends on the coordinate system. Using, once again, the example of the scalar function, $\mathfrak{f}$, expressions for the Laplacian are given, respectively, in cylindrical and spherical coordinates (2) as

$$\nabla^2\mathfrak{f}(\rho,\phi,z) = \frac{\partial^2\mathfrak{f}(\rho,\phi,z)}{\partial\rho^2} + \frac{1}{\rho}\frac{\partial\mathfrak{f}(\rho,\phi,z)}{\partial\rho} + \frac{1}{\rho^2}\frac{\partial^2\mathfrak{f}(\rho,\phi,z)}{\partial\phi^2} + \frac{\partial^2\mathfrak{f}(\rho,\phi,z)}{\partial z^2} \tag{1.13a}$$

$$\nabla^2\mathfrak{f}(r,\theta,\phi) = \frac{1}{r^2}\frac{\partial}{\partial r}\left(r^2\frac{\partial\mathfrak{f}(r,\theta,\phi)}{\partial r}\right) + \frac{1}{r^2\sin(\theta)}\frac{\partial}{\partial\theta}\left(\sin(\theta)\frac{\partial\mathfrak{f}(r,\theta,\phi)}{\partial\theta}\right) + \frac{1}{r^2\sin^2(\theta)}\frac{\partial^2\mathfrak{f}(r,\theta,\phi)}{\partial\phi^2}. \tag{1.13b}$$

1.1.2 Scalar Helmholtz Equation

Continuing with our sample function, $\mathfrak{f}(\rho,\phi,z)$, in cylindrical coordinates, the scalar helmholtz equation is given as

$$\left(\nabla^2 + \frac{\omega}{c^2}\right)\mathfrak{f}(\rho,\phi,z) = 0, \tag{1.14}$$

where c stands for the appropriate–longitudinal or transverse–wave speed. The circular cylindrical coordinate system is separable in the helmholtz equation (2) which means that we may

solve Equation 1.14 by the method of separation of variables (3), wherein we assume that the function, in this case $\mathfrak{f}(\rho, \phi, z)$, is a product of three functions, each of only one coordinate, i.e.

$$\mathfrak{f}(\rho, \phi, z) = P(\rho)\Phi(\phi)Z(z). \tag{1.15}$$

The method of separation of variables is a powerful tool because it allows us to transform a partial differential equation into multiple ordinary differential equations. All systems in this work are assumed to be axially symmetric so we will neglect any dependence on ϕ, making Equation 1.15

$$\mathfrak{f}(\rho, z) = P(\rho)Z(z). \tag{1.16}$$

Putting Equation 1.16 into Equation 1.14 gives us

$$\frac{1}{P(\rho)}\frac{\partial^2 P(\rho)}{\partial \rho^2} + \frac{1}{\rho P(\rho)}\frac{\partial P(\rho)}{\partial \rho} + \frac{1}{Z(z)}\frac{\partial^2 Z(z)}{\partial z^2} + \frac{\omega^2}{c^2} = 0. \tag{1.17}$$

We can isolate terms based on their variable, introducing a constant of separation, ν, which we square for analytic convenience,

$$\frac{1}{P(\rho)}\frac{\partial^2 P(\rho)}{\partial \rho^2} + \frac{1}{\rho P(\rho)}\frac{\partial P(\rho)}{\partial \rho} + \frac{\omega^2}{c^2} = -\frac{1}{Z(z)}\frac{\partial^2 Z(z)}{\partial z^2} = \nu^2. \tag{1.18}$$

We now have two linear, second order, ordinary differential equations. The radial equation is

$$\frac{\partial^2 P(\rho)}{\partial \rho^2} + \frac{1}{\rho}\frac{\partial P(\rho)}{\partial \rho} - \nu^2 P(\rho) = 0, \tag{1.19}$$

and the axial equation is

$$\frac{\partial^2 Z(z)}{\partial z^2} + \left(\frac{\omega^2}{c^2} + \nu^2\right) Z(z) = 0. \tag{1.20}$$

Equation 1.19 is the cylindrical Bessel equation, the solution to which is called the cylindrical Bessel function (4) and given as

$$P(\rho) = J_\nu\left(\frac{\omega}{c}\rho\right) = \sum_{m=0}^{\infty}(-1)^m \frac{1}{m!\Gamma(\nu+m+1)}\left(\frac{\frac{\omega}{c}\rho}{2}\right)^{2m+\rho}, \tag{1.21}$$

where Γ is the Gamma function (4). It is conventional to use J_ν to indicate the cylindrical Bessel function of the first kind of order ν. Because we get Bessel's equation when dealing with cylindrical coordinates, Bessel functions are sometimes referred to as cylindrical functions. The solution to Equation 1.20 is given as

$$Z(z) = \sin(\nu z) + \cos(\nu z). \tag{1.22}$$

In spherical coordinates, Equation 1.16 becomes

$$\mathfrak{f}(r,\theta) = R(r)\Theta(\theta), \tag{1.23}$$

and, after separating variables, we get a radial equation and an angular equation,

$$\frac{\partial}{\partial r}\left(r^2\frac{\partial R(r)}{\partial r}\right) + \frac{\omega^2}{c^2}r^2 R(r) - \nu(\nu+1)R(r) = 0, \tag{1.24}$$

and

$$\frac{\partial}{\partial\theta}\left(\sin(\theta)\frac{\partial\Theta(\theta)}{\theta}\right)+\nu(\nu+1)\Theta(\theta)\sin(\theta)=0, \tag{1.25}$$

respectively. For analytic convenience we chose $\nu(\nu+1)$ as the separation constant. Equation 1.24 is the spherical Bessel equation whose solution is defined in terms of the cylindrical Bessel function,

$$R(r)=j_\nu\left(\frac{\omega}{c}r\right)=\sqrt{\frac{\pi}{2\frac{\omega}{c}r}}J_{\nu+\frac{1}{2}}\left(\frac{\omega}{c}r\right). \tag{1.26}$$

Conventionally, the spherical Bessel function is written with a lower case, j. The solution to Equation 1.25 is called the Legendre polynomial of order ν,

$$\Theta(\theta)=P_\nu(\cos(\theta))=\sum_{m=0}^{\frac{\nu}{2}}(-1)^m\frac{(2\nu-2m)}{2^\nu m!(\nu-m)!(\nu-2m)!}\cos(\theta)^{\nu-2m}. \tag{1.27}$$

1.2 Imaging

The dynamic analysis of this work is for validation and other use in medical imaging. The modalities concerned are magnetic resonance imaging and a specialized technique thereof called magnetic resonance elastography. I'll, very briefly, describe them here. Much more thorough treatments can easily be found in the literature. I recommend the text by Smith and Webb (5).

1.2.1 Magnetic Resonance Imaging

A magnetic resonance imaging (MRI) scanner has one super-conducting magnet surrounding a cylindrical bore that produces the main magnetic field, B_0, that has a magnitude of $1.5-3$ tesla in most clinical scanners (we used a 9.4 tesla animal scanner for our data collection).

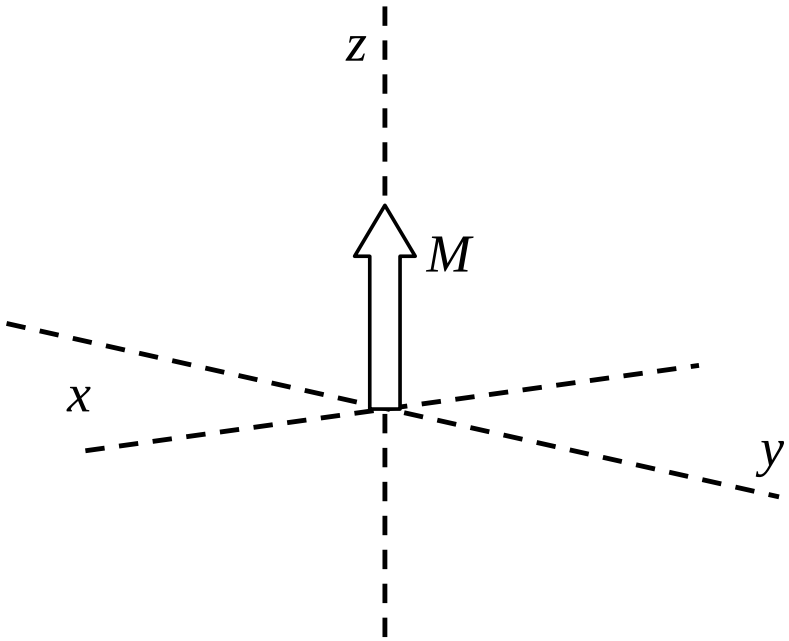

Figure 3. Vector model

There are two more magnetic fields induced by coils, the radio frequency (RF) and gradient. Once an object in question is in the field, it's protons begin to precess around the main field, according to the Bloch equation (5). Summing the vectors of all the magnetic moments of the protons we get one vector oriented along the B_0 vector, shown in Figure 3. RF coils apply another magnetic field whose principal components are perpendicular to the B_0 field and the induced torque tips the magnetization vector to the transverse plane, shown in Figure 4. The RF field is stopped and the protons begin to relax, first de-phasing and then re-aligning

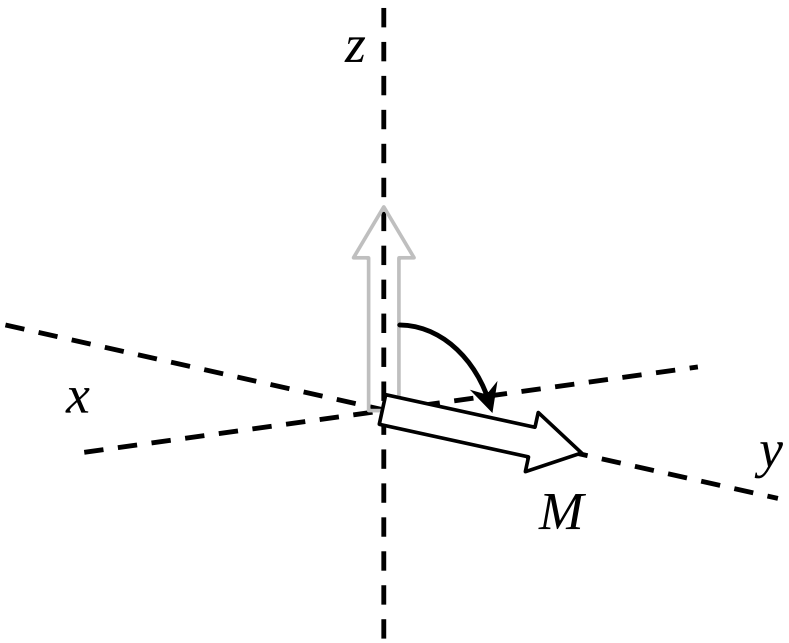

Figure 4. Tipping

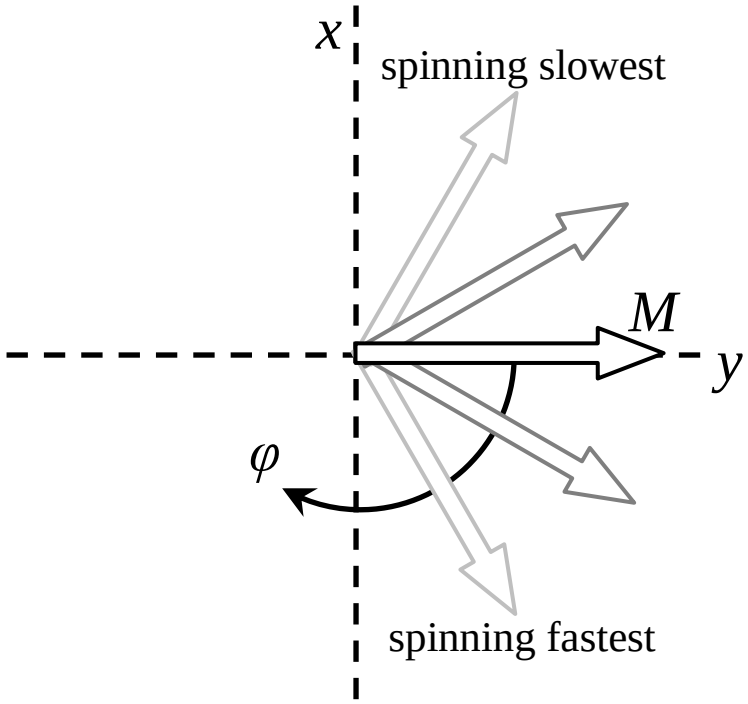

Figure 5. Dephasing

with the B_0. The view of vectors in Figure 3 and Figure 4 assumed a rotating reference frame, allowing us to visualize the dephasing. The magnetization vector is comprised of all the protons' magnetizations. They are not all spinning at the same frequency. From the rotating view it appears that the vectors spread out, the higher frequency vectors gaining phase, the angle, ϕ, with the y axis, and the lower frequency vectors losing phase, shown in Figure 5. As the vectors dephase, the magnetic resonance signal decays exponentially, with a rate constant, T_2,

and is much faster than T_1, the rate constant at which the magnetization vector returns to the z axis. In pure water, $T_1 = T_2$. As it requires energy to tip the magnetization, so energy is released when it relaxes. This energy is the signal recorded by the RF coils. Before that, though, the gradient coils apply yet another field such that only the particular plane, or slice, of interest will be relaxing at the same frequency as the RF coils. This is how specific slices are selected. This can take mere seconds but must be repeated for all phases of the protons. The inverse Fourier transform is applied to the raw data to get the final image. The subject must remain motionless during the scan (5).

1.2.2 MR Elastography

In magnetic resonance elastography (6), a conventional MRI scan is modified. A harmonic shear wave is introduced in the tissue by an internal or external actuator. The scanner's motion-encoding gradient coils are synchronized with the mechanical actuator. The protons in water in these oscillating magnetic field accrue a phase shift corresponding to their displacement. The phase depends on the strength of the magnetic field surrounding it by the integral relationship,

$$\phi = \mathfrak{g} \int \mathfrak{G}(t) \cdot \vec{r}(t) dt, \tag{1.28}$$

where ϕ is the phase, $\mathfrak{g}$ is the gyromagnetic ratio, $\mathfrak{G}(t)$ is the magnetic field strength, and $\vec{r}(t)$ is the position of the nuclear spins. The gradient coils create an oscillating field such that protons in certain parts of the material–peaks at $t = 0$ and troughs at $t = 1/2T$, where T is the period–are always in the strong part of the magnetic field, acquiring a larger phase shift than

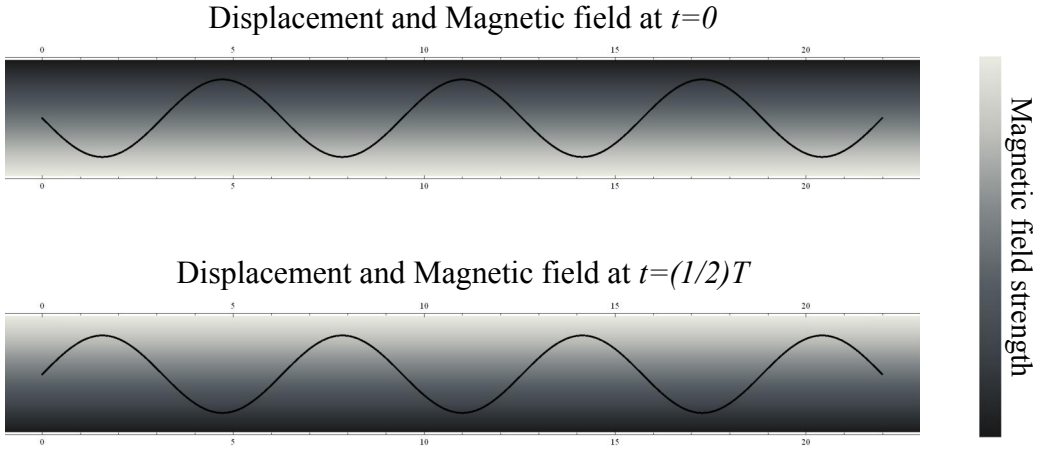

Figure 6. Displacement profile superimposed on a magnetic gradient

the oppositely displaced material. Figure 6 is a simplified illustration of the displacement in a magnetic gradient. The peaks at $t = 0$ are in the dark part of the field. Half a period later, there are troughs where there were peaks and the gradient has reversed, keeping those protons in the dark part of the field. Meanwhile, the protons on the other side of the wave–troughs at $t = 0$ and peaks at $t = 1/2T$–have remained in the light part of the field. The phase contrast image is analogous to a wave image from which the mechanical properties of the tissue, i.e. shear modulus, μ, can be calculated using the relationship,

$$\mu = \gamma (lf)^2 , \tag{1.29}$$

where γ is the material density, l is the wavelength, and f is the frequency of the applied vibrations.

1.3 Hydrogels

Before clinical use, before clinical trials, before even animal studies, medical imaging, at least nowadays, is tested on non-living objects called phantoms. Phantoms should ideally behave as would the objects for which the imaging is being considered. Out phantoms need to move and squeeze and bounce and shake like soft tissue. The best choice for our work, considering cost and ease of use, are solidified suspensions of colloids in water called hydrogels.

1.3.1 Colloids

The term colloid comes from the Greek kolla which means glue. It refers to substances of large molecular weight, e.g. collagen, the primary component of gelatin. The solution of a colloid dispersed in a fluid medium is called a sol. When a colloid dispersion solidifies it is called a gel. So diffusing e.g. gelatin or agarose into hot water will yield a hydrosol which, upon cooling, will solidify into a hydrogel (7). The mechanism by which a colloidal dispersion transitions from sol to gel, i.e. the particular attractive interaction between the elements of the disperse phase, depends on the type of colloid and may include electrostatic, Van der Waals, or chemical bonding (8). To make our phantoms, we combined two colloids, agarose and gelatin. Agarose is a neutral polysaccharide derived from seaweek whose gel rheologic properties, specifically dynamic Young's modulus, go linearly with concentration in water in the range used herein (9). Gelatin, whose dynamic Young's modulus also linearly correlates with concentration in water, is made from collagen derived from beef and pork hydes and bones (10).

1.3.2 Properties

Hydrogels are useful because they have essentially tunable viscoelastance. The higher the concentration of colloid in the hydrogel, the stiffer it will be. Watase et al showed that gelatin and agarose will interfere with each others' gelling abilities (11), but this was at concentrations much higher than those used in this work. Hydrogels offer us the opportunity to investigate how different colloids will behave alone, together, and in various ratios. Modifying these parameters would allow for the testing of different types of tissues in the body as well as mathematical models, e.g. fractional vs. integer order calculus (12).

1.3.3 Other Phantom Materials

While I have used hydrogels throughout these studies, I would be remiss not to mention what also has been used to great effect and what could still be of use. The first is a poly(dimethyl siloxane) (13; 14) called Ecoflex. It has rheologic properties similar to soft tissue. It has a longer curing time than hydrogels, but it lasts much longer. Water will evaporate from the hydrogels which will not only increase the concentration of colloid thus stiffening the phantom, but also change the shape. Ecoflex does not have this problem though it is also nowhere near as easy to use as gelatin. The other polymer that, to my knowledge, has yet to be used for magnetic resonance elastography phantoms, but shows great promise with regard to tenability is poly(ethylene glycol)-dimethacrylate (PEGDMA) (15). It is rather expensive, though, which is probably why it is not used.

CHAPTER 2

CONCENTRIC CYLINDERS

Magnetic resonance elastography (MRE) is an imaging technique that allows for the non-invasive visualization of the displacement field throughout an object from externally driven harmonic motion. Assuming linear elasticity, the stiffness of the material being scanned can be calculated by directly measuring the wavelength from the wave field images. This has been used to estimate the mechanical properties of soft tissue. Validation is attained by making certain assumptions about the material properties as well as the geometry of the wave fields and the region through which they are propagating, i.e. a plane wave traveling through an infinite medium. This is necessary because the actual geometry of e.g. an entire liver is not amenable to an analytic solution of the linear vector Helmholtz equation. Recent studies, however, have extended the scale of MRE, even down to the microscopic (16). And on a small enough scale much of physiology can be mathematically modeled with basic geometric shapes, e.g. a cylinder representing a blood vessel. In principal, then, MRE can be used to carefully study models of pathology with specifically designed phantoms. One very important benefit of MRE is the ability to collect information from any plane throughout the object which, coupled with the geometric focusing technique pioneered by Yaşar et al. (16), overcomes the loss of viscous damping, allowing for detection of high frequency waves deep in a highly viscous material, e.g. agarose. That is the focus of this paper: the design and analysis of a phantom for use in MRE and inverse modeling with a closed-form analytic solution.

2.1 Introduction

The mechanical properties of biologic tissue are informed by their relative states of health. A Malignant tumor in, e.g. breast, liver, pancreas, etc., tissue is noticeably stiffer than the surrounding healthy regions of that tissue. Further, the progression of disease can be characterized by the degree to which the mechanical properties veer from normal as in, e.g. the maturity of a blood clot in deep vein thrombosis (17). This phenomenon makes the ancient art of palpation, the manual pressured probing of a patient's body, to this day an invaluable method to detect maladies. Though inexpensive and universally applicable, noninvasive palpation is limited to the periphery of a patient's body. A small tumor deeply embedded in tissue could be missed, and allowed to grow, reducing a patient's chance of survival. Moreover, a doctor's tactile sensitivity to variations in tissue stiffness is, by nature, a subjective trait, prone to error in disease detection and characterization. The broad engineering challenge is centered around the noninvasive, high resolution, characterization of soft tissues through their mechanical behavior. Linear elastic theory defines a mechanical system through a plethora of parameters though an imaging modality need not consider them all to be clinically relevant. The complex shear modulus, in particular, has received scrutiny in the literature of late as a biomarker for pathologies in magnetic resonance (MR) elastography (6; 18; 19; 20; 21). In MR elastography an object is perturbed with harmonic oscillations from a mechanical actuator. The displacement throughout the material, i.e. the wave field, is encoded in the phase of the MR signal by synchronizing the gradient coils of the MRI scanner with the oscillatory frequency of the actuator. The shear modulus can be estimated from these wave data with various inverse modeling techniques (22).

Medical imaging requires phantom studies for validation. Hydrocolloid suspensions are affordable and easily made so they have seen considerable use as tissue-mimicking phantoms in all manner of elastographic studies.

2.1.1 Homogeneous Material

To validate a novel technique or model in elastographic imaging it is sometimes necessary that the samples being studied be homogeneous to eliminate artifacts from, e.g. scattering. Perriñez et al used a bean curd, tofu, to mimic soft poroelastic tissue in MR elastography (23), estimating shear modulus from simulated data with a finite-element-based nonlinear inversion scheme. Othman et al used agarose gel phantoms to extend MR elastography to the micro scale (16; 24; 25). Homogeneous gelatin phantoms have also been used in ultrasound elastography. Amador et al validated their shearwave dispersion ultrasound vibrometry technique with a hydrocolloid mixture of gelatin, glycerol and cellulose by comparing the results to those of indentation tests (26), while Zhang et al validated their surface wave method in a similar study (27).

2.1.2 Heterogeneities and Connectedness

Some researchers deliberately introduce heterogeneities in their phantoms to more closely mimic a biologic system. Henni et al did ultrasound elastography on a cuboidal gelatin phantom that had a soft cylindrical region running through it to validate their elegant analytic model of scattering and diffraction of a plane shear wave by an infinite cylinder (28). Schmitt et al used Henni's model to solve the inverse problem of characterizing vascular behavior with ultrasound elastography (29; 30). Doyley et al constructed elastically heterogeneous phantoms by

embedding hydrogel spheres in a hydrogel spheres in a hydrogel medium of a different stiffness than the spheres to show that more sophisticated mathematical assumptions, i.e. nonlinearity, anisotropy, and viscoelasticity should be made when reconstructing elastograms from MR elastography data (31). Qin et al immersed spandex fibers in a polyvinyl alcohol hydrogel to test a combined MR elastography and diffusion tensor imaging technique (32). Yin et al designed a ball-in-tube phantom to demonstrate their novel technique for simultaneous acquisition of diffusion and MR elastography data (33). As the geometry of the phantoms increases in complexity, e.g. being multiply connected as opposed to simply connected or mixing geometry, so do the analytic solutions describing their dynamic mechanical behavior. Certainly a phantom that accurately models the geometry of a brain would necessitate a technique like local frequency estimation to infer its mechanical properties, but there are many geometric configurations with clinical or academic relevance that are amenable to analytic solutions. Khan et al modeled a corneal phantom as a thin viscoelastic plate (34). They obtained an elastogram by fitting their closed form analytic solution to displacement data. Yaşar et al used the solution to a longitudinally vibrating, homogeneous, infinite circular cylinder to obtain shear stiffnesses of cylindrical phantoms over a wide range of frequencies (35). Okamoto et al conducted a similar study but varied their phantoms' composition (36). Also, they had a different mathematic solution because their actuation came from within their phantom, whereas Yaşar et al perturbed their phantom's outer surface.

2.1.3 Objective

Of all the works mentioned, Okamoto et al is the only MR elastography study to obtain estimates of the complex shear modulus of a multiply connected body by inverse modeling with a closed form analytic solution. There has been no such modeling of a multiply connected *heterogeneous* body in MR elastography and this is what is presented now. The solution to a concentric cylindrical body undergoing harmonic oscillations is derived from first principles. The phantom construction, experimental procedure, parameter estimation, and the forward problem are then described. To validate the model, the shear moduli estimates as inputs to solve the forward problem with a finite element model (FEM) are used and compared with experimental results. Finally the immediate consequences of this work as well its implications for future research are considered.

2.2 Theory

2.2.1 Problem Formulation

Let there be given an infinitely long, rigid, circular cylindrical tube on inner radius, b, filled with an elastic solid, medium 1. Concentrically embedded therein is a circular cylindrical elastic solid, medium 2, with mechanical properties different from medium 1. This system is described by cylindrical coordinates (ρ,ϕ,z) (2), and shown in Figure 7. The rigid tube harmonically oscillates along the z axis and it is assumed that medium 1 is in intimate contact

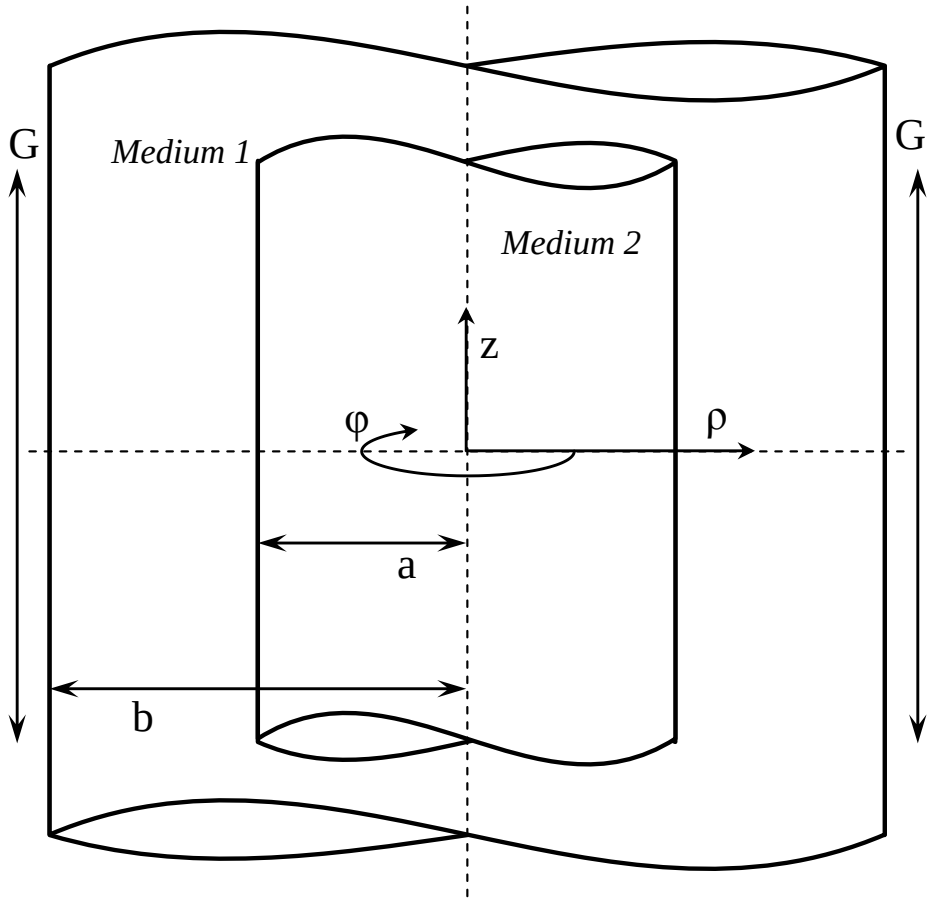

Figure 7. The cylindrical media are referred to a cylindrical coordinate system (ρ, ϕ, z) with the z axis coinciding with the axes of the media.

with both medium 2 and the oscillating wall. The displacement of both media satisfy the vector Helmholtz equation (1),

$$\alpha_i^2 \nabla\nabla\cdot\vec{U} - \beta_i^2 \nabla\times\nabla\times\vec{U} + \omega^2\vec{U} = 0 \tag{2.1}$$

where

$$\alpha_i^2 = (\lambda_i + 2\mu_i)\,\gamma_i^{-1} \quad (i = 1, 2) \tag{2.2a}$$

and

$$\beta_i^2 = \mu_i \gamma_i^{-1} \ (i = 1, 2). \tag{2.2b}$$

The constants, λ_i and μ_i, are the Lame constants, and γ_i is the density of the material. It is held that $\lambda_i = (2\mu_i\nu)\,/\,(1-2\nu)$, where the Poisson ratio is $\nu = 0.4999998$ for both media. Here the index i is 1 or 2 to denote the medium, i.e.

$$i = \begin{cases} 1, & \text{if } a < \rho \le b \\ 2, & \text{if } 0 < \rho \le a \end{cases}. \tag{2.3}$$

The harmonic time dependence, $e^{i\omega t}$, is suppressed throughout this study. The boundary condition at the outer surface of medium 1 is equality of tangential displacement of the wall and elastic medium,

$$u_1(\rho, z)|_{\rho=b} = G \tag{2.4}$$

where G is the amplitude of the forced oscillations. At the interface between media 1 and 2, the boundary conditions are equality of the tangential displacement and stress,

$$u_1(\rho, z)|_{\rho=a} = u_2(\rho, z)|_{\rho=a} \tag{2.5a}$$

$$\sigma_1(\rho, z)|_{\rho=a} = \sigma_2(\rho, z)|_{\rho=a}. \tag{2.5b}$$

The solution of Equation 2.1 can be given as the sum of the vector wave functions, $\vec{L}$, $\vec{M}$, and $\vec{N}$ given as

$$\vec{L} = \nabla\Phi \tag{2.6a}$$

$$\vec{M} = \nabla \times \hat{e}\Psi \tag{2.6b}$$

$$\vec{N} = \beta_i^{-1}\nabla \times \nabla \times \hat{e}\mathrm{X} \tag{2.6c}$$

where Φ, Ψ, and X each solves the scalar Helmholtz equation,

$$\left(\nabla^2 + \alpha_i^{-2}\right)\Phi = 0, \tag{2.7a}$$

$$\left(\nabla^2 + \beta_i^{-2}\right)\Psi = 0, \tag{2.7b}$$

$$\left(\nabla^2 + \beta_i^{-2}\right)\mathrm{X} = 0, \tag{2.7c}$$

and $\hat{e}$ is a constant vector (1). The displacement in medium 1 is the sum of the incidental and scattered wave fields, $\vec{U}^{(i)}$ and $\vec{U}^{(s)}$, respectively, while the displacement in medium 2 is

from the refracted wave field only, $\vec{U}^{(r)}$. One can write, then, the displacement as a piecewise continuous function throughout the entire domain, i.e.

$$u(\rho,z)=\begin{cases} u_1(\rho,z)=\vec{U}^{(i)}+\vec{U}^{(s)}, & \text{if } a<\rho\leq b \\ u_2(\rho,z)=\vec{U}^{(r)}, & \text{if } 0<\rho\leq a \end{cases}. \tag{2.8}$$

Due to the axial and longitudinal symmetry of this system, one need be concerned with only the vertically-polarized transverse waves, i.e. $\vec{L}=\vec{M}=0$ for all wave fields. The wave fields are, then, simply given as

$$\vec{U}^{(i)}=\vec{N}^{(i)}. \tag{2.9a}$$

$$\vec{U}^{(s)}=\vec{N}^{(s)}. \tag{2.9b}$$

$$\vec{U}^{(r)}=\vec{N}^{(r)}. \tag{2.9c}$$

In cylindrical coordinates, the constant vector is the unit vector, $\hat{z}$, making the vector function (37)

$$\vec{N}^{(i)}=\frac{1}{q_i\rho}\frac{\partial}{\partial\rho}\left(\rho\frac{\partial \mathrm{X}^{(i)}}{\partial\rho}\right)\hat{z}. \tag{2.10a}$$

$$\vec{N}^{(s)}=\frac{1}{q_i\rho}\frac{\partial}{\partial\rho}\left(\rho\frac{\partial \mathrm{X}^{(s)}}{\partial\rho}\right)\hat{z}. \tag{2.10b}$$

$$\vec{N}^{(r)}=\frac{1}{q_i\rho}\frac{\partial}{\partial\rho}\left(\rho\frac{\partial \mathrm{X}^{(r)}}{\partial\rho}\right)\hat{z}. \tag{2.10c}$$

One can calculate the relevant components of the stress tensor, $\sigma_{\rho z}$, directly from the displacement, given here as

$$\sigma_i = \mu_i \frac{\partial u_i(\rho, z)}{\partial \rho} \quad (i = 1, 2). \tag{2.11}$$

2.2.2 Solutions

The potential functions are given by

$$\mathrm{X}^{(i)} = AJ_0(q_1\rho) \tag{2.12a}$$

$$\mathrm{X}^{(s)} = BH_0(q_1\rho) \tag{2.12b}$$

$$\mathrm{X}^{(r)} = CJ_0(q_2\rho) \tag{2.12c}$$

where

$$q_i = \frac{\omega}{\beta_i} \quad (i = 1, 2) \tag{2.13}$$

and A, B, and C are the unknown coefficients determined by satisfying the boundary conditions. Here J_0 and H_0 are the 0^{th} order cylindrical Bessel and Hankel functions (4), respectively.

2.2.3 Boundary Conditions

Considering Equation 2.12, Equation 2.10, Equation 2.9, and Equation 2.8, the boundary conditions, Equation 2.4 and Equation 2.5, become three equations through three unknowns, given in matrix form as

$$\begin{bmatrix} \varepsilon_{11} & \varepsilon_{12} & \varepsilon_{13} \\ \varepsilon_{21} & \varepsilon_{22} & \varepsilon_{23} \\ \varepsilon_{31} & \varepsilon_{32} & \varepsilon_{33} \end{bmatrix} \begin{bmatrix} A \\ B \\ C \end{bmatrix} = \begin{bmatrix} G \\ 0 \\ 0 \end{bmatrix}. \tag{2.14}$$

After considerable algebraic simplification, the elements of Equation 2.14, ε_{mn}, are given here as

$$\varepsilon_{11} = \varepsilon_{21} = -q_1 J_0(bq_1), \tag{2.15a}$$

$$\varepsilon_{13} = 0, \tag{2.15b}$$

$$\varepsilon_{12} = \varepsilon_{22} = -q_1 H_0(bq_1), \tag{2.15c}$$

$$\varepsilon_{23} = -q_2 J_0(bq_2), \tag{2.15d}$$

$$\varepsilon_{31} = -\mu_1 q_1^2 J_1(aq_1), \tag{2.15e}$$

$$\varepsilon_{32} = -\mu_1 q_1^2 H_1(aq_1), \tag{2.15f}$$

$$\varepsilon_{33} = -\mu_2 q_2^2 J_1(aq_2). \tag{2.15g}$$

Solving for A, B, and C, completely determines all wave fields, concluding the mathematical analysis. The expansion coefficients A, B, and C are too cumbersome to write out completely. Instead, they are given here in parametric from, i.e.

$$A = \frac{Gq_1\mu_1 c}{q_1 d}, \tag{2.16a}$$

$$B = \frac{Gq_2\mu_2 e}{q_1 d}, \tag{2.16b}$$

$$C = \frac{2iG\mu_1}{\pi a q_2 f}, \tag{2.16c}$$

where

$$d = q_1\mu_1 J_0(aq_1)c + q_2\mu_2 J_1(aq_2)g, \tag{2.17a}$$

$$f = q_1\mu_1 J_0(aq_2)h + q_2\mu_2 J_1(aq_2)j, \tag{2.17b}$$

and where

$$c = H_1(aq_1)J_0(aq_2) - H_0(aq_1)J_1(aq_2), \tag{2.18a}$$

$$e = J_0(aq_1)J_1(aq_2) - J_1(aq_1)J_0(aq_2), \tag{2.18b}$$

$$g = H_0(aq_1)J_0(bq_1) - J_0(aq_1)H_1(bq_1), \tag{2.18c}$$

$$h = H_1(aq_1)J_0(bq_1) - J_1(aq_1)H_0(bq_1), \tag{2.18d}$$

$$j = J_0(aq_1)H_0(bq_1) - H_0(aq_1)J_0(bq_1). \tag{2.18e}$$

TABLE I

Concentrations of polymers, in percent by weight, in the two hydrocoloid media

Medium	% by weight gelatin	% by weight agarose
1	4	0.75
2	1	0.4

2.3 Method

2.3.1 Phantom Construction

2.3.1.1 Matrix Preparation

The matrices of the inner and outer cylinders are hydrocoloids made from a mixture of agarose (SeaKem LE Agarose, Lonza, Rockland, ME) and food grade gelatin (Knox Original Unflavored Gelatine, Kraft Foods Group Inc., Northfield, IL) in water. The concentrations of the separate media are summarized in Table I. Each hydrocoloid was prepared by first sprinkling granulated gelatin into room temperature DI water which was then heated while stirred constantly. Once all the gelatin dissolved, agarose was then added. Heating and stirring continued until clarification, at 90 °C. The molten gel was allowed to cool to about 40 °C before being poured into the molding.

2.3.1.2 Molding

To ensure concentricity between the two hydrocoloid solids a moldwas designed and custom-built, depicted as a cut-away view in Figure 8, and as it exists in the laboratory in Figure 9. On the bottom is a stage made of poly(methyl methacrylate) (PMMA) (Plexiglas®, Rohn and Haas Company, Philadelphia, PA) with an annular dais, in whose center a removable PMMA rod tightly fits. Encircling the dais is the cylindrical container made of an acetyl resin (Delrin, DSM Engineering Plastic Products, Inc., Reading, PA). All components were manufactured at the University of Illinois at Chicago. The PMMA components were manufactured by the machine shop of the College of Liberal Arts and Sciences, and the acetyl resin component was manufactured by the machine shop of the College of Engineering.

2.3.1.3 Phantom Assembly

The final assembly of the phantom is basically a two step process: Step 1. the outer cylinder (medium 1), Step 2. the inner cylinder (medium 2). For medium 1, the delrin container is mounted on the dais and the acrylic rod is inserted in the depression. Then the 40 °C molten medium 1 is poured into the space between the delryn and PMMA, with particular attention payed for any bubbles that might form. It is important that there be no bubbles–or any heterogeneity–within each medium as they would cause scattering and diffraction of the mechanical waves for which there is no account in our mathematical model. Air, especially, would be disruptive to the waves because fluids do not support shear waves, guaranteeing a mode conversion. Once the mold is filled, it is set aside and allowed to cool. No sealant was found to be necessary between the cylindrical container and dais. It is at this point when the

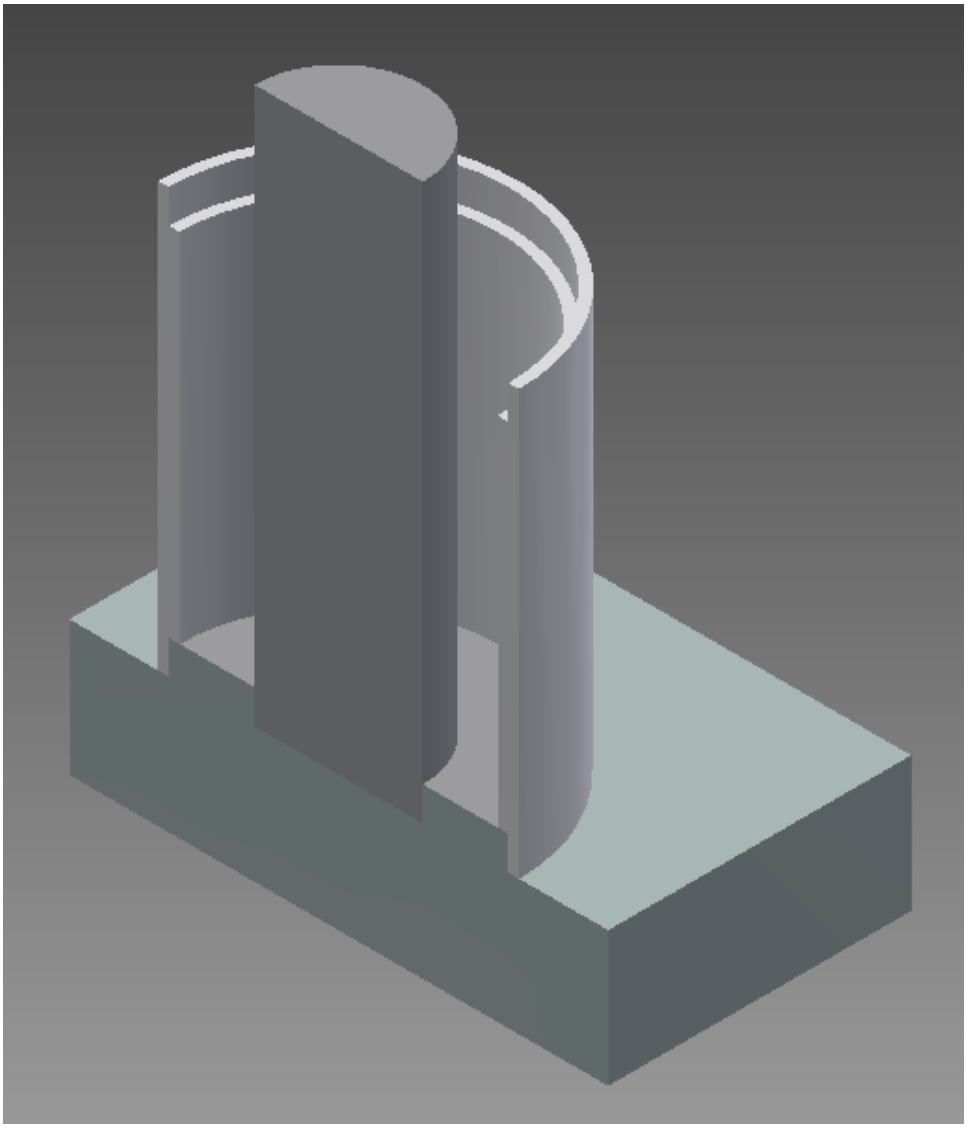

Figure 8. Cut-away view of the assembly.

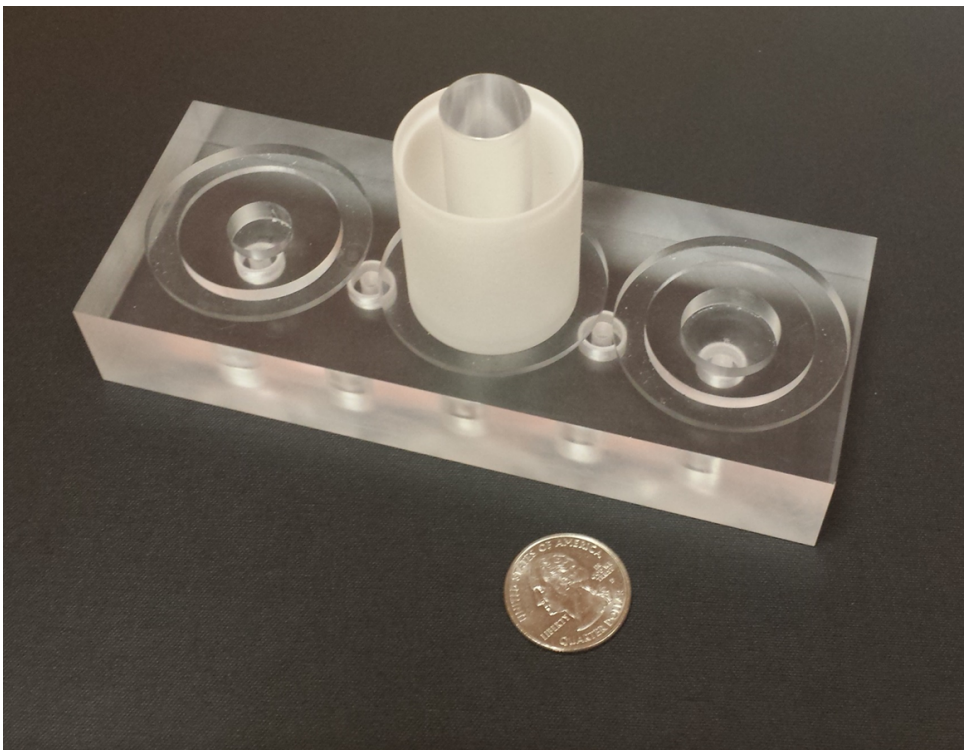

Figure 9. Molding

hydrocoloid for medium 2 is prepared, (section 2.3.1.1). Medium 1 will stick to the acetyl resin but not the PMMA, so, once it has solidified, the cylindrical container was vertically pulled off the dais, sliding the medium 1 off the rod. Now begins step 2. First the rod is removed from the dais. To ensure that the media are flush with each other, a piece of plastic paraffin film (Parafilm "M"®, Bemis Flexible Packaging, Neenah, WI) was stretched over the dais to cover the depression before replacing the cylindrical container and medium 1 on the dais. Once affixed, the molten medium 2 was poured into the vacancy left by the rod. The entire body was then allowed to cool to room temperature before removing from the dais for scanning.

2.3.2 Experimental Setup

MR elastography experiments were performed at 9.4 T using a horizontal bore Agilent small-animal MR scanner (310/ASR, Agilent Technologies, Santa Clara, CA) (33). A 39 mm diameter quadrature RF coil was used inside a 60 mm diameter gradient coil with a maximum gradient of 1000 G/m. The gel-filled container was placed horizontally inside the center of the RF coil. the container was attached to a pre-loaded piezo-actuator (p-840.1, PhysikInstrumente (PI) GmbH & Co. KG, Germany), which generates the transverse vibration motion. All phantoms were scanned at the excitation frequencies of 250, 500, and 750 Hz. This experimental setup establishes concentric wave patterns within the gel.

2.3.3 Data Acquisition

A customized spin-echo (SE) based MR elastography sequence with a sinusoidal motion-sensitizing gradient (MSG) was used for data acquisition, obtaining one axial slice and one coronal slice. The acquisition parameters, summarized in Table II, were as follows: repetition

TABLE II

Parameters for data acquisition

TR	1 s
TE	28 ms
FOV	4 cm × 4 cm
Matrix size	128 × 128
Slice thickness	1 mm
MSG	30 G/cm

time (TR) = 1 s, echo time (TE) = 28 ms, field of view (FOV) = 4 cm × 4 cm, matrix size = 128 × 128, slice thickness = 1 mm, MSG = 30 G/cm. The number of MSG cycles varied with the actuation frequency from 2 to 6 to accommodate constant TR/TE imaging parameters. In all scans, the MSG was applied along the principle direction of vibration in our experimental setup. Phase difference images were made from two acquisitions by inverting the polarity of the MSG. Four time steps were acquired per actuation cycle.

2.3.4 Estimation of Shear Moduli, μ_i

To estimate the complex moduli of the two media, the analytic solution for displacement, $u(\rho)$, was fit to the displacement data. A fitting algorithm was written in MatLab (Math-Works, Inc., Natick, MA) called Data Analysis and Visualization Toolbox (DeVIANT). It is described in detail in (35). Briefly, the data to which the model is fit is a linear profile, u_n, taken from the experimental complex wave images. Some parameters were added to the model to take into

account phase, θ, bias from compression wave, η, magnitude scale, s, and off-centering, δ. This is expressed as

$$\underset{\Psi}{MIN}\left\{\sum_{n=-N}^{N}\|u_n-\hat{u}\left(\rho_n\right)\|^2\right\} \tag{2.19}$$

where

$$\hat{u}(\rho)=s\times e^{i\theta}\times u(\rho_n+\delta)+\eta, \tag{2.20}$$

and the set of parameters is $\Psi=\{\mu_1,\mu_2,\theta,\eta,s,\delta\}$. The chief difference in DeVIANT for this study is that the complex shear moduli of two different regions are being found with a piecewise-continuous function, Equation 2.8.

2.3.5 The Forward Problem

The analytic model assumes that the cylinders are infinitely long, i.e. it neglects edge effects from the top and bottom of the phantom. To validate the estimates, then, a two-dimensional, axisymmetric FEM in ANSYS (12.1 v, ANSYS, Inc. Pittsburg, PA) was created. A quadrilateral mesh of 12496 elements was used and with a maximum element size of 0.3 mm, and degree of freedom of 50586. The forward problem was solved using as inputs the parameters of the experimental procedures ($\omega=2\pi f$, where $f=250, 500, 750$, and 1000 Hz., $a=0.75$ cm, $b=1.5$ cm, height$=3$ cm) and fitting results (section 2.4), summarized in Table III.

2.4 Results

The scanning was at four frequencies, 250, 500, 750, and 1000 Hz. These seem like reasonable upper and lower limits. Vibrations at frequencies less than 250 Hz would yield wavelengths longer than the diameter of the phantom, making it difficult to see the agreement between

TABLE III

Parameters for FEM

a	0.75 cm
b	1.5 cm
height	3 cm
degree of freedom	50586
no. of elements	12496
max. element size	0.3 mm

model and experiment. Going higher then 1000 Hz would also obscure any agreement between theory and data because the attenuation of the mechanical waves would overcome the benefical effect even of geometric focusing, i.e. there would be no discernible displacement save for at the radial periphery of the phantom. At each frequency the displacement was fit to ten linear profiles taken from the displacement, getting complex moduli from each profile. In Figure 10 and Figure 12 the mean ± one standard deviation of the real and imaginary components of μ_1 were plotted, respectively. The components of μ_2 are shown in Figure 11 and Figure 13. The numeric values of all μ_i are summarized in Table IV. A frequency dependence can be seen wherein the complex shear moduli of both media increase as does the frequency of the applied vibrations, in keeping with previously reported trends of hydrocolloids of gelatin (38) and agarose-gelatin mixtures (36). The experimental (left) and simulated (right) wave images in the plane parallel to the z axis and containing the origin for the scans at 250, 500,

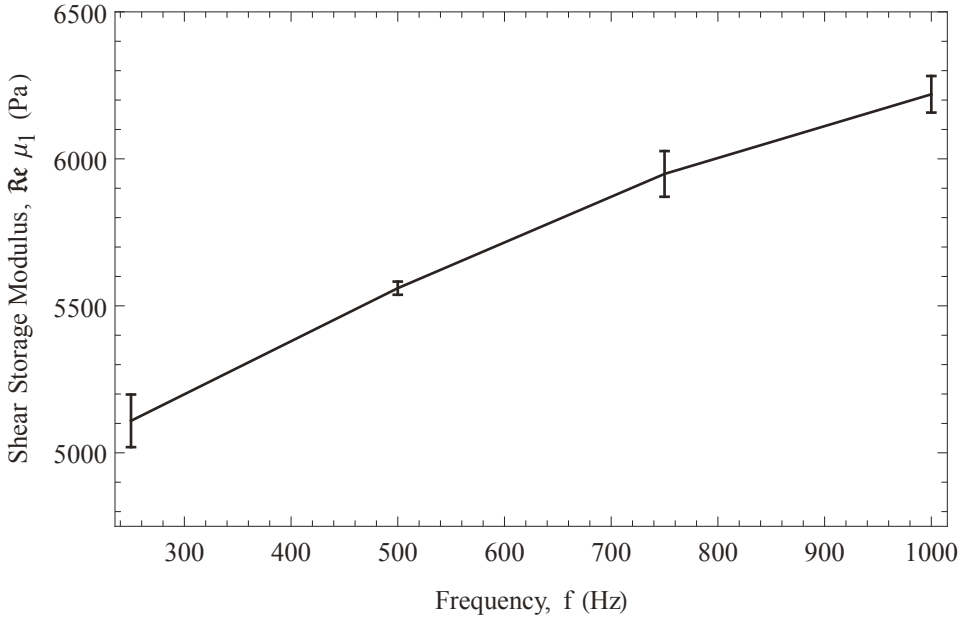

Figure 10. Storage shear modulus of Medium 1. The error bars are one standard deviation from the mean.

750, and 1000 Hz are shown in Figure 14, Figure 15, Figure 16, and Figure 17, respectively. Close agreement can be seen between theory and data in all four frequencies.

A more profound understanding of how the model matches the data is realized when their linear profiles are plotted together, shown in Figure 18, Figure 18, Figure 18, and Figure 18 for frequencies, 250, 500, 750, and 1000 Hz respectively.

2.5 Discussion

The connectedness of a mechanical system is central to its internal operation as well as its response to external stimuli. In the context of MR elastography, the behavior of biologic materials through which mechanical energy is propagating is of concern. Ultimately this is a

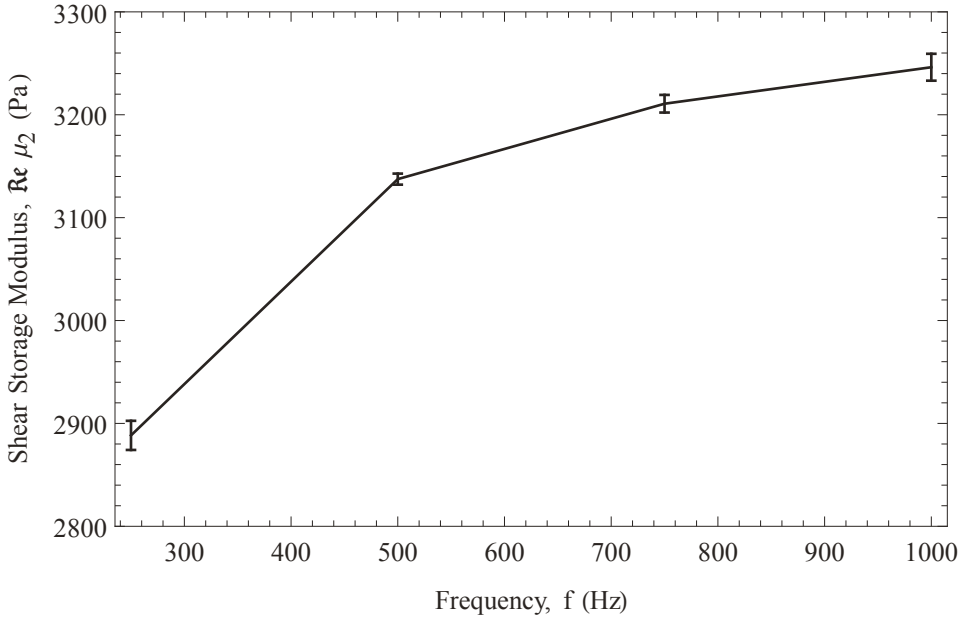

Figure 11. Storage shear modulus of Medium 2. The error bars are one standard deviation from the mean.

medical device, to be used on an organismic scale, e.g. human beings, and so the biomaterials in question will be found in a very complex network of interacting systems connected on many levels, e.g. electrically, chemically, hæmodynamically, and, of course, mechanically. The elastodynamic behavior of a material depends on its surroundings and biomaterials are no exception. It behooves researchers, then, to investigate not only the behavior of tissue-mimicking materials, but the behavior of said materials ensconced in a system-mimicking setting. To that end a multiply connected hydrogel phantom was modeled, designed, built, and tested. The results are addressed in turn, and their implications considered.

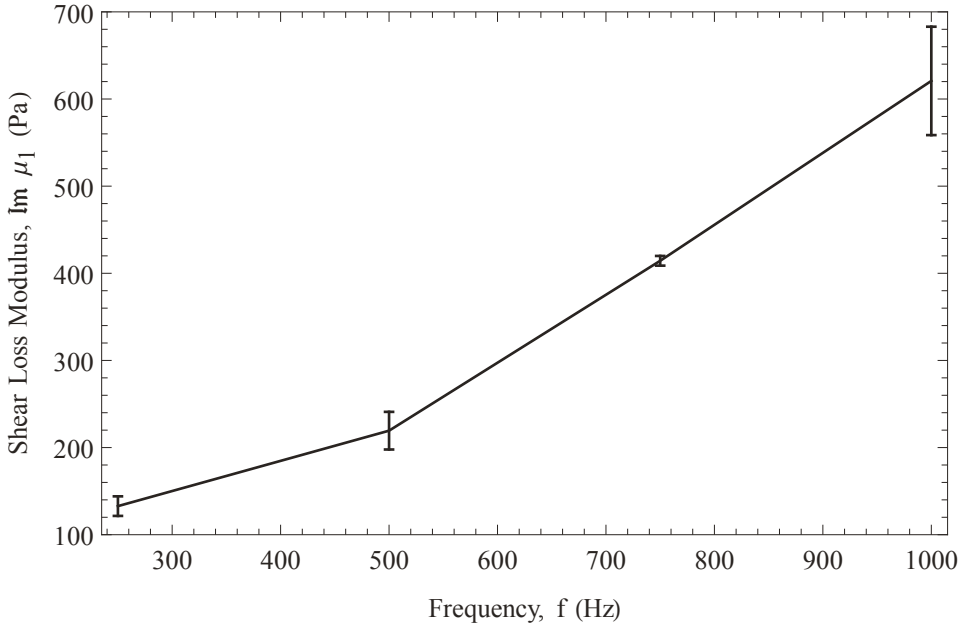

Figure 12. Loss shear modulus of Medium 1. The error bars are one standard deviation from the mean.

From the model fitting it is found that the complex shear moduli of the materials increase with the oscillatory frequency of the mechanical actuator. While, as noted in section 2.4, this does generally follow reported trends of hydrogels, it is not clear how the specific composition of the gels informed the results. Obviously increasing the total colloid concentration increased the stiffness, but it is not clear what role the individual colloids had. The mathematical model does not distinguish between the types of colloids or their chemical interactions or their molecular interconnectedness. Employing fractal models of polymers (39) might shed light here as could generalizing the calculus operations (40) (41).

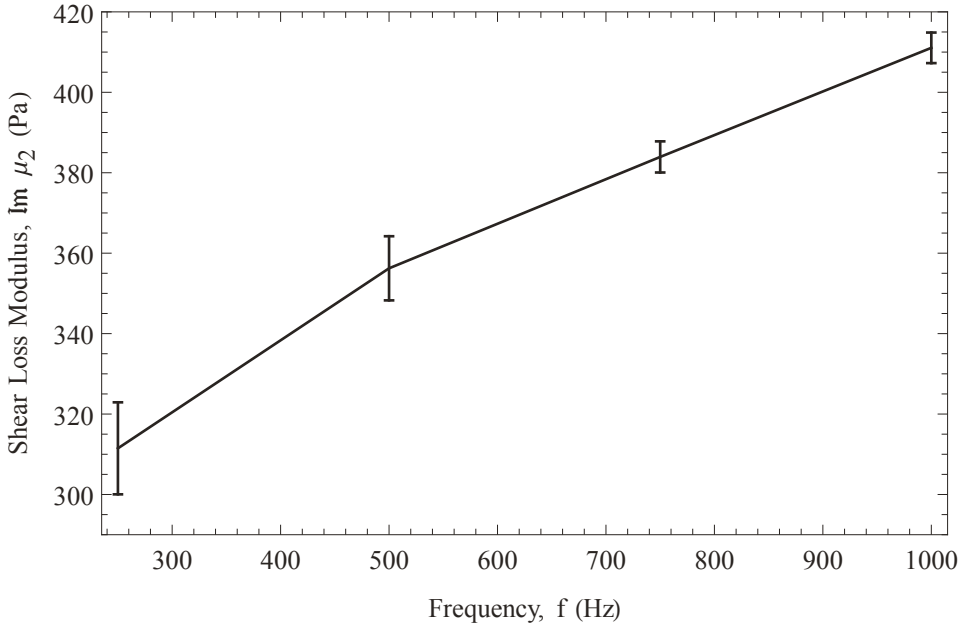

Figure 13. Loss shear modulus of Medium 2. The error bars are one standard deviation from the mean.

In the forward modeling close agreement was found between theory and experiment. The noteworthy discrepancies seem to be toward the top and bottom of the phantom. In the experimental images of Figure 14, Figure 15, Figure 16, and Figure 17, there appears to be a distortion in the wave field at the axial extremes. It is more pronounced in the upper three frequencies than in the lowest one. Given the location, it is assumed that this is an edge effect, and, thus, why a FEM was used for the forward problem. This highlights the major flow with the closed form analytic model, i.e. the assumption that the cylinders are infinite in length. The FEM seems to capture the apparent edge effects but not perfectly, implying that there is more at work than yet described mathematically. One very real possibility is the existence

TABLE IV

Complex shear moduli, μ_1 and μ_2, $\pm$ one standard deviation in units of Pa. The frequency, f, is in Hz.

f	$\mathfrak{Re}\mu_1$	$\mathfrak{Im}\mu_1$	$\mathfrak{Re}\mu_2$	$\mathfrak{Im}\mu_2$
250	5108 ± 90	133 ± 11	2888 ± 14	311 ± 11
500	5560 ± 22	219 ± 22	3137 ± 5	356 ± 8
750	5949 ± 78	414 ± 6	3210 ± 9	384 ± 4
1000	6219 ± 62	620 ± 15	3246 ± 13	411 ± 4

of a third cylindrical layer. Switching the two media was tried, i.e. make the inner cylinder out of the stiffer medium 1 and vice versa, but the softer hydrocolloid would not stick at all the resin shell. This is likely due to the reduced gelatin content, because the two media still stuck to each other. Perhaps also the interface between the two media is not as stark as the mathematical model assumes. It is speculated that mixing or, at least, diffusion happens while the second hydrocolloid cools, transitioning from sol to gel. Immediately upon touching the first medium, the heat of the second will melt a thin layer of the first, forming an intermediate later. Having a different colloid concentration from the layers on either side, this layer would have different mechanical properties from the other layers, ergo its own two wave fields and unknown coefficients as well as change the expressions for the waves of the original media. This speaks to the point of this work, that the increasing precision of imaging modalities demands more

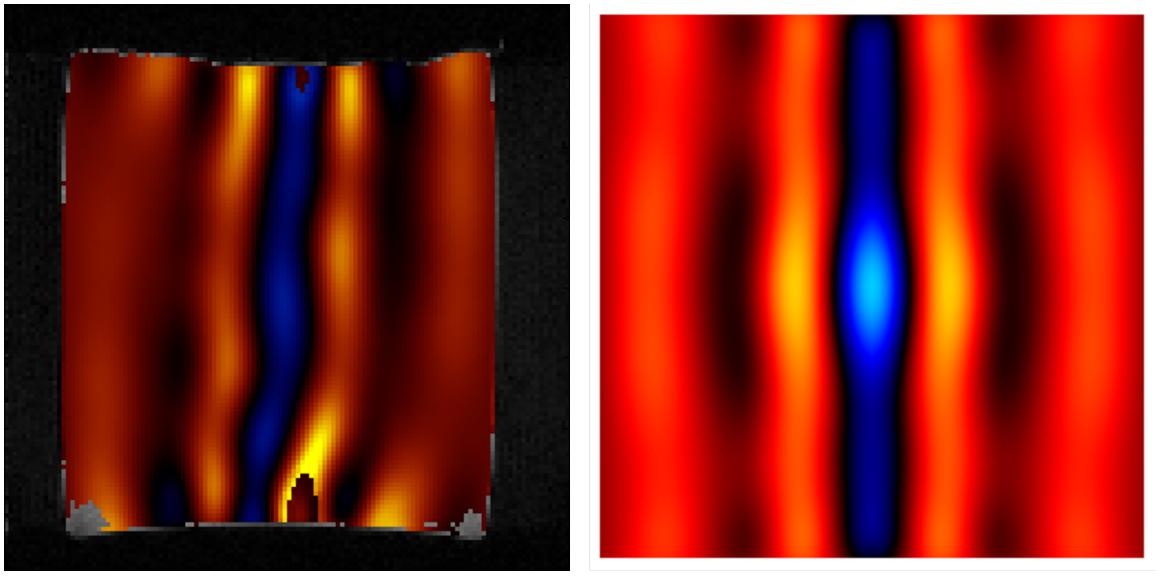

Figure 14. Experimental (left) and theoretic (right) wave field through a plane parallel to the z axis, containing the origin. The excitation frequency is 250 Hz. The estimated complex moduli are $\mu_1 = 5108.82 - 132.8i$ Pa and $\mu_2 = 2888.37 - 311.478i$

careful and precise tools of validation and verification. This study features novel mathematical modeling but also deigned to showcase the phantom construction techniques and the exceptional care required in such highly determined systems.

Finally, it is noticeable in the planar images and very clear in the linear profiles that, despite the best phantom construction efforts, perfect axial symmetry was not achieved at all frequencies. It is most apparent in the linear profile of 1000 Hz, Figure 21. Note, however, that the amplitude seems to be equal but opposite across the origin, i.e. it is very high on the left side and very low on the right side. It is possible that this is due to the experimental setup and not actually the phantom construction. The same protocol was used as that described

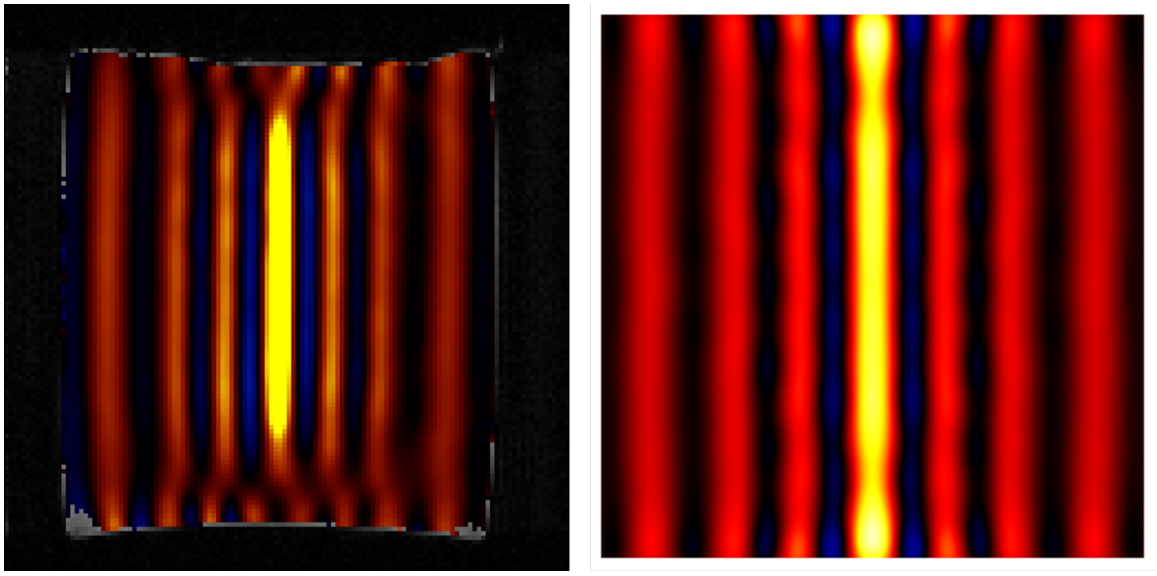

Figure 15. Experimental (left) and theoretic (right) wave field through a plane parallel to the z axis, containing the origin. The excitation frequency is 500 Hz. The estimated complex moduli are $\mu_1 = 5560.08 - 219.378i$ Pa and $\mu_2 = 3137.43 - 356.238i$

in (33). The asymmetric displacement is likely due to the horizontal positioning (depicted in figure 2 of that article) of the phantom, causing unequal contact force between the gel and resin container. The gel on the side facing down would be under the weight of the entire phantom pushing it down as well as the cohesion of the gel to create a shear force, while the side facing up would have merely the cohesion of the gel. Still, the results are generally what was expected, confirming the methods and, hopefully, leading to further developments in this field.

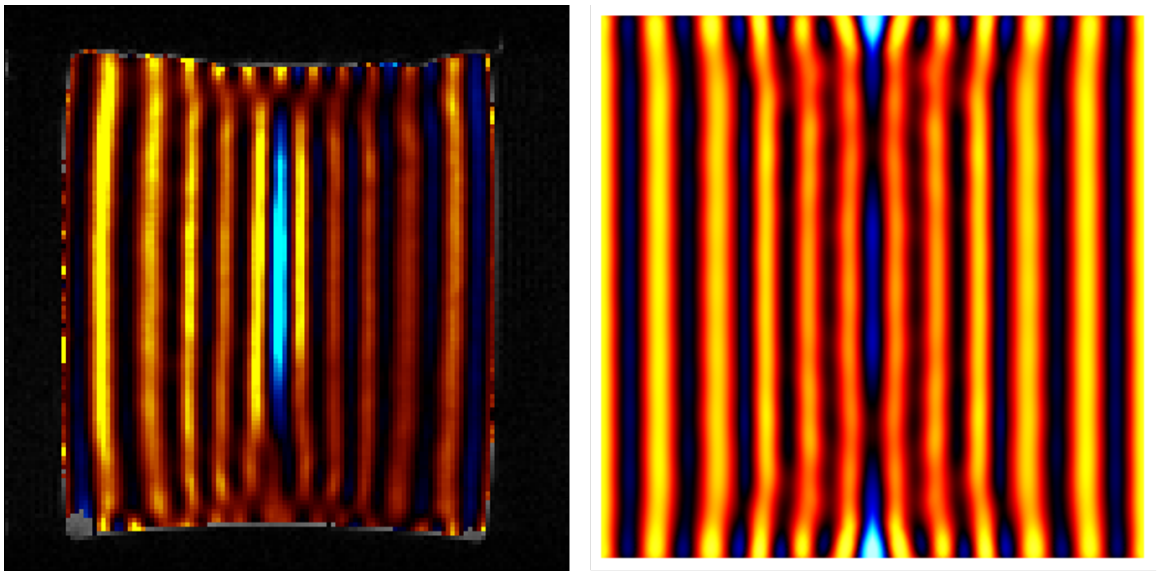

Figure 16. Experimental (left) and theoretic (right) wave field through a plane parallel to the z axis, containing the origin. The excitation frequency is 750 Hz. The estimated complex moduli are $\mu_1 = 5948.72 - 414.337i$ Pa and $\mu_2 = 3210.72 - 383.932i$

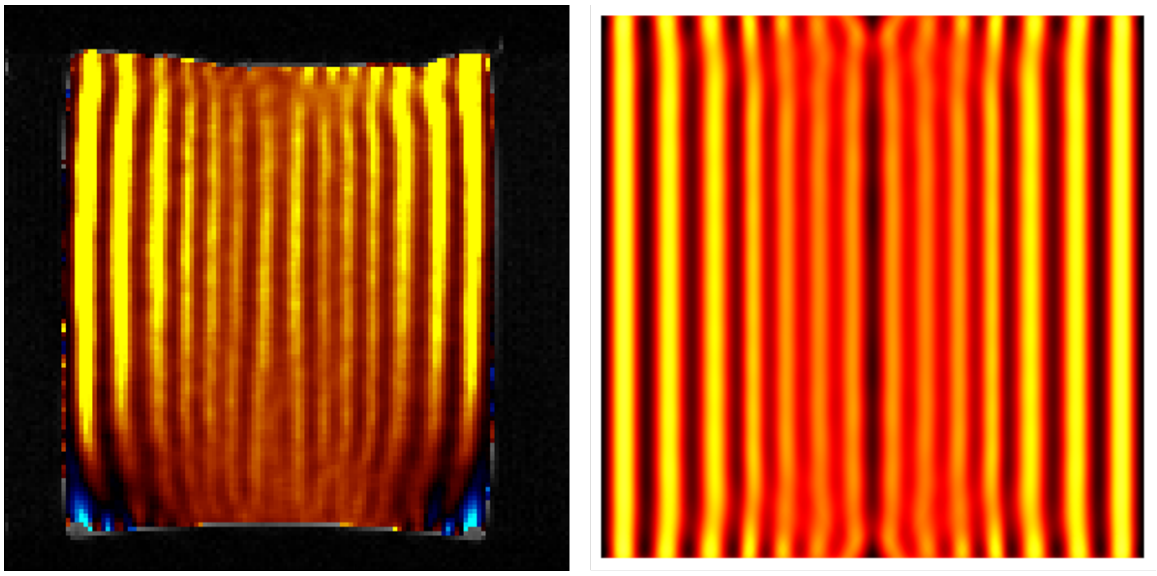

Figure 17. Experimental (left) and theoretic (right) wave field through a plane parallel to the z axis, containing the origin. The excitation frequency is 1000 Hz. The estimated complex moduli are $\mu_1 = 6219.57 - 620.777i$ Pa and $\mu_2 = 3246.19 - 411.058$

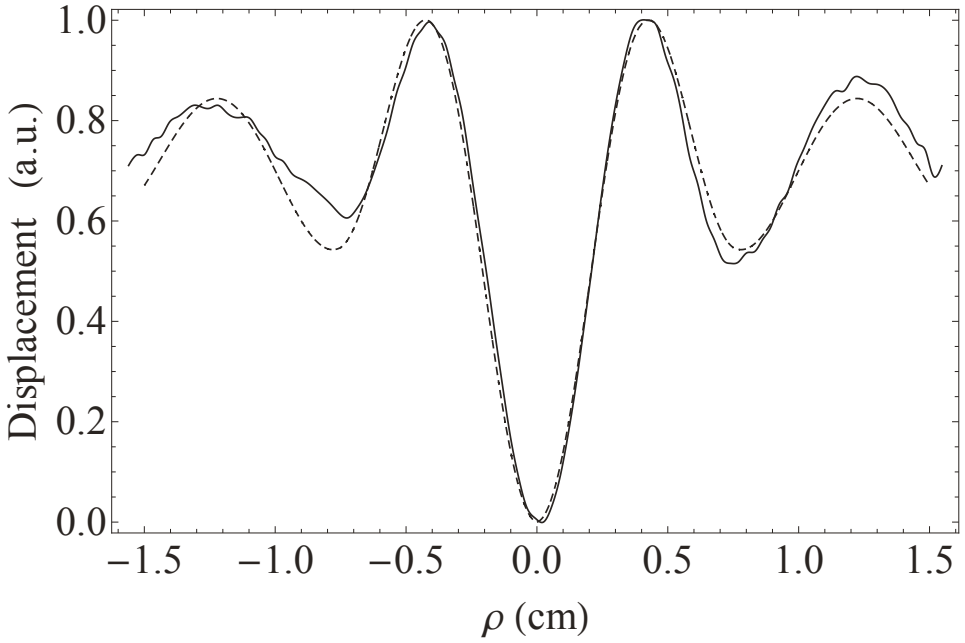

Figure 18. Comparison of the theoretic (dashed) to experimental (solid) displacements along a horizontal line through the fields in Figure 14

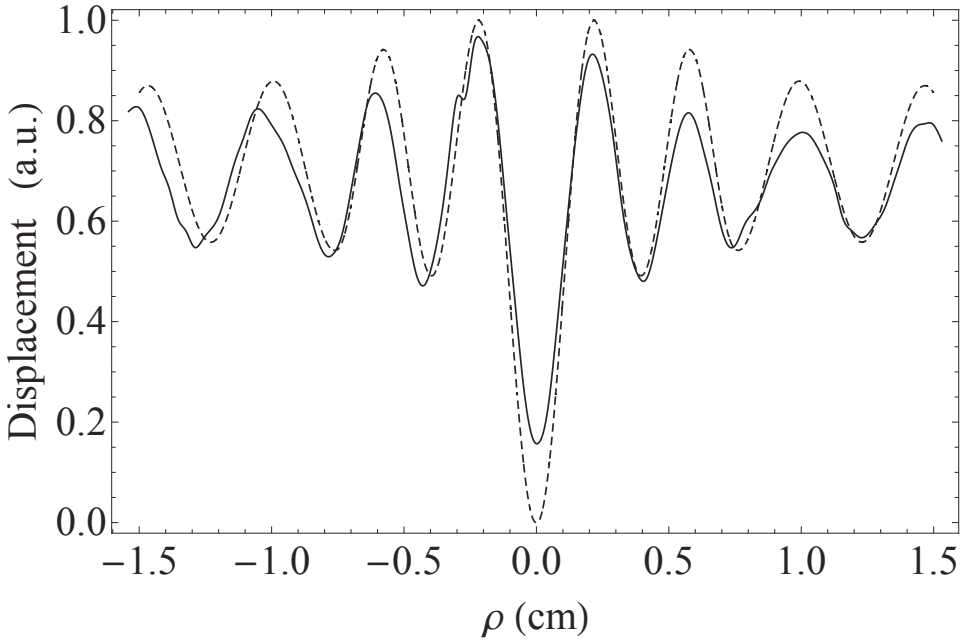

Figure 19. Comparison of the theoretic (dashed) to experimental (solid) displacements along a horizontal line through the fields in Figure 15

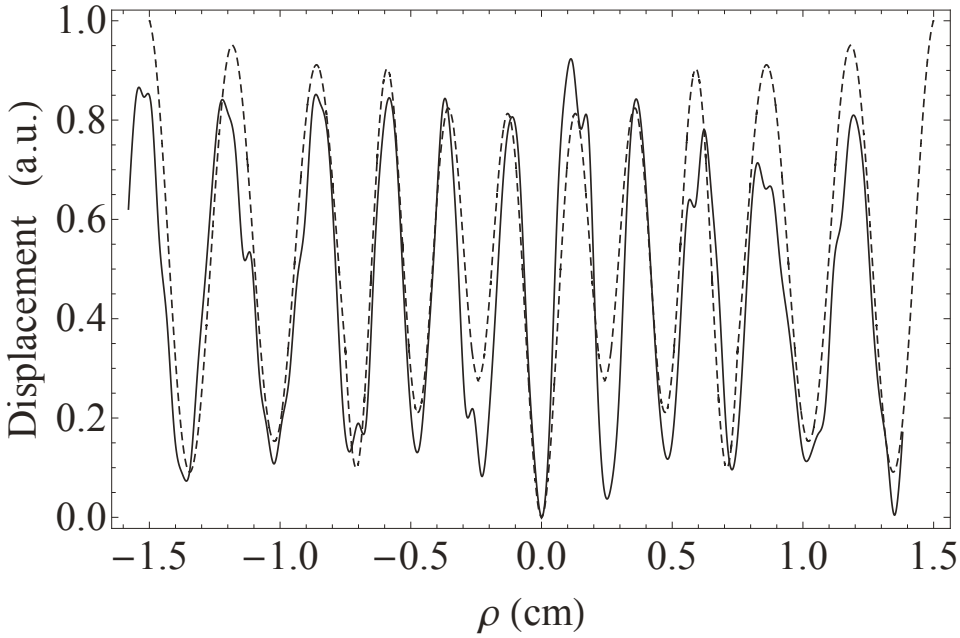

Figure 20. Comparison of the theoretic (dashed) to experimental (solid) displacements along a horizontal line through the fields in Figure 16

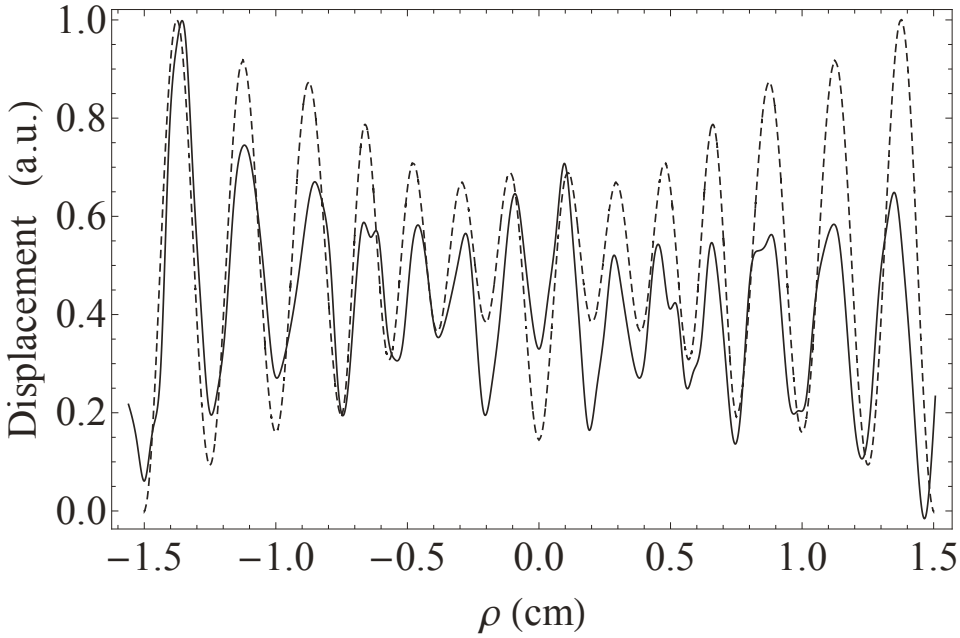

Figure 21. Comparison of the theoretic (dashed) to experimental (solid) displacements along a horizontal line through the fields in Figure 17

CHAPTER 3

SPHERICAL INCLUSION: THEORY

In this chapter, the scattering and diffraction of a cylindrically converging transverse shear wave in a viscoelastic isotropic medium by a spherical heterogeneity is analytically solved. The spherical inclusion is located at the radial center of the cylinder and differs from the cylindrical material only in its shear elastic constant. Small amplitude motion is assumed, such that linear system theory is valid. By employing multi-pole expansions, the incidental and scattered wave fields are each defined in both cylindrical and spherical coordinates allowing for the satisfaction of the boundary conditions at the surfaces of these multiply-connected bodies. The solution involves an infinite sum of improper integrals, which are evaluated numerically. The wave field is determined for a hydrogel (alginate) bead suspended in a different hydrogel (agarose) that fills a glass test tube. Numerical examples showing the effect on displacement fields of varying the stiffness of the inclusion are presented.

3.1 Introduction

With the goal of non-destructively monitoring the growth of engineered tissue in beads of hydrogel scaffolding, Yaşar et al (35; 42) pursued magnetic resonance (MR) elastography on the microscopic scale (μMRE), wherein high frequency displacements in the medium are discernible due to geometric focusing of the radially-converging circular cylindrical, shear waves. Briefly, a glass cylindrical tube is filled with a viscoelastic solid and harmonically vibrated along its

axis. Assuming a "welded" contact between the solid and rigid tube wall, the mechanical oscillations of the latter induce radially convergent circular cylindrical shear waves in the former. The analytic solution to that problem is generally straight forward. Such is not the case if a different elastic solid is embedded in the cylindrical medium that is a shape other than an infinite circular cylinder, e.g. a sphere. Over the past eight decades many researchers have studied mechanical problems involving a finite spherical heterogeneity centrally embedded in, or proximally external to, a cylindrical medium. Using Laplace's equation, Knight (43) studied the potential in a conducting cylinder with a spherical cavity. Kubenko et al. adopted this approach to solve the problems of pulsating (44) and potential (45) flow past a sphere in a rigid tube and thin elastic cylindrical shell, respectively, while Linton's work covers potential and Stokes flow around, and acoustic scattering by, a sphere in a cylinder (46). Smythe solved for the velocity field of the flow around a sphere (47) and a spheroid (48) in a tube, starting with the vector potential functions to insert into the governing Laplace equation. Cai and Wallis (49) extended Smythe's work to include an infinite row of spheres in a tube.

Several authors have studied the phenomenon of waves that travel along the length of the cylinder. Ursell (50) considered a rigid tube filled with an acoustic medium and a centrally-placed rigid sphere to demonstrate the existence of so-called trapped modes, where normal velocity vanishes on the surfaces. Linton (51) extended this to include both soft and hard cylinders and spheres, while Zhuk et al. (52) considered the radiation force on the sphere. Lee (53) examined the scattering of torsional waves down an elastic cylinder by a central spherical cavity though Golovchan (54) had solved that problem for infinitely many stacked spherical

cavities. Kubenko and Dzyuba wrote several papers where the spherical heterogeneity was the wave source, varying the type of cylindrical container and spherical inclusion. They include an oscillating and pulsating sphere in a rigid cylinder (55), a thin elastic cylindrical shell (56), and a thin elastic cylindrical shell immersed in an elastic medium (57; 58). Hasheminejad and Hosseini (59; 60) solved for the case when the acoustic medium fills a cylindrical cavity in an infinite poroelastic medium. Hosseiniand Namazi (61) applied the same coordinate transformations as above to solve for the case when the spherical wave source is external to an infinite circular cylindrical poroelastic cylinder, i.e a ball outside of a tube. Earlier, though, Li and Ueda (62) solved a very similar problem but assumed that the spherical waves could be modeled as a plane wave while Piquette (63) simplified matters by neglecting the radial component of the scattered wave. Adopting the integral equation formulation given by Ström (64), using the so-called T matrix method of Waterman (65), Olsson solved for a spherical cavity scattering a longitudinal wave propagating down a cylinder(66), waves from a perturbation at some point on the surface of the cylinder (67), as well as the scattering of elastic waves by a non-axisymmetric spherical cavity in a thick-walled pipe (68). Finally, it is worth mentioning that this ball in a tube formalism extends far beyond acoustics, having been used by Kim et al. (69) to solve for the quantum scattering potential of atomic matter waves and by Otey and Fan (70) to solve for the electromagnetic heat transfer between a sphere and a plate. Presently, we will cast the problem in terms of differential, rather then integral, equations. Whereas Linton and Kubenko used the scalar Helmholtz equation, the elastic nature of our problem calls for the vector Helmholtz equation. Golovchan (54) and Lee (53) both studied problems of elastic waves in cylinders with

spherical obstacles, but they include only transverse, torsional waves, parallel to the boundaries. This produced no mode conversion, leaving only one type of wave to comprise the wave field. The present study, then, is the first to use differential equations to solve the problem of elastic wave diffraction, in this particular geometry, under conditions that involve both longitudinal and transverse wave fields.

3.2 Problem Formulation

Let there be given an infinitely long, rigid, circular cylindrical tube of inner radius b, filled with an elastic solid. Embedded therein is an elastic sphere (ball) whose center is on the axis of the tube. The tube and the embedded ball are respectively described by cylindrical (ρ, ϕ, z) and spherical (r, θ, ϕ) coordinates (71), shown in Figure 22. The $\hat{z}$ axis is aligned with the axis of the tube and contains the center of the spherical inclusion. The rigid tube harmonically oscillates along the cylindrical z axis and it is assumed that the embedding material (medium 1) is in intimate contact with both the spherical inclusion (medium 2) and the oscillating wall. The displacement of both media satisfy the vector Helmholtz equation,

$$\alpha_i^2 \nabla\nabla \cdot \vec{U} - \beta_i^2 \nabla \times \nabla \times \vec{U} + \omega^2 \vec{U} = 0 \tag{3.1}$$

where

$$\alpha_i^2 = (\lambda_i + 2\mu_i)\gamma_i^{-1} \ (i = 1, 2), \tag{3.2a}$$

$$\beta_i^2 = \mu_i \gamma_i^{-1} \ (i = 1, 2). \tag{3.2b}$$

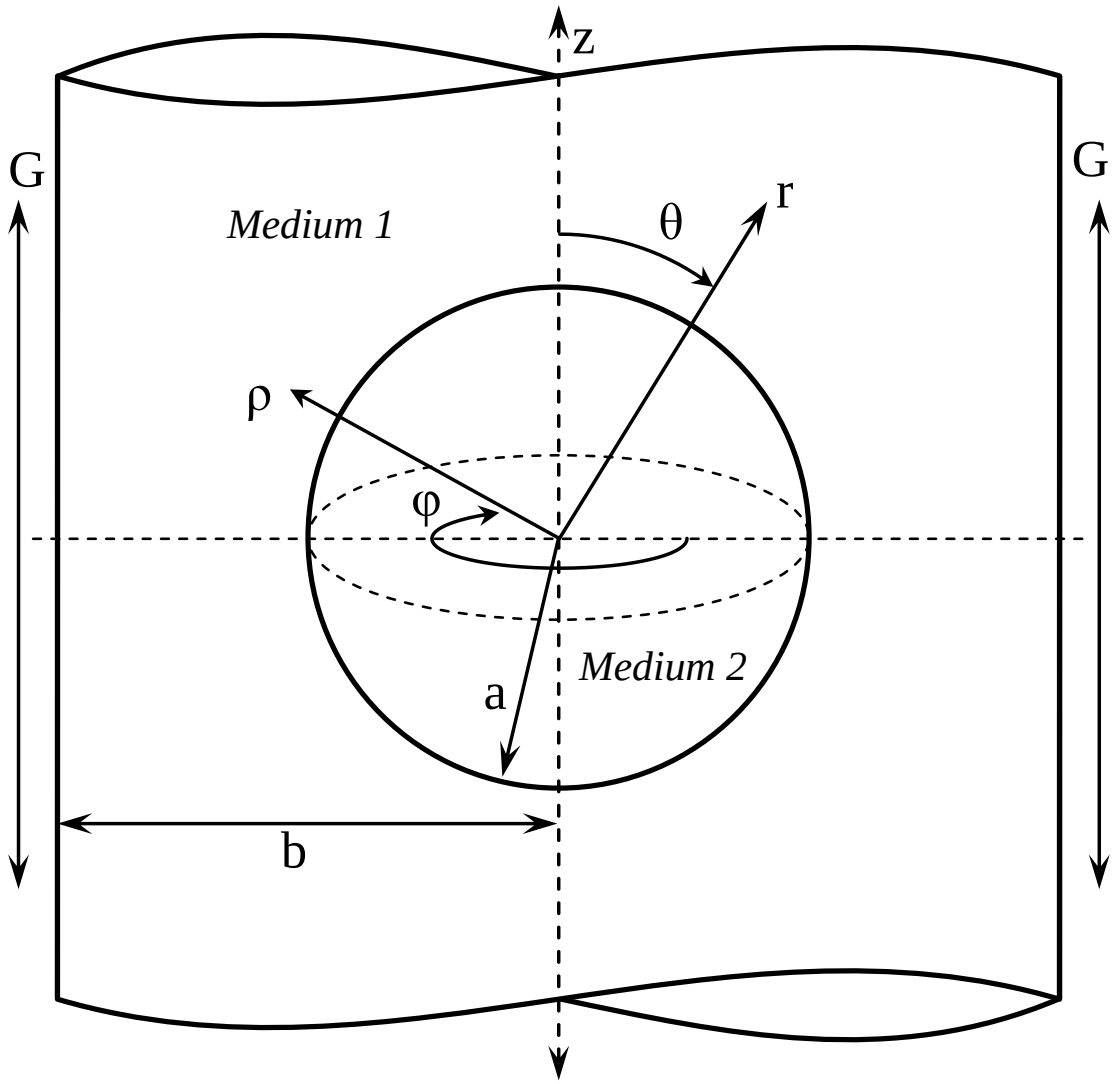

Figure 22. The cylindrical medium, medium 1, is referred to a cylindrical coordinate system, r and z, with the z axis coinciding with the axis of medium 1. The spherical coordinates, r and θ, are assigned to the center of the spherical inclusion, medium 2.

The constants, λ_i, and μ_i, are the Lame constants, and γ_i is the density of a material. It is held that $\lambda_i = (2\mu_i\nu)/(1-2\nu)$ for both media, where ν is the Poisson ratio. Here the index i is 1 or 2 to denote the medium. The harmonic time dependence, $e^{-i\omega t}$, is suppressed throughout this study. The boundary conditions of the cylindrical surface, due to the welded contact, are equality of the normal and axial displacements of the elastic medium and wall

$$u_{1\rho}(\rho, z)\big|_{\rho=b} = 0, \tag{3.3a}$$

$$u_{1z}(\rho, z)\big|_{\rho=b} = G \tag{3.3b}$$

where G is the amplitude of the forced oscillations. At the spherical surface, the boundary conditions, also due to the welded contact, are equality of the radial and polar displacements of the two media,

$$u_{1r}(r, \theta)\big|_{r=a} = u_{2r}(r, \theta)\big|_{r=a}\,, \tag{3.4a}$$

$$u_{1\theta}(r, \theta)\big|_{r=a} = u_{2\theta}(r, \theta)\big|_{r=a}\,, \tag{3.4b}$$

and equality of the stresses between the two media,

$$\sigma_{1rr}(r, \theta)\big|_{r=a} = \sigma_{2rr}(r, \theta)\big|_{r=a}\,, \tag{3.5a}$$

$$\sigma_{1r\theta}(r, \theta)\big|_{r=a} = \sigma_{2r\theta}(r, \theta)\big|_{r=a}\,. \tag{3.5b}$$

The solution of (Equation 3.1) can be given as the sum of the vector wave functions, $\vec{L}$, $\vec{M}$, and $\vec{N}$ given as

$$\vec{L} = \nabla\Phi, \tag{3.6a}$$

$$\vec{M} = \nabla \times \hat{e}\Psi, \tag{3.6b}$$

$$\vec{N} = \beta_i^{-1}\nabla \times \nabla \times \hat{e}\mathrm{X}, \tag{3.6c}$$

where Φ, Ψ, and X each solves the scalar Helmholtz equation,

$$\left(\nabla^2 + \alpha_i^{-2}\right)\Phi = 0, \tag{3.7a}$$

$$\left(\nabla^2 + \beta_i^{-2}\right)\Psi = 0, \tag{3.7b}$$

$$\left(\nabla^2 + \beta_i^{-2}\right)\mathrm{X} = 0, \tag{3.7c}$$

and $\hat{e}$ is a constant vector (1). The displacement in medium 1 is the sum of the incidental and scattered wave fields, $\vec{U}^{(i)}$ and $\vec{U}^{(s)}$, respectively, while the displacement in medium 2 is from the refracted wave field only, $\vec{U}^{(r)}$. Due to the axial symmetry of the system, of concern are only the longitudinal and vertically-polarized transverse waves, i.e. $\vec{M} = 0$ for all wave fields. The wave fields are, then, given as

$$\vec{U}^{(i)} = \vec{L}^{(i)} + \vec{N}^{(i)}, \tag{3.8a}$$

$$\vec{U}^{(s)} = \vec{L}^{(s)} + \vec{N}^{(s)}, \tag{3.8b}$$

$$\vec{U}^{(r)} = \vec{L}^{(r)} + \vec{N}^{(r)}. \tag{3.8c}$$

In cylindrical coordinates, the constant vector is the unit vector, $\hat{z}$. The vector functions are then given as (37)

$$\vec{L}_{\text{cyl}} = \frac{\partial \Phi_{\text{cyl}}}{\partial \rho}\hat{\rho} + \frac{\partial \Phi_{\text{cyl}}}{\partial z}\hat{z}, \tag{3.9a}$$

$$\vec{N}_{\text{cyl}} = \frac{1}{q_i}\frac{\partial^2 \text{X}_{\text{cyl}}}{\partial \rho \partial z}\hat{\rho} + \frac{1}{q_i r}\frac{\partial}{\partial r}\left(r\frac{\partial \text{X}_{\text{cyl}}}{\partial r}\right)\hat{z}, \tag{3.9b}$$

from which can be written the displacement components,

$$u_\rho = \frac{\partial \Phi_{\text{cyl}}}{\partial \rho} + \frac{1}{q_i}\frac{\partial^2 \text{X}_{\text{cyl}}}{\partial \rho \partial z}, \tag{3.10a}$$

$$u_z = \frac{\partial \Phi_{\text{cyl}}}{\partial z} + \frac{1}{q_i r}\frac{\partial}{\partial r}\left(r\frac{\partial \text{X}_{\text{cyl}}}{\partial r}\right). \tag{3.10b}$$

In spherical coordinates the constant vector is $r\hat{r}$ and the vector functions are given as (72)

$$\vec{L}_{\text{sph}} = \frac{\partial \Phi_{\text{sph}}}{\partial r}\hat{r} + \frac{1}{r}\frac{\partial \Phi_{\text{sph}}}{\partial \theta}\hat{\theta}, \tag{3.11a}$$

$$\vec{N}_{\text{sph}} = \frac{1}{q_i}\left(\frac{\partial^2 r\text{X}_{\text{sph}}}{\partial r^2} - \frac{1}{r^2}\frac{\partial}{\partial r}\left(r^2\frac{\partial \text{X}_{\text{sph}}}{\partial r}\right) - \frac{1}{r^2\sin(\theta)}\frac{\partial}{\partial \theta}\left(\sin(\theta)\frac{\partial \text{X}_{\text{sph}}}{\partial \theta}\right)\right)\hat{r} + \frac{1}{r}\frac{\partial^2 r\text{X}_{\text{sph}}}{\partial r \partial \theta}\hat{\theta}, \tag{3.11b}$$

whence

$$u_r = \frac{\partial \Phi_{\text{sph}}}{\partial r} + \frac{1}{q_i}\left(\frac{\partial^2 r \mathrm{X}_{\text{sph}}}{\partial r^2} - \frac{1}{r^2}\frac{\partial}{\partial r}\left(r^2 \frac{\partial \mathrm{X}_{\text{sph}}}{\partial r}\right) - \frac{1}{r^2 \sin(\theta)}\frac{\partial}{\partial \theta}\left(\sin(\theta)\frac{\partial \mathrm{X}_{\text{sph}}}{\partial \theta}\right)\right), \tag{3.12a}$$

$$u_\theta = \frac{1}{r}\frac{\partial \Phi_{\text{sph}}}{\partial \theta} + \frac{1}{r}\frac{\partial^2 r \mathrm{X}_{\text{sph}}}{\partial r \partial \theta}. \tag{3.12b}$$

The relevant components of the stress tensor, σ_{rr} and $\sigma_{r\theta}$, can be calculated directly from the displacement, given here as

$$\sigma_{rr} = \lambda\left(\frac{\partial u_r}{\partial r} + \frac{1}{r}\frac{\partial u_\theta}{\partial \theta} + 2\frac{u_r}{r} + \frac{\cot(\theta)}{r}u_\theta\right) + 2\mu\frac{\partial u_r}{\partial r}, \tag{3.13a}$$

$$\sigma_{r\theta} = \mu\left(\frac{1}{r}\frac{\partial u_r}{\partial \theta} - \frac{u_\theta}{r} + \frac{\partial u_\theta}{\partial r}\right). \tag{3.13b}$$

3.3 Solutions

For the incidental wave, the scalar potential functions, $\Phi^{(i)}_{\text{cyl}}$ and $\mathrm{X}^{(i)}_{\text{cyl}}$, are given as

$$\Phi^{(i)}_{\text{cyl}}(\rho, z) = \int_{-\infty}^{\infty} A(\xi) J_0(g\rho)\, e^{i\xi z} d\xi, \tag{3.14a}$$

$$\mathrm{X}^{(i)}_{\text{cyl}}(\rho, z) = \int_{-\infty}^{\infty} B(\xi) J_0(h\rho)\, e^{i\xi z} d\xi, \tag{3.14b}$$

where $g = \sqrt{p_1^2 - \xi^2}$, $h = \sqrt{q_1^2 - \xi^2}$, $p_1 = \omega/\alpha_1$, $q_1 = \omega/\beta_1$, and $A(\xi)$ and $B(\xi)$ are unknown functions. The scattered and refracted scalar potential functions, $\Phi_{\text{sph}}^{(s)}$, $\Phi_{\text{sph}}^{(r)}$, $\text{X}_{\text{sph}}^{(s)}$ and $\text{X}_{\text{sph}}^{(r)}$, are given as

$$\Phi_{\text{sph}}^{(s)}(r,\theta) = \sum_{n=0}^{\infty} C_n h_n(p_1 r) P_n\left(\cos(\theta)\right), \tag{3.15a}$$

$$\Phi_{\text{sph}}^{(r)}(r,\theta) = \sum_{n=0}^{\infty} E_n j_n(p_2 r) P_n\left(\cos(\theta)\right), \tag{3.15b}$$

$$\text{X}_{\text{sph}}^{(s)}(r,\theta) = \sum_{n=0}^{\infty} D_n h_n(q_1 r) P_n\left(\cos(\theta)\right), \tag{3.15c}$$

$$\text{X}_{\text{sph}}^{(r)}(r,\theta) = \sum_{n=0}^{\infty} F_n j_n(q_2 r) P_n\left(\cos(\theta)\right), \tag{3.15d}$$

where C_n, D_n, E_n, and F_n are unknown coefficients. To satisfy the boundary condition, thereby determining all unknown functions and coefficients, the incidental and scattered wave fields must be defined in terms of both cylindrical and spherical coordinates. To do this the following transformations are used (73; 74; 75):

$$\vec{L}_{\text{sph}}(\rho,z) = (i^n 2k)^{-1} \int_{-\infty}^{\infty} P_n\left(\frac{\xi}{k}\right) \vec{L}_{\text{cyl}} d\xi, \tag{3.16a}$$

$$\vec{N}_{\text{sph}}(\rho,z) = \left(i^{n-1} 2k\right)^{-1} \int_{-\infty}^{\infty} \sin(\alpha) \frac{\partial}{\partial \alpha} P_n\left(\cos(\alpha)\right) \vec{N}_{\text{cyl}} d\xi, \tag{3.16b}$$

where $\alpha = \arccos(\xi/k)$. Considering (Equation 3.15), one can write the scalar potential functions of the scattered wave in cylindrical coordinates,

$$\Phi^{(s)}_{\text{sph}}(\rho, z) = \int_{-\infty}^{\infty} C(\xi) H_0\left(g\rho\right) e^{i\xi z} d\xi, \tag{3.17a}$$

$$\mathrm{X}^{(s)}_{\text{sph}}(\rho, z) = \int_{-\infty}^{\infty} D(\xi) H_0\left(h\rho\right) e^{i\xi z} d\xi, \tag{3.17b}$$

where

$$C(\xi) = (2p_1)^{-1} \sum_{n=0}^{\infty} C_m i^{-m} P_n\left(\frac{\xi}{k}\right), \tag{3.18a}$$

$$D(\xi) = (2q_1)^{-1} \sum_{n=0}^{\infty} D_m i^{1-m} (m+1) \left(q_1 P_{m+1}\left(\frac{\xi}{q_1}\right) - \xi P_m\left(\frac{\xi}{q_1}\right)\right). \tag{3.18b}$$

To write cylindrical waves in spherical coordinates the following transformations are used (73; 74; 75):

$$\vec{L}_{\text{cyl}}(r, \theta) = \sum_{n=0}^{\infty} i^n (2n+1) P_n\left(\frac{\xi}{k}\right) \vec{L}_{\text{sph}}, \tag{3.19a}$$

$$\vec{N}_{\text{cyl}}(r, \theta) = \sum_{n=0}^{\infty} \frac{2n+1}{n(n+1)} i^{n+1} \sin(\alpha) \frac{\partial}{\partial \alpha} P_n\left(\cos(\alpha)\right) k \vec{N}_{\text{sph}}. \tag{3.19b}$$

One may now write the scalar potential functions of the incidental wave as

$$\Phi^{(i)}_{\text{cyl}}(r, \theta) = \sum_{n=0}^{\infty} A_n j_n\left(p_1 r\right) P_n\left(\cos(\theta)\right), \tag{3.20a}$$

$$\mathrm{X}^{(i)}_{\text{cyl}}(r, \theta) = \sum_{n=0}^{\infty} B_n j_n\left(q_1 r\right) P_n\left(\cos(\theta)\right), \tag{3.20b}$$

where

$$A_n = i^n(2n+1)\int_{-\infty}^{\infty} A(\xi)P_n\left(\frac{\xi}{k}\right)d\xi, \tag{3.21a}$$

$$B_n = \frac{2n+1}{n(n+1)}i^{n+1}\int_{-\infty}^{\infty} B(\xi)y(\xi)d\xi, \tag{3.21b}$$

and

$$y(\xi) = \frac{1}{q_1}(m+1)\left(\xi P_m\left(\frac{\xi}{q_1}\right) - q_1 P_{m+1}\left(\frac{\xi}{q_1}\right)\right). \tag{3.22}$$

Here, J_n and j_n are the cylindrical and spherical Bessel functions of the first kind of order n, respectively, while P_n is the Legendre polynomial of order n. Also, H_n and h_n are the cylindrical and spherical Hankel functions of the first kind of order n, respectively (4). Finally, as the spherical refracted wave does not contact the cylindrical boundary, the potential functions need only be given in spherical coordinates. The first kind of cylindrical and spherical Bessel functions are chosen for the incidental and refracted wave fields, respectively, because those functions are not singular when their argument is zero and those wave fields contain the radial origin of their respective coordinate systems. Let there be introduced dimensionless variables

$$\bar{\rho} = \frac{\rho}{b},\ \bar{r} = \frac{r}{b},\ \bar{U} = \frac{U}{b},\ \bar{p_i} = p_i b,\ \bar{q_i} = q_i b,\ \bar{z} = \frac{z}{b}. \tag{3.23}$$

Hereafter, only use dimensionless variables will be used; so, the over-bar will be omitted.

3.4 Boundary Conditions

Let first be considered the cylindrical boundary conditions. It is convenient to work in the frequency domain so let the Fourier transform be applied in z,

$$f(\xi) = \int_{-\infty}^{\infty} f(z) e^{-i\xi z} dz, \tag{3.24}$$

to (Equation 3.3), and taking into account (Equation 3.10), (Equation 3.14b), and (Equation 3.17b), one obtains expressions relating the axial and radial displacements of medium 1 and the oscillating wall:

$$gq_1 \left(A(\xi)J_1(gr) + C(\xi)H_1(gr)\right) + ih\xi \left(D(\xi)H_1(hr) + B(\xi)J_1(hr)\right) = 0 \tag{3.25a}$$

$$i\xi q_1 \left(A(\xi)J_0(gr) + C(\xi)H_0(gr)\right) - h^2 \left(D(\xi)H_0(hr) + B(\xi)J_0(hr)\right) = Gq_1. \tag{3.25b}$$

From Equation 3.25 one can write the unknown functions of the incidental wave, $A(\xi)$ and $B(\xi)$, in terms of the unknown coefficients of the scattered wave, C_m and D_m, i.e.

$$A(\xi) = \sum_{m=0}^{\infty} \left(C_m a_m(\xi) + D_m b_m(\xi)\right) - c(\xi), \tag{3.26a}$$

$$B(\xi) = \sum_{m=0}^{\infty} \left(C_m d_m(\xi) + D_m e_m(\xi)\right) - f(\xi), \tag{3.26b}$$

where

$$a_m(\xi) = \frac{i^{-m} P_m\left(\xi/p_1\right)\left(\xi^2 J_1(bh)H_0(bg) - ghJ_0(bh)H_1(bg)\right)}{(2p_1 x(\xi))}, \tag{3.27a}$$

$$b_m(\xi) = \frac{i^{1-m} y(\xi) h\xi}{\left(b\pi q_1^2 x(\xi)\right)}, \tag{3.27b}$$

$$c(\xi) = \frac{iG\xi J_1(bh)}{x(\xi)}, \tag{3.27c}$$

$$d_m(\xi) = \frac{\xi P_m\left(\xi/p_1\right) q_1}{(i^m b\pi h p_1 x(\xi))}, \tag{3.27d}$$

$$e_m(\xi) = \frac{i^{1-m} y(\xi)\left(ghJ_1(bg)H_0(bh) - \xi^2 J_0(bh)H_1(bh)\right)}{(2q_1 x(\xi))}, \tag{3.27e}$$

$$f(\xi) = \frac{gGJ_1(bg)}{(hx(\xi))}, \tag{3.27f}$$

and

$$x(\xi) = ghJ_0(bh)J_1(bg) - \xi^2 J_0(bg)J_1(bh). \tag{3.28}$$

From Equation 3.20 and Equation 3.26, then, one has

$$A_n = \sum_{m=0}^{\infty} \left(C_m a_{mn} + D_m b_{mn}\right) - c_n, \tag{3.29a}$$

$$B_n = \sum_{m=0}^{\infty} (C_m d_{mn} + D_m e_{mn}) - f_n. \tag{3.29b}$$

When $m + n$ is even, one has

$$a_{mn} = i^n (2n+1) \int_{-\infty}^{\infty} a_m(\xi) P_n(\xi/p_1)\, d\xi, \tag{3.30a}$$

$$b_{mn} = i^n (2n+1) \int_{-\infty}^{\infty} b_m(\xi) P_n(\xi/p_1)\, d\xi, \tag{3.30b}$$

$$d_{mn} = \frac{2n+1}{n(n+1)} i^{n+1} \int_{-\infty}^{\infty} d_m(\xi) y(\xi)\, d\xi, \tag{3.30c}$$

$$e_{mn} = \frac{2n+1}{n(n+1)} i^{n+1} \int_{-\infty}^{\infty} e_m(\xi) y(\xi)\, d\xi, \tag{3.30d}$$

otherwise $a_{mn} = b_{mn} = d_{mn} = e_{mn} = 0$. When $m + n$ is odd, one has

$$c_n = i^n (2n+1) \int_{-\infty}^{\infty} c(\xi) P_n(\xi/p_1)\, d\xi, \tag{3.31a}$$

$$f_n = \frac{2n+1}{n(n+1)} i^{n+1} \int_{-\infty}^{\infty} f(\xi) y(\xi)\, d\xi, \tag{3.31b}$$

otherwise $c_n = f_n = 0$. At the spherical boundary ($r = a$) one has expressions that relate the displacements and stresses of the two media,

$$\mathbf{T}_n \left(A_n B_n C_n D_n E_n F_n\right)^{\mathrm{T}} = 0 \ (n = \overline{0, \infty}), \tag{3.32}$$

where $\mathbf{T}_n$ is a four-by-six matrix whose elements, τ_{ij} ($i = \overline{1,4}$ and $j = \overline{1,6}$), are determined from Equation 3.4, Equation 3.5, Equation 3.12, Equation 3.13, Equation 3.15, and Equation 3.20, and given here as (76)

$$\tau_{11} = nj_n(ap_1) - p_1 aj_{n+1}(ap_1), \tag{3.33a}$$

$$\tau_{12} = -n(n+1)j_n(aq_1), \tag{3.33b}$$

$$\tau_{13} = p_1 ah_{n+1}(ap_1) - nh_n(ap_1), \tag{3.33c}$$

$$\tau_{14} = n(n+1)h_n(aq_1), \tag{3.33d}$$

$$\tau_{15} = nj_n(ap_2) - p_2 aj_{n+1}(ap_2), \tag{3.33e}$$

$$\tau_{16} = -n(n+1)j_n(aq_2), \tag{3.33f}$$

$$\tau_{21} = j_n(ap_1), \tag{3.33g}$$

$$\tau_{22} = (n+1)j_n(aq_1) - q_1 aj_{n+1}(aq_1), \tag{3.33h}$$

$$\tau_{23} = h_n(ap_1), \tag{3.33i}$$

$$\tau_{24} = (n+1)h_n(aq_1) - q_1 ah_{n+1}(aq_1), \tag{3.33j}$$

$$\tau_{25} = j_n(ap_2), \tag{3.33k}$$

$$\tau_{26} = (n+1)j_n(aq_2) - q_2 aj_{n+1}(aq_2), \tag{3.33l}$$

$$\tau_{31} = \left(n^2 - n - 0.5q_1^2a^2\right) j_n(ap_1) + 2p_1aj_{n+1}(ap_1), \tag{3.33m}$$

$$\tau_{32} = n(n+1)((1-n)j_n(aq_1) + q_1aj_{n+1}(aq_1)), \tag{3.33n}$$

$$\tau_{33} = \left(n^2 - n - 0.5q_1^2a^2\right) h_n(ap_1) + 2p_1ah_{n+1}(ap_1), \tag{3.33o}$$

$$\tau_{34} = n(n+1)((1-n)h_n(aq_1) + q_1ah_{n+1}(aq_1)), \tag{3.33p}$$

$$\tau_{35} = \left(n^2 - n - 0.5q_2^2a^2\right) j_n(ap_2) + 2p_2aj_{n+1}(ap_2), \tag{3.33q}$$

$$\tau_{36} = n(n+1)((1-n)j_n(aq_2) + q_2aj_{n+1}(aq_2)), \tag{3.33r}$$

$$\tau_{41} = (n-1)j_n(ap_1) - p_1aj_{n+1}(ap_1), \tag{3.33s}$$

$$\tau_{42} = \left(1 - n^2 + 0.5q_1^2a^2\right) j_n(aq_1) - q_1aj_{n+1}(aq_1), \tag{3.33t}$$

$$\tau_{43} = (n-1)h_n(ap_1) - p_1ah_{n+1}(ap_1), \tag{3.33u}$$

$$\tau_{44} = \left(1 - n^2 + 0.5q_1^2a^2\right) h_n(aq_1) - q_1ah_{n+1}(aq_1), \tag{3.33v}$$

$$\tau_{45} = (n-1)j_n(ap_2) - p_2aj_{n+1}(ap_2), \tag{3.33w}$$

$$\tau_{46} = \left(1 - n^2 + 0.5q_2^2a^2\right) j_n(aq_2) - q_2aj_{n+1}(aq_2). \tag{3.33x}$$

Inserting Equation 3.29 into Equation 3.32, the following infinite system of equations are obtained in the unknowns C_n, D_n, E_n, and F_n,

$$\varepsilon_{i3}C_n + \sum_{m=1}^{\infty} x_{mn}C_m + \varepsilon_{i4}D_n + \sum_{m=1}^{\infty} y_{mn}D_m - \varepsilon_{i5}E_n - \varepsilon_{i6}F_n = z_i \ (n = \overline{1,\infty}), \tag{3.34}$$

where

$$x_{mn} = a_{mn}\varepsilon_{i1} + d_{mn}\varepsilon_{i2}, \tag{3.35a}$$

$$y_{mn} = b_{mn}\varepsilon_{i1} + e_{mn}\varepsilon_{i2}, \tag{3.35b}$$

$$z_i = \varepsilon_{i1}c_n + \varepsilon_{i2}f_n. \tag{3.35c}$$

The expressions for C_n and D_n may then be inserted in to Equation 3.26, thereby completely determining all wave fields.

3.5 Numeric Examples and Discussion

The behavior of our model is demonstrated with some numeric examples. To solve Equation 3.34 numerically, the method of truncation is used (77), wherein the infinite system of equations is reduced to a system of N equations, i.e. $m = \overline{1,N}$ and $n = \overline{1,N}$. The order of truncation was determined by trial so that the boundary conditions were satisfied with adequate accuracy. Hosseini et al (61) report that they require $N = p+5$ where p is the maximum nondimensional wave number on the graphs. This is true here, too, but for the transverse wave number q, rather than the longitudinal wave number p. This speaks to the motivation of this study. Microscale MRE (24) is concerned with transverse wave propagation through tissues,

i.e. viscoelastic media, because the longitudinal wavelength exceeds the physical dimensions of the phantoms in the studies of e.g. Yaşar et al. (35) and Okamoto et al. (36).

To evaluate the integrals in Equation 3.30 and Equation 3.31 the upper infinite limit is replaced with a finite limit such that the value stabilized to, at least, the sixth decimal place. All of the integrands in these equations have singular points at the zeroes of Equation 3.28 as well as branch points when $\xi = p_1$ and $\xi = q_1$. In other studies, e.g. the works of Olsson (66; 67; 68), these singularities have required that the contour of integration be deformed such that it passes into the second and fourth quadrants of the complex plane. One need not make use of such techniques because the materials in the examples of the present study are modeled as having complex, i.e. viscoelastic, moduli. This moves all singularities and branch points off of the real axis (78), simplifying numeric integration.

In the following examples our attention is confined to varying the stiffness of the spherical inclusion, μ_2, recognizing, though, that this formulation allows analysis of the effects of the changes of all parameters, e.g. the ratio of radii (a/b) or the damping ratio ($\mathfrak{Im}\mu_i/\mathfrak{Re}\mu_i$), on the displacement of the wave field. In all examples, $a/b = 0.5$, $\mathfrak{Im}\mu_i/\mathfrak{Re}\mu_i = 0.2$, the densities are $\gamma_1 = \gamma_2 = 1000$ kg/m^3, the excitation frequency is $\omega = 2\pi f$, where $f = 500$ Hz, and $\mu_1 = 7500 - 1500i$ Pa. Those material properties were chosen because they have been shown to characterize hydrogels (36) used in MRE phantoms. One assumes that, like water, they are nearly incompressible and have a finite bulk modulus. To satisfy these assumptions the Poisson ratio, ν, is held to be 0.4999998 in both media. The parameters are summarized in Table V. Experimental considerations inform the frequency choice. As an imaging tool,

TABLE V

Summary of the mechanical parameter values for the numeric examples.

Poisson ratio, ν	0.4999998
Spherical radius, a (cm)	0.75
Clyndrical radius, b (cm)	1.5
Displacement amplitude, G (μm)	1
Density, $\gamma_{1,2}$ (kg/m^3)	1000
Excitation frequency, f (Hz)	500
Medium 1 shear stiffness, μ_1 (kPa)	$7.5 - i1.5$
Truncation limit, N	38

MRE needs to clearly and easily show a researcher exactly where a heterogeneity sits in a field of view. This is impossible if the frequency is so low that the wavelength is longer than the field of view. There is a practical upper limit to the frequency, too. In soft tissue high frequency vibrations are preferentially attenuated and would eventually overcome the effect of geometric focusing in our system. Additionally, as more wavelengths are visible in the field of view, the higher is the degree of truncation which would, in turn, increase the computation time. All analytic computations were done with Mathematica 9 (Wolfram Research, Champaign, Illinois) on a desktop computer running Windows 7 Ultimate. The processor was an Intel®Core$^{\text{TM}}$i5-2500K central processing unit at 3.30 GHz, with 7.71 usable GB of installed memory, and a 64-bit operating system. Every displacement calculation took approximately 3.1 seconds, which

meant that each planar image took about 8 hours to render. Figure 23, Figure 24, Figure 25, Figure 26, and Figure 27 show the stationary displacement field for five different moduli of medium 2, i.e $\mu_2 = 2.5 - 0.5i$ kPa, $\mu_2 = 5 - 1i$ kPa, $\mu_2 = 7.5 - 1.5i$ kPa, $\mu_2 = 10 - 2i$ kPa, and $\mu_2 = 12.5 - 2.5i$ kPa, respectively.

In those displacement figures, the left top image is the coronal plane with the cylindrical axis and containing the spherical center, and the left bottom image is the axial plane, perpendicular to the cylindrical axis and also containing the spherical center. The axial views is at $z = 0$, indicated by a white line on the coronal views. The dotted gray circle indicates the orthodrome of the spherical inclusion. As expected, the region occupied by medium 2 can easily be distinguished from the surrounding medium 1 when the former is stiffer (Figure 23 and Figure 24) or softer (Figure 26 and Figure 27) than the latter. Figure 25 shows the limiting case of a sphere whose modulus equals that of medium 1. When $\mu_1 = \mu_2$ the system is effectively homogeneous, having an identical wavefield to those studied by Yaşar et al. (35). The right image shows the displacement as a function of the radius, corresponding to the white line on the coronal and axial views, for the analytic solution.

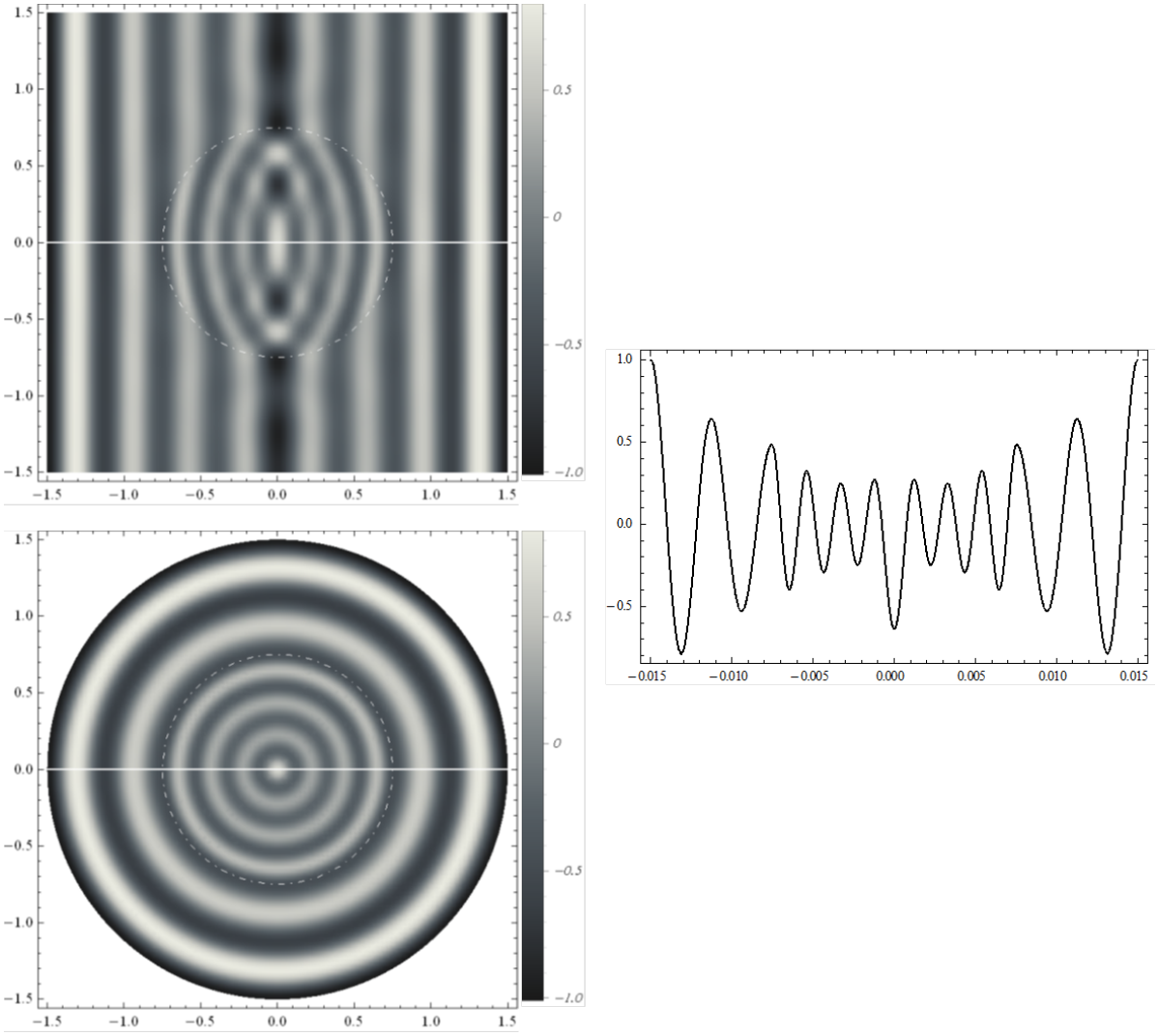

Figure 23. Wave field through a plane, containing the origin, parallel (top left) and perpendicular (bottom right) to the cylindrical axis. The line profile on the right comes from the white line on the wave fields. The complex shear moduli of the embedding medium and spherical inclusion are $\mu_1 = 7.5 - 1.5i$ kPa and $\mu_2 = 2.5 - 0.5i$ kPa, respectively.

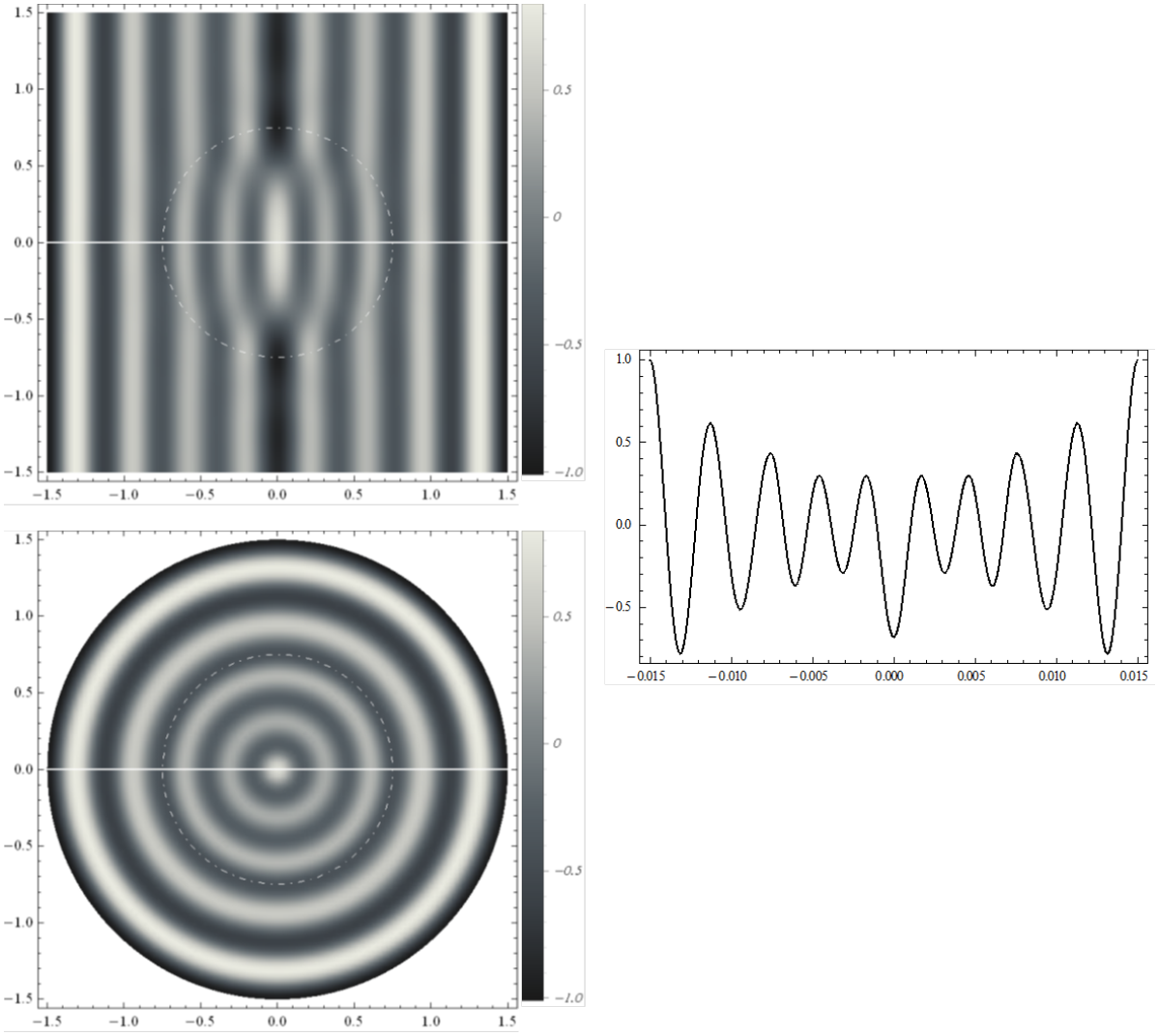

Figure 24. Wave field through a plane, containing the origin, parallel (top left) and perpendicular (bottom right) to the cylindrical axis. The line profile on the right comes from the white line on the wave fields. The complex shear moduli of the embedding medium and spherical inclusion are $\mu_1 = 7.5 - 1.5i$ kPa and $\mu_2 = 5 - 1i$ kPa, respectively.

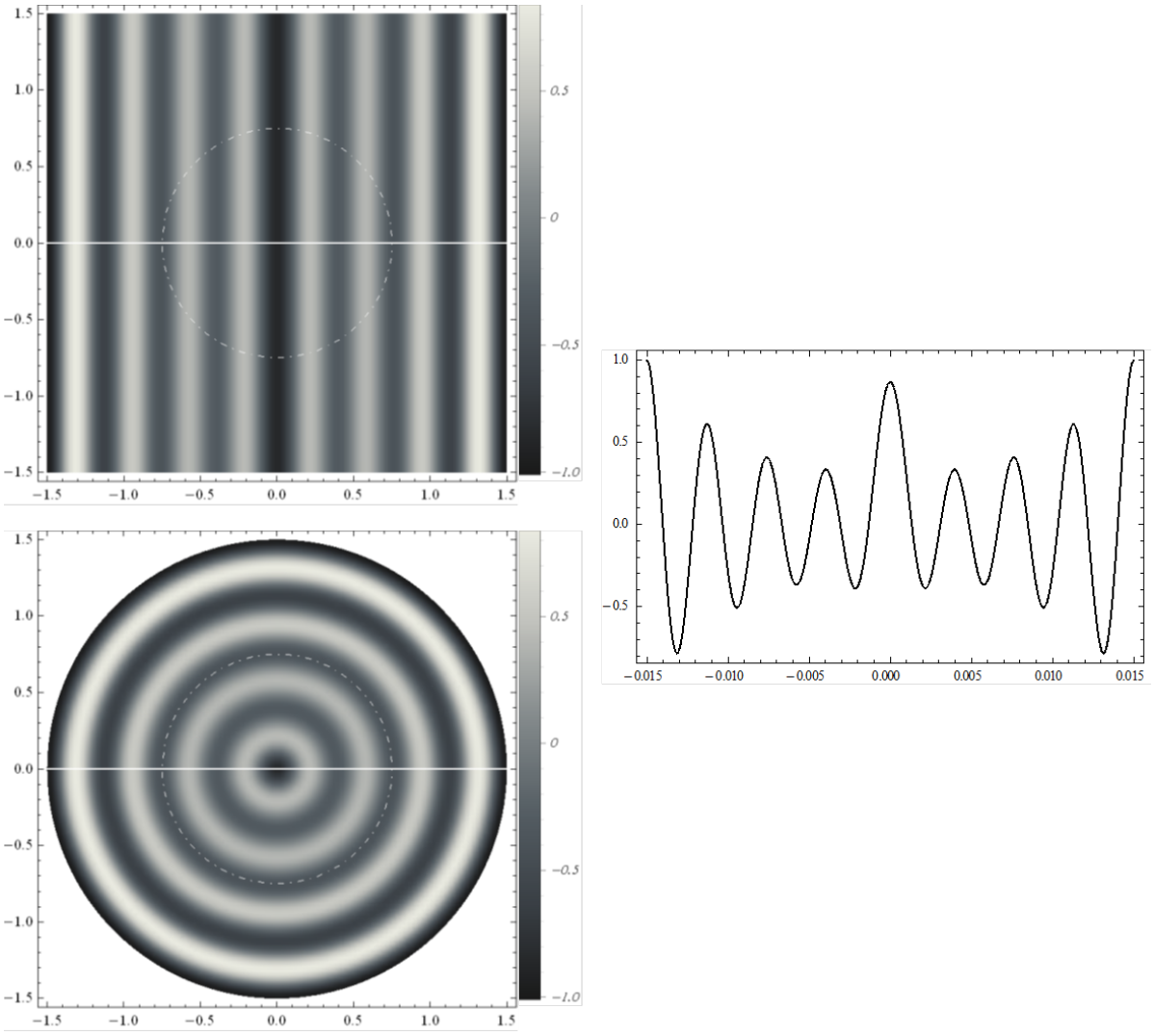

Figure 25. Wave field through a plane, containing the origin, parallel (top left) and perpendicular (bottom right) to the cylindrical axis. The line profile on the right comes from the white line on the wave fields. The complex shear moduli of the embedding medium and spherical inclusion are $\mu_1 = 7.5 - 1.5i$ kPa and $\mu_2 = 7.5 - 1.5i$ kPa, respectively.

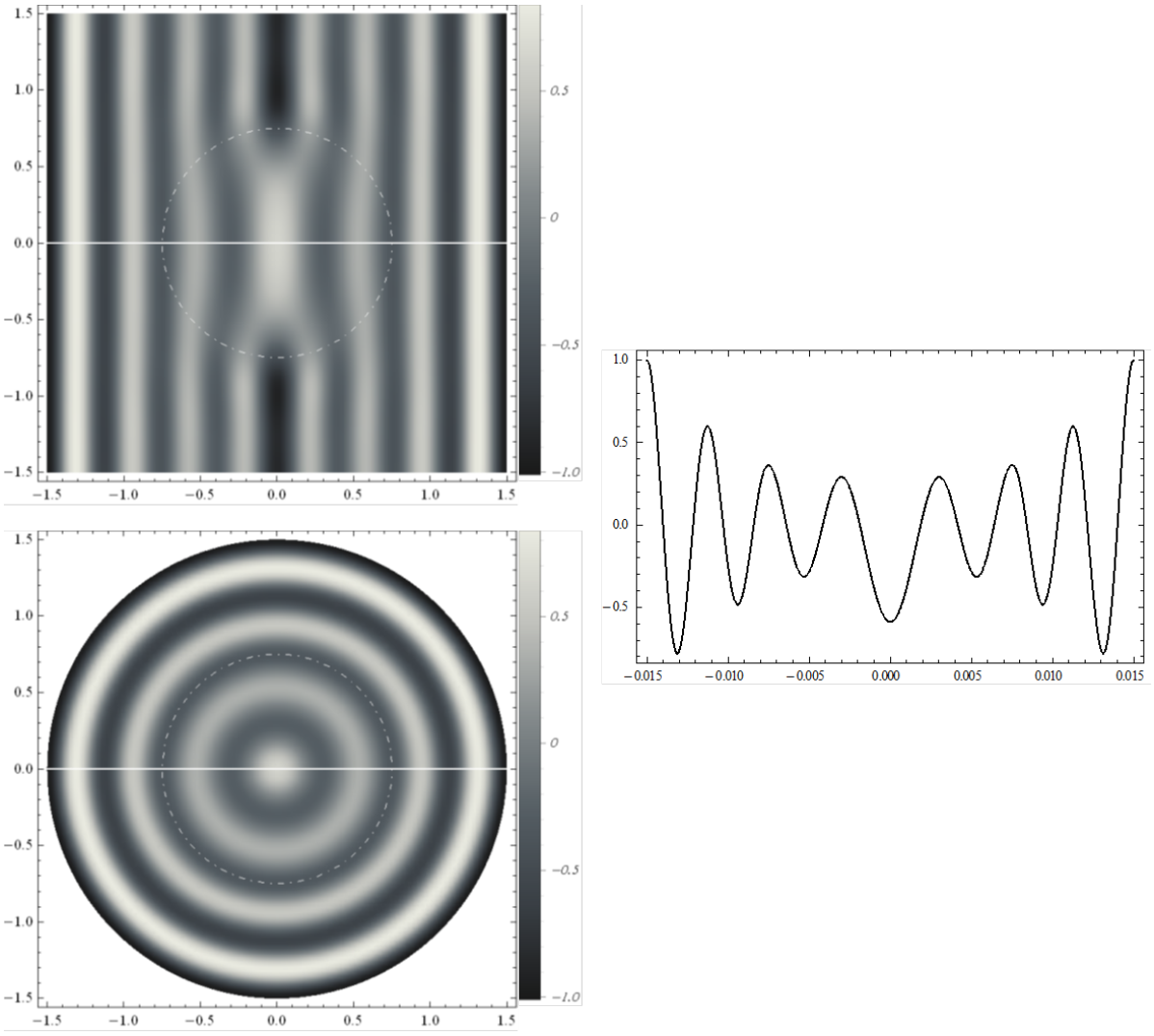

Figure 26. Wave field through a plane, containing the origin, parallel (top left) and perpendicular (bottom right) to the cylindrical axis. The line profile on the right comes from the white line on the wave fields. The complex shear moduli of the embedding medium and spherical inclusion are $\mu_1 = 7.5 - 1.5i$ kPa and $\mu_2 = 10 - 2i$ kPa, respectively.

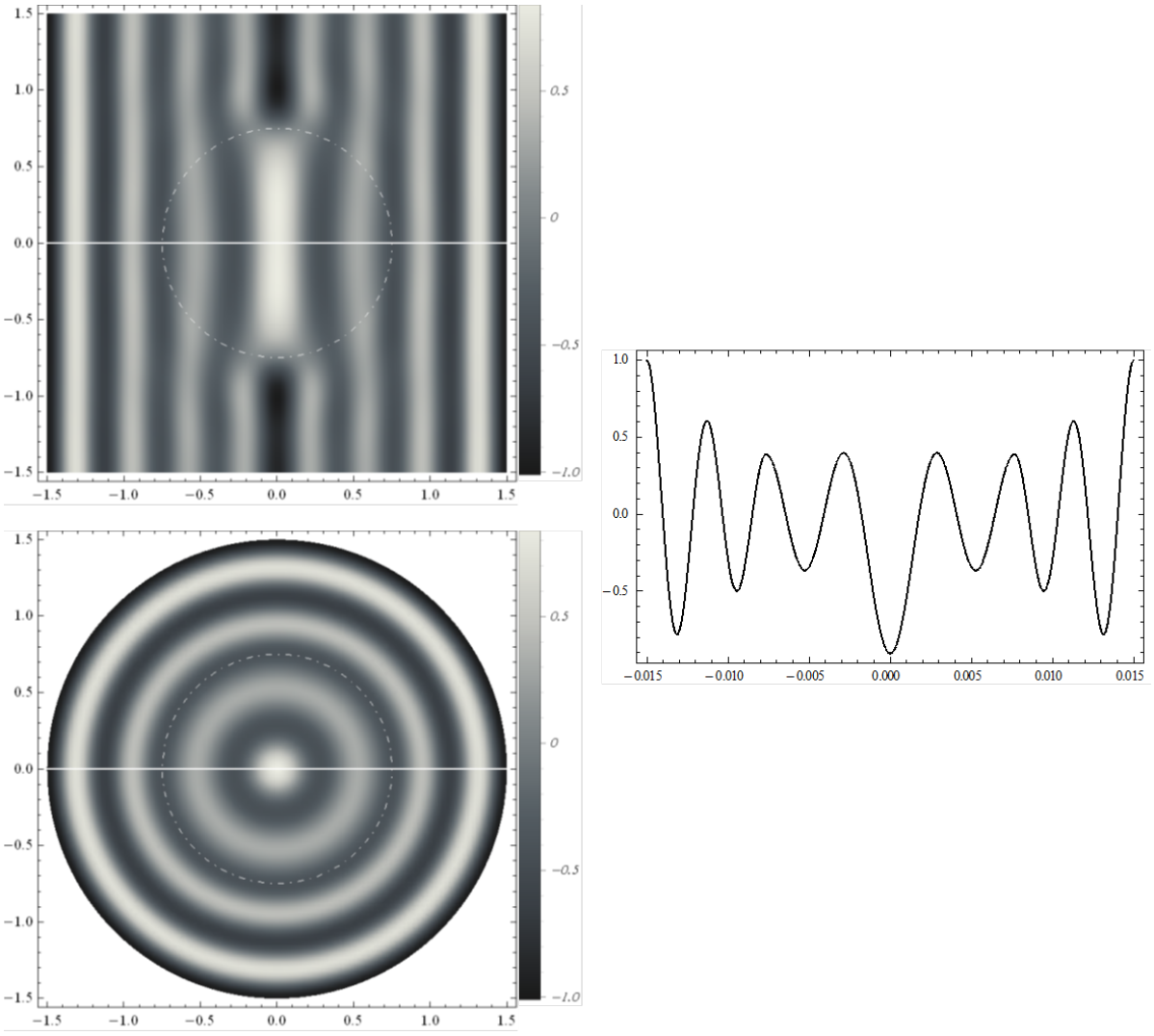

Figure 27. Wave field through a plane, containing the origin, parallel (top left) and perpendicular (bottom right) to the cylindrical axis. The line profile on the right comes from the white line on the wave fields. The complex shear moduli of the embedding medium and spherical inclusion are $\mu_1 = 7.5 - 1.5i$ kPa and $\mu_2 = 12.5 - 2.5i$ kPa, respectively.

3.6 Concluding Remarks

The scattering and diffraction of a radially-converging cylindrical elastodynamic harmonic wave on a finite elastic sphere is investigated in this chapter. An analytic solution is found by describing spherical and cylindrical waves in each others' coordinates, allowing satisfaction of the mixed boundary conditions. The expansion coefficients are expressed in terms of infinite sums of improper integrals. Both the sphere and embedding medium are modeled as being viscoelastic, i.e. their shear moduli have both real and imaginary components. Beside accurately describing the behavior of soft tissue, the assumption of viscoelasticity simplified the numeric evaluation of the improper integrals by moving the singularities and branch points off of the real axis, out of the path of integration.

This formalism need not be limited to biologic applications, or the integer-ordered calculus. Perhaps this work could be extended to enrich seismologic investigations of heterogeneities in the Earth, or cosmological studies of the interaction between black holes and gravitational fields of celestial bodies, or even the behavior of carbon nanotubes and cellular organelles. The other obvious extension is to generalize the orders of the calculus operators (79) used in the wave equation (80; 81) or the material properties (35), or both, to include the set of all complex numbers, $\mathbb{C}$, not just real integers, $\mathbb{N}$. There has been a non-trivial surge in interest in the fractional calculus of late, particularly in the biomedical sciences (41). It follows that the work presented in this article, given its underlying motivations, should be amenable to these calculus generalizations, that material properties and interactions may be similarly explored.

CHAPTER 4

SPHERICAL INCLUSION: EXPERIMENT

The increasing use of magnetic resonance (MR) elastography in biomedical research and clinical medicine has spurred much effort to optimize the sensitivity and specificity of the technique. Improvement in pulse sequence and actuator design have greatly reduced the overall imaging time and now provide multi-dimensional and multi-frequency data for elastographic reconstruction. One remaining question is the absolute accuracy of the material elasticity data (typically, the real and complex part of the elastic shear modulus). Cylindrical phantoms provide one way to validate system performance, but the simplified geometry and boundary conditions can cloak complexity arising at tissue interfaces. In an effort to develop a more realistic gel tissue phantom for MRE, a ball in tube gel phantom was constructed that allows one to vary the relative dimensions, elastic properties and water diffusion coefficient. The phantom was imaged and its stiffness determined using a 9.4 T horizontal MRE with a custom build piezo-elastic shear wave actuator (50-5,000 Hz). The resulting shear wave images were first compared with the theoretical model of chapter 3, and then used to reconstruct material stiffness maps for thin (1 mm) axial and transverse slices. The overall accuracy of the measurement process was assessed by comparing theory with experiment for selected values of the shear modulus (real and imaginary parts). The results validate the utility of this new phantom for use in animal and human MR elastography for system optimization and quality control.

4.1 Introduction

Many pathologies can be characterized by the changes they induce in the mechanical properties of tissue, e.g. cirrhotic liver is stiffer than healthy liver. This phenomenon has been exploited by physicians, since antiquity, to diagnose disease through the technique of palpation, wherein the physician manually feels for heterogeneities in a region of a patient's body by applying pressure thereupon. The obvious limitations of this are that an abnormally stiff region can be missed if it is too deep in the body and that the sense of touch of a doctor is highly subjective. Dynamic elastography seeks to answer this need, allowing for the non-invasive viscoelastic description of soft tissues by measuring the displacement fields from an applied stress (82). In MR elastography (6; 18; 19; 21) a harmonic shear wave is introduced in the tissue by an internal or external actuator. The scanner's motion-encoding gradient coils are synchronized with the mechanical actuator. The protons in these oscillating magnetic field accrue a phase shift corresponding to their displacement. The phase contrast image is analogous to a wave image from which the mechanical properties of the tissue, i.e. shear modulus, can be calculated. As with any imaging modality, phantom studies have been used to optimize MR elastography in terms of specificity and sensitivity.

4.1.1 Approximate Methods

Madsen et al showed how to construct agar/gelatin phantoms for long term stability of physical properties for use in both ultrasound and MR elastography studies. They were multiply connected, a cylinder through a cube (83), with the cylindrical inclusion being stiffer than the surrounding medium, and several evenly suspended spheres (84), also in a softer medium.

Perriñez et al made rectangular and cylindrical phantoms out of tofu (23), a bean curd made from soy, modeling the material as being poroelastic. Their finite element model (FEM), based on the theory of M. A. Biot (85), showed that poroelastic effects are non-trivial and should be considered when studying deformation of biomaterials, particularly in the context of MR elastography. The phantom study of Doyley et al (86) served to explore the use of the subzone inversion technique of Van Houten et al (87; 88) wherein the complex shear elastance of a material is obtained by solving the inverse problem from the displacement data using a FEM. Sack et al (89) used a simply connected heterogeneous phantom to demonstrate the effect of elastic heterogeneity on shear wave amplitudes. Though the two media are in intimate contact, they are in simple connection because one medium is not completely encased in the other as in those of Madsen et al (83; 84). Qin et al (32) used a phantom of several cylinders embedded throughout a disk parallel to its axis to demonstrate the possibility of acquiring MR elastography and diffusion tensor imaging simultaneously, while Yin et al (33) used a ball in tube phantom for combining MR elastography with diffusion-weighted imaging in a novel technique called Diffusion MRE (dMRE). Using the same type of phantom as Yin et al, Yaşar et al (42) compared wave images alone to show that it is possible to produce, with multifrequency MR elastography, wave images comparable to those obtained with conventional monofrequency scans, reducing, then, the scan time by a factor of 3.

4.1.2 Analytic Modeling

All of the above studies estimated the material parameters from the elastography data either with local frequency estimation of solving the inverse problem with a FEM. Yaşar et al (35)

used a closed form analytic solution to inverse model a tissue-mimicking simply connected, homogeneous, cylindrical phantom over a wide range of vibrational frequencies, showing that fractional order models capture best the complicated nature of viscoelastic material. Though Okamoto et al (36) used a closed form analytic solution to inverse model *multiply* connected soft gel phantoms, they were homogeneous. The actuator in their MR elastography set up was immersed in their cylindrical phantom whereas the phantoms used by Yaşar et al and Yin et al were vibrated by the very container holding them. There has been no study, then, of forward or inverse modeling of a heterogeneous multiply connected body in MR elastography using an analytic mathematical model. And, so, that is what is here now present in this chapter.

4.1.3 Objective

The entire derivation, solution, and numeric examples of the analytic solution of a sphere centrally embedded in an infinite circular cylinder can be found in chapter 3. The solution takes the form of an infinite sum of improper integrals, which is why it is only analytic, not closed form. The phantom construction, image acquisition, and parameter estimation techniques are then described. Experimental and theoretic results are compared, validating the model. Future research direction are then considered, including the relevance of this work in the context of medical imaging, tissue engineering, and mathematical modeling of complex physiologic systems.

4.2 Theory

The derivation, solution, and numeric examples of the problem of a ball in a tube can be found in chapter 3. Here the solution to just a tube is presented. Let there be given an

infinitely long, rigid, circular cylindrical tube on inner radius, b, filled with an elastic solid. This system is described by cylindrical coordinates (ρ,ϕ,z) (71), and shown in Figure 28. The rigid tube harmonically oscillates along the z axis and it is assumed that the elastic solid is in intimate contact with the oscillating wall. The displacement of the solid, $\vec{U}$, satisfies the vector Helmholtz equation (1),

$$\alpha^2 \nabla\nabla \cdot \vec{U} - \beta^2 \nabla \times \nabla \times \vec{U} + \omega^2 \vec{U} = 0 \tag{4.1}$$

where

$$\alpha^2 = (\lambda + 2\mu)\,\gamma^{-1}, \tag{4.2a}$$

and

$$\beta^2 = \mu\gamma^{-1}. \tag{4.2b}$$

The constants, λ and μ, are the Lame constants, and γ is the density of the material. It is held that $\lambda = (2\mu\nu)\,/\,(1-2\nu)$, where the Poisson ratio is $\nu = 0.4999998$ for both media. The harmonic time dependence, $e^{i\omega t}$, is suppressed throughout this study. The boundary condition at the radius, $\rho = b$, is equality of tangential displacement of the wall and elastic medium,

$$u(\rho, z)|_{\rho=b} = G \tag{4.3}$$

where G is the amplitude of the forced oscillations. The solution of Equation 4.1 can be given as the sum of the longitudinal, $\vec{L}$, and transverse components, $\vec{M}$ and $\vec{N}$. The motion is only

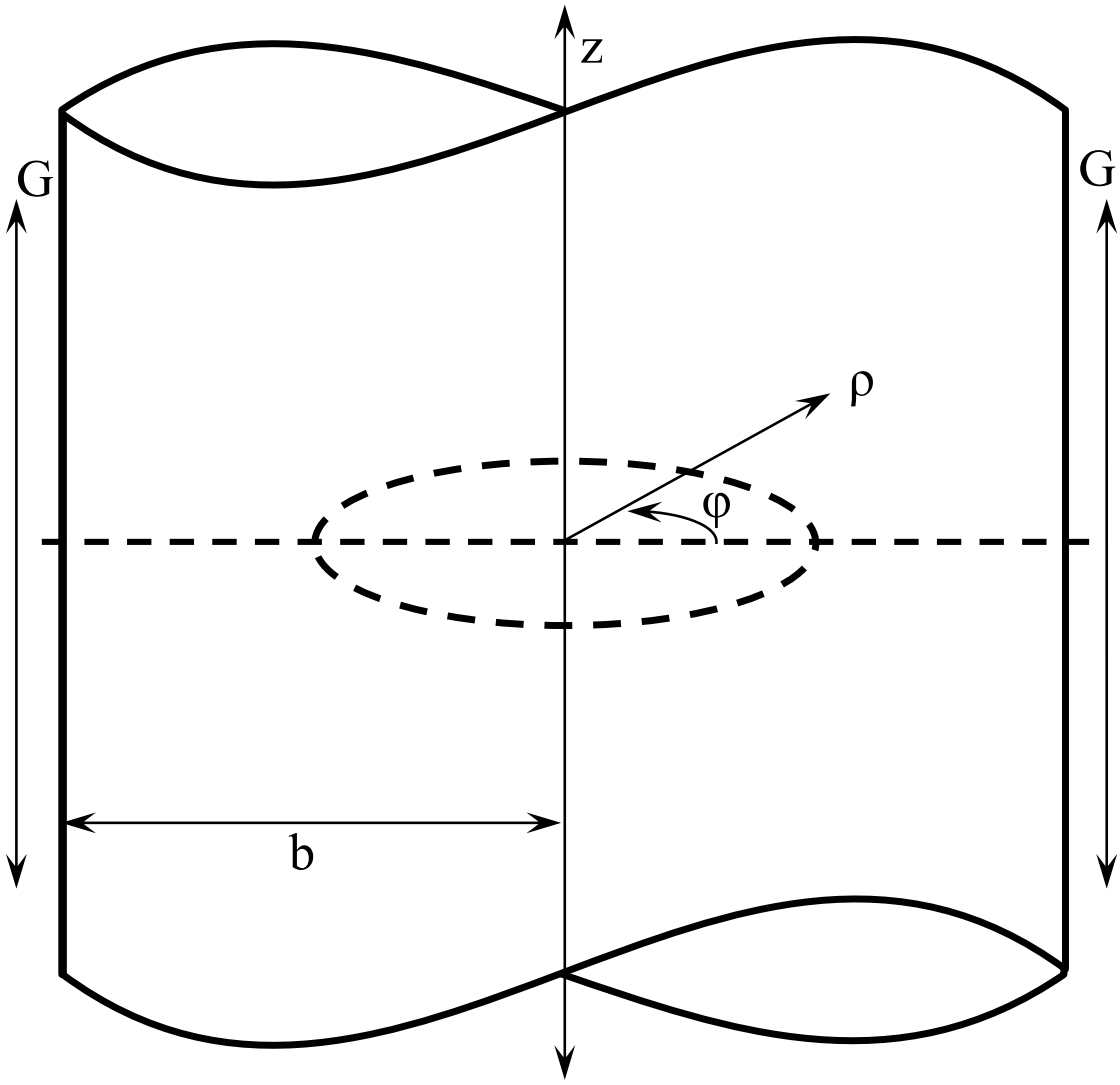

Figure 28. The cylindrical medium, medium 1, is referred to a cylindrical coordinate system, r and z, with the z axis coinciding with the axis of medium 1.

in the axial direction and there are no boundaries, e.g. a sphere, where mode conversion might occur, and, as before, this is an axially symmetric system, so, only $\vec{N}$ is of concern, given here, for convenience, as

$$\vec{N} = \beta^{-1}\nabla \times \nabla \times \hat{e}\mathrm{X}. \tag{4.4}$$

As before, X solves the scalar Helmholtz equation,

$$\left(\nabla^2 + \beta^{-2}\right)\mathrm{X} = 0, \tag{4.5}$$

and $\hat{e}$ is a constant vector (1). There is only an incidental field that cancels itself out at the origin. Again, for convenience and a sense of finality, $\vec{U} = \vec{N}$ is given as

$$\vec{U} = \vec{N} = \frac{1}{q\rho}\frac{\partial}{\partial\rho}\left(\rho\frac{\partial \mathrm{X}}{\partial\rho}\right)\hat{z}. \tag{4.6}$$

The solution to the scalar Helmholtz equation is achieved by the separation of variables,

$$\mathrm{X} = AJ_0(q\rho), \tag{4.7}$$

where

$$q = \frac{\omega}{\beta} \tag{4.8}$$

and A is the expansion coefficients, determined by the boundary condition, and J_0 is the Bessel function of the first kind of order zero (4). This analysis is restricted to the first kind because the

second kind and third kind (also call the Hankel function) are singular at the origin. Okamoto et al. made their solution unnecessarily complicated by not just starting with the Hankel function (36). Their domain didn't contain the origin while the domain here does. It is in the separation of variables where it becomes clear why the axial symmetry means always going to the cylindrical function of order zero. Putting Equation 4.7 in Equation 4.6 and setting $\rho = b$, one gets

$$-qJ_0(bq)A = G, \tag{4.9}$$

which is solved for A to get

$$A = -\frac{G}{qJ_0(bq)}, \tag{4.10}$$

making the closed form analytic solution for displacement

$$\vec{U}(\rho) = \frac{G}{qJ_0(bq)}J_0(q\rho). \tag{4.11}$$

4.3 Methods

4.3.1 Phantom Preparation

For a general frame of reference, magnitude MR images of the two phantoms used in this study are shown in Figure 29. The slight curvature on the bottom of the coronal images of both phantoms are imaging artifacts due to heterogeneities in the main magnetic field of the MRI scanner. The phantoms are actually flat in those regions.

4.3.1.1 Cylindrical Phantom

The phantom matrix was made from a mixture of agarose (SeaKem LE Agarose, Lonza, Rockland, ME) 0.75% by weight, and food grade gelatin (Knox Original Unflavored Gelatine, Kraft Foods Group Inc., Northfield, IL), 4% by weight, in water. The solution was heated until clarification occurred at 90 . The molten gel was poured into a cylindrical container made of an acetyl resin (Delrin, DSM Engineering Plastic Products, Inc., Reading, PA), and allowed to solidify at room temperature for 12 hours before being scanned.

4.3.1.2 Ball in Tube Phantom

The ball in tube phantom is identical to the cylindrical phantom save for the inclusion of a 1.7 cm diameter soft spherical inclusion (33). The procedure for making the surrounding agarose/gelatin gel (medium 1) is the same as presented above. The spherical inclusion (medium 2) was formed from dehydrated beads (Rainbow Water Beads, Greenville, SC) by immersion in distilled water for 8 hours. The are composed of a liquid crystalline polymer that absorbs water to form spherical beads of a hydrated gel. An individual bead was embedded in the center of the agarose/gelatin gel in the cylindrical container and allowed to gel at room temperature for 12 hours prior to the start of scanning.

4.3.2 Experimental Setup

MR elastography experiments were performed at 9.4 T using a horizontal bore Agilent small-animal MR scanner (310/ASR, Agilent Technologies, Santa Clara, CA) (33). A 39 mm diameter quadrature RF coil was used inside a 60 mm diameter gradient coil with a maximum gradient of 1000 G/m. The gel-filled container was placed horizontally inside the center of the RF coil.

TABLE VI

Parameters for data acquisition.

TR	1 s
TE	28 ms
FOV	4 cm × 4 cm
Matrix size	128 × 128
Slice thickness	1 mm
MSG	30 G/cm

the container was attached to a pre-loaded piezo-actuator (p-840.1, PhysikInstrumente (PI) GmbH & Co. KG, Germany), which generates the transverse vibration motion. All phantoms were scanned at the excitation frequencies of 250, 500, and 750 Hz. This experimental setup establishes concentric wave patterns within the gel.

4.3.3 Data Acquisition

A customized apin-echo (SE) based MR elastography sequence with a sinusoidal motion-sensitizing gradient (MSG) was used for data acquisition, obtaining one axial slice and one coronal slice. The acquisition parameters, summarized in Table VI, were as follows: repetition time (TR) = 1 s, echo time (TE) = 28 ms, field of view (FOV) = 4 cm × 4 cm, matrix size = 128 × 128, slice thickness = 1 mm, MSG = 30 G/cm. The number of MSG cycles varied with

the actuation frequency from 2 to 6 to accommodate constant TR/TE imaging parameters. In all scans, the MSG was applied along the principle direction of vibration in our experimental setup. Phase difference images were made from two acquisitions by inverting the polarity of the MSG. Four time steps were acquired per actuation cycle.

4.3.4 Data Processing

The raw phase images were unwrapped if wrapping artifacts were present, and Fourier transformed along the time axis over four time steps. The resulting complex wave images for each driving frequency were spatially filtered for noise reduction using a Gaussian filter. The wavelengths, l_i, were estimated using a 2D local frequency estimation (LFE) algorithm applied to the wave images (90). The shear stiffness maps were calculated from the following relation (91)

$$\mu_i = \gamma_i \left(l_i f\right)^2 . \tag{4.12}$$

Here γ_i is assumed to be to be the same as water, i.e. 1000 kg/m^3. At each frequency, the shear stiffness values were spatially averaged over regions of interest (ROIs) prescribed by the boundaries of the spherical inclusion visible in the MR elastography magnitude image or, in the case of the cylindrical phantom, by selection the region over the entire sample.

To compare the experimental to theoretic wave images, the forward problem had to be solved, i.e. calculate the displacement fields given certain mechanical inputs. The storage modulus, $\mathfrak{Re}\mu_i$, was obtained from the LFE while the loss modulus, $\mathfrak{Im}\mu_i$, was determined by trial-and-error comparisons of theoretic and experimental images. The estimated values of μ_1 and μ_2 were $7.5 - i0.5$ kPa and $1.9 - i0.5$ kPa, respectively. These inputs were used for all

frequencies in the forward modeling. All theoretic calculations were done on the computational software, Mathematica (Version 9, Wolfram Research, Inc., Champaign, IL). For comparison, the normalized analytic linear profiles were taken out of the experimental MR elastography wave image and the corresponding simulated wave image.

4.4 Results

The experimentally determined behavior of our phantoms is validated by comparing the experimental and theoretic displacement wave fields. Three excitations frequencies were chosen, 250, 500, and 750 Hz, to demonstrate validity. These frequencies were chosen for both experimental and computational reasons. The dimensions of the phantom and the dampening behavior of the viscoelastic material are limiting factors, experimentally. If the excitation frequency were too low, the wavelength would exceed the diameter of the cylinder. On the other hand, vibrating the cylinder too quickly would yield no discernible waves because of the preferential attenuation of high frequency mechanical waves. From a computational point of view, there is only an upper limit with regard to excitation frequency. The analytic solution of the ball in tube takes the form on an infinite sum of improper integrals which are truncated. The computation time required to evaluate the displacement goes with the degree of truncation, N, and N goes with the shear wave number, q_i. With the Mathematica code it took around 2 hours to render a 250 Hz wave field using a desktop computer running Windows 7 Ultimate–the processor was an Intel®Core$^{\text{TM}}$i5-2500K central processing unit at 3.30 GHz, with 7.71 usable GB of installed memory, and a 64-bit operating system–while a 750 Hz image took over 8 hours. The cylindrical and ball in tube phantoms are considered in turn.

4.4.1 Cylindrical Phantom

Figure 30 shows the analytic and experimental normalized displacements as seen in in the coronal plane through the center of the cylinder, i.e. parallel to the $\hat{z}$ axis and containing the origin. Close correspondence is seen between experimental and computed images, though there are differences between them. Most noticeably, it seems that the wave field is not perfectly uniform along the cylindrical $\hat{z}$ axis. For a more thorough comparison of theory to experiment the displacement field is examined through the axial plane, along the dashed lines in Figure 31. Figure 30 shows the analytic and experimental normalized displacements as seen in the axial plane through the center of the cylinder, i.e. perpendicular to the $\hat{z}$ axis and containing the origin. In Figure 32 the theoretic displacements along the dashed lines in Figure 30 are superimposed on the experimental displacements.

4.4.2 Ball in Tube Phantom

The results of the cylindrical phantom which contains a spherical heterogeneity that are analogous to those for the simple cylindrical phantom, i.e. coronal images, axial images, and linear profiles, are shown in Figure 34, Figure 33, and Figure 35, respectively. As with the simple cylindrical phantom, good agreement is found between the theoretic and experimental wave fields.

4.5 Discussion

While there is an obvious agreement between model and experiment it is not total and the differences are important to consider for they speak to the whole point of this study. The simple

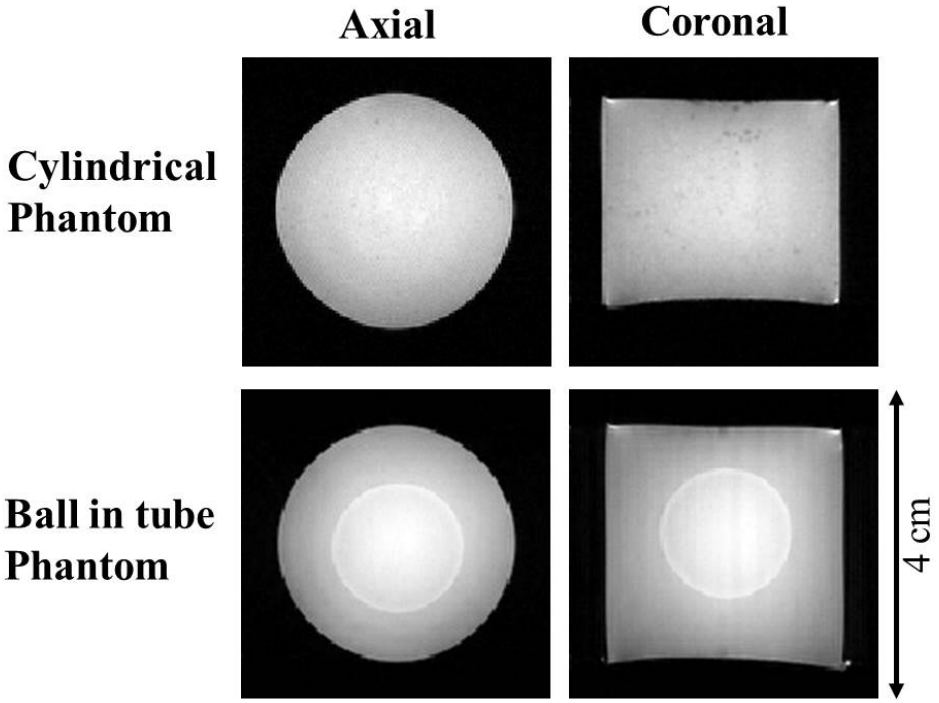

Figure 29. Magnitude images of the cylindrical (top) and ball in tube (bottom) phantoms. The left column is the axial plane through the center while the right column is the coronal plane, also through the center.

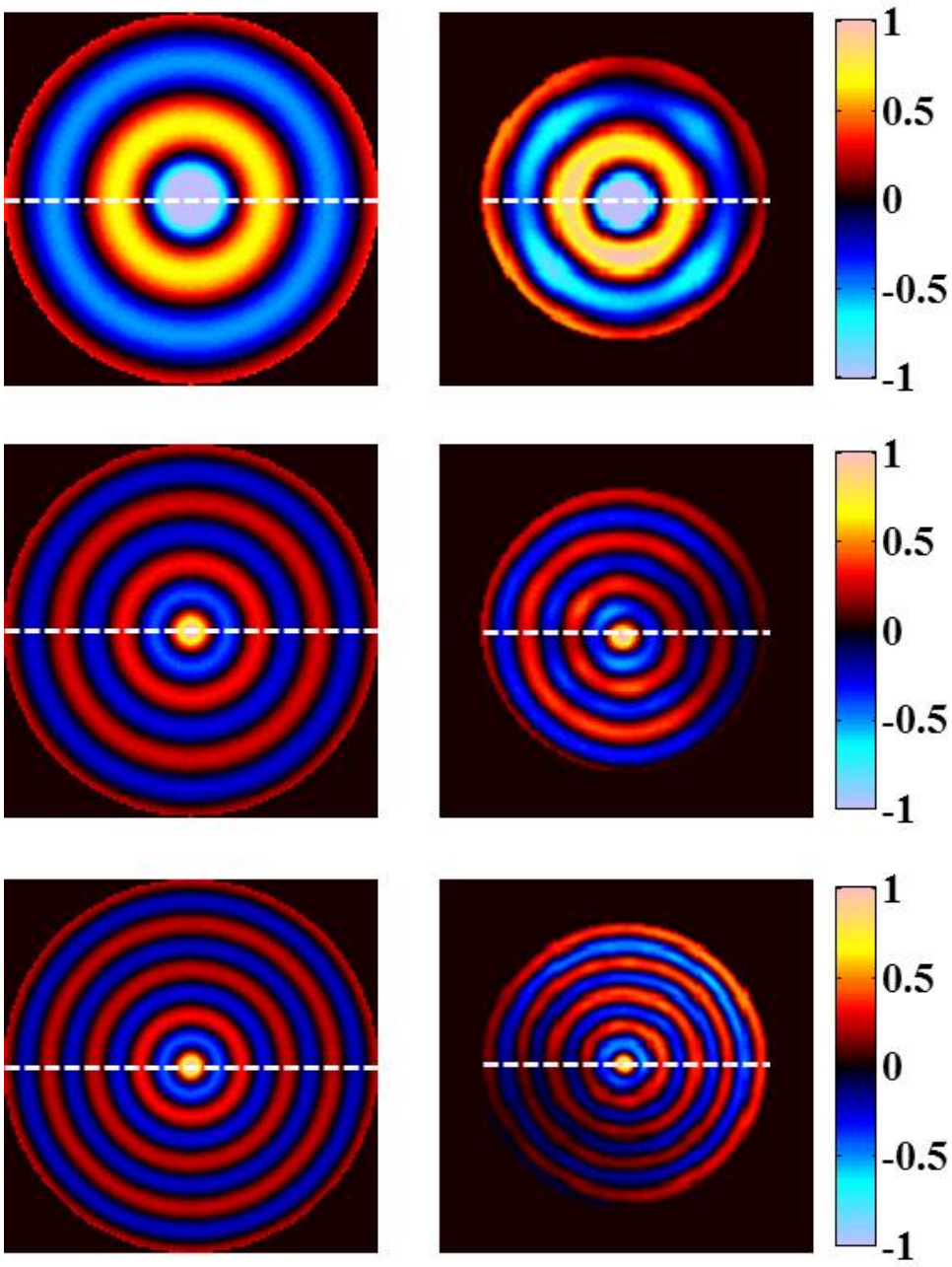

Figure 30. Theoretic (left) and experimental (right) wave field through the coronal plane, parallel to the cylindrical axis. The top, middle, and bottom rows correspond to excitation frequencies of 250, 500, and 750 Hz, respectively.

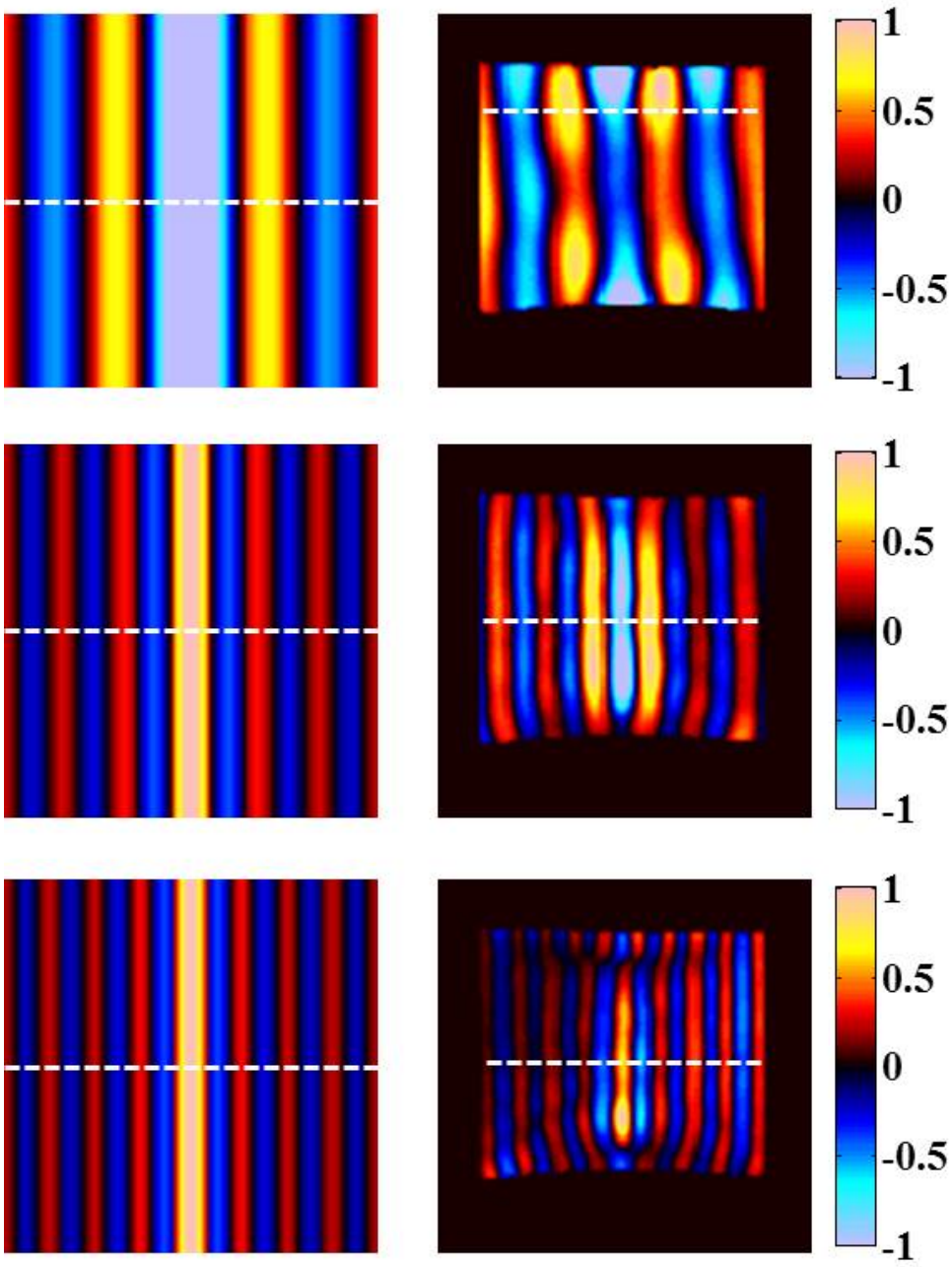

Figure 31. Theoretic (left) and experimental (right) wave field through the axial plane, perpendicular to the cylindrical axis. The top, middle, and bottom rows correspond to excitation frequencies of 250, 500, and 750 Hz, respectively.

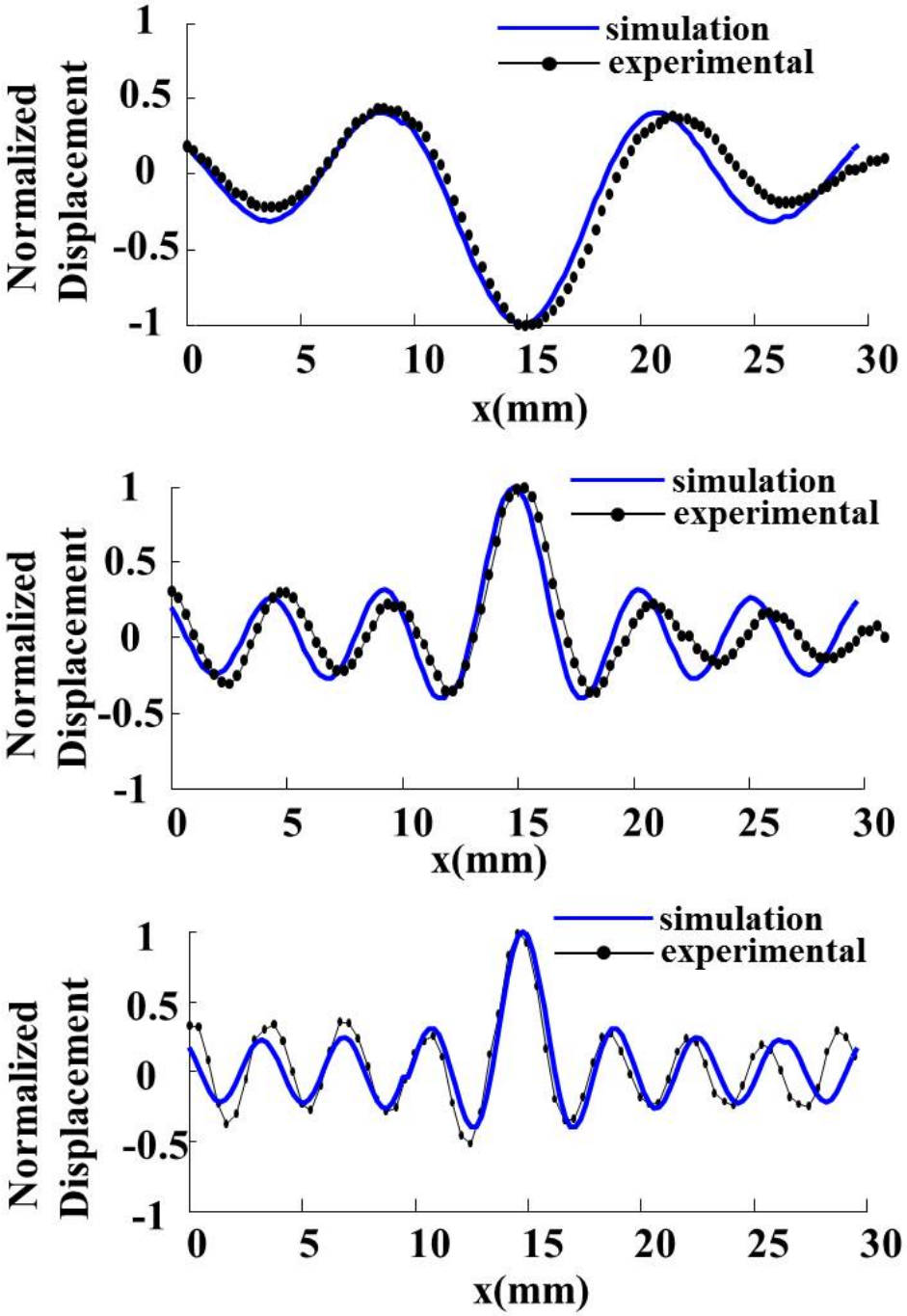

Figure 32. Comparison of the theoretic simulation and experimental displacements along the dotted white line indicated in Figure 30 and Figure 31.

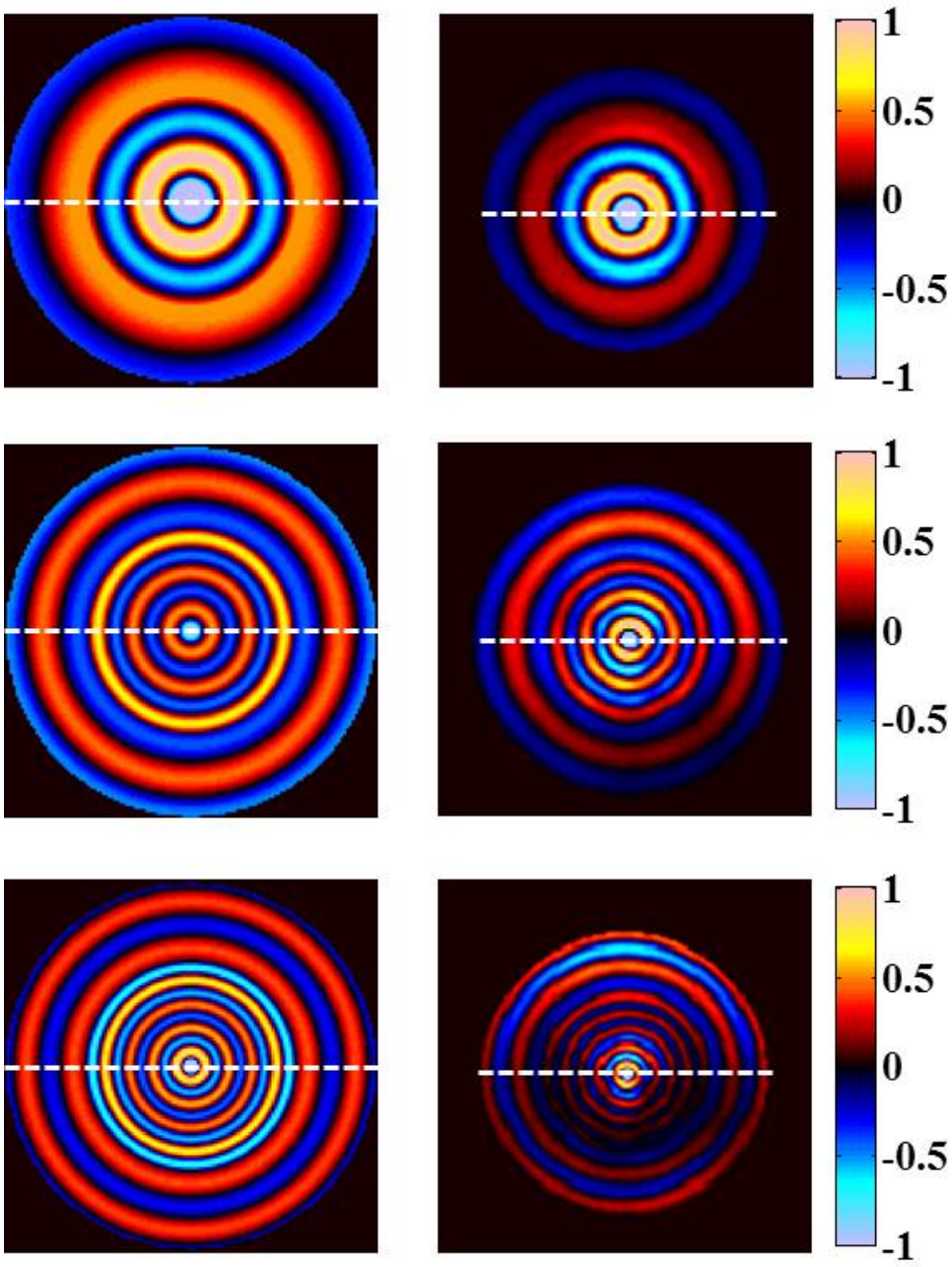

Figure 33. Theoretic (left) and experimental (right) wave field through the coronal plane, parallel to the cylindrical axis and containing the orthodrome of the spherical inclusion. The top, middle, and bottom rows correspond to excitation frequencies of 250, 500, and 750 Hz, respectively.

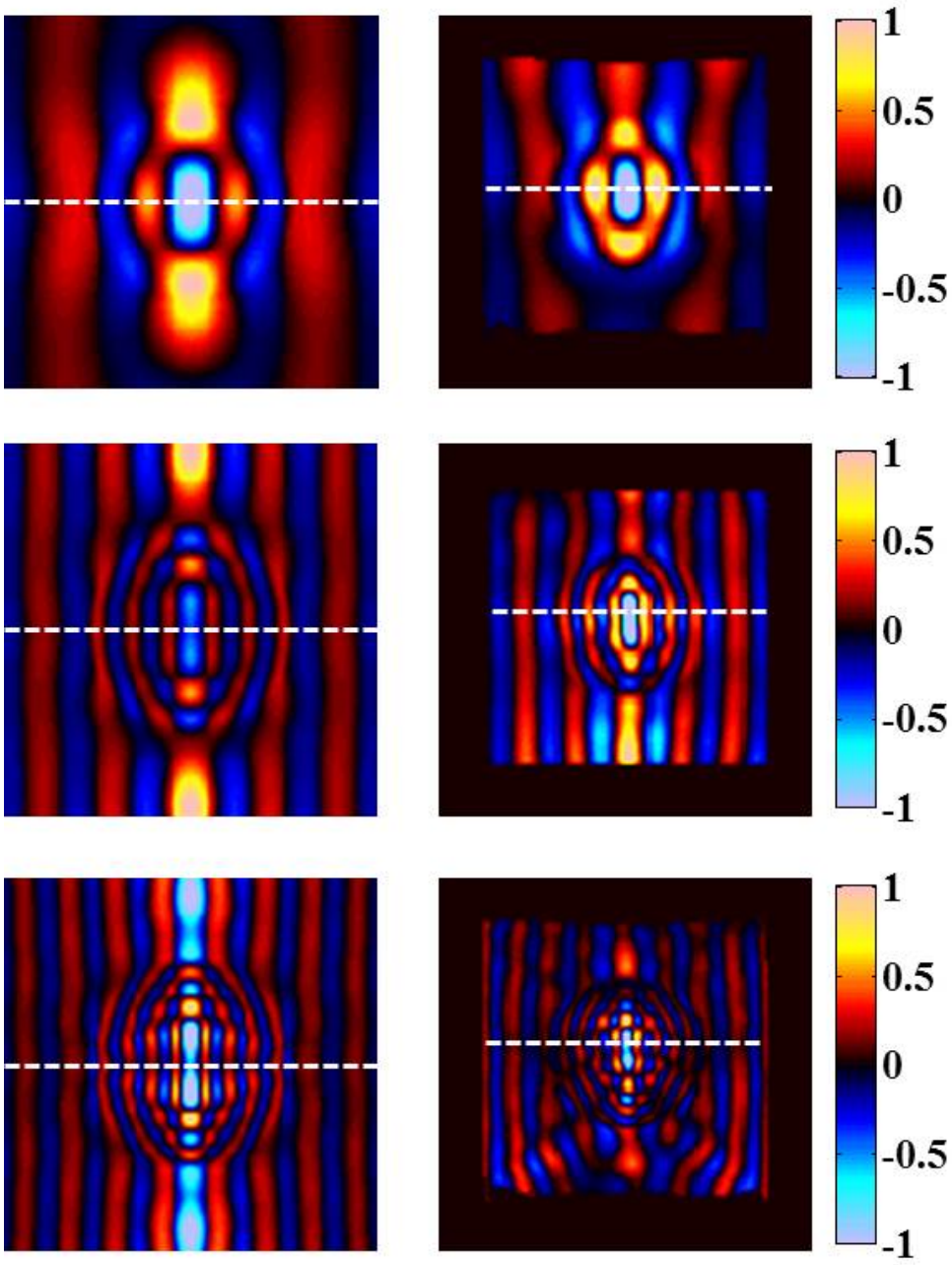

Figure 34. Theoretic (left) and experimental (right) wave field through the axial plane, perpendicular to the cylindrical axis and containing the orthodrome of the spherical inclusion. The top, middle, and bottom rows correspond to excitation frequencies of 250, 500, and 750 Hz, respectively.

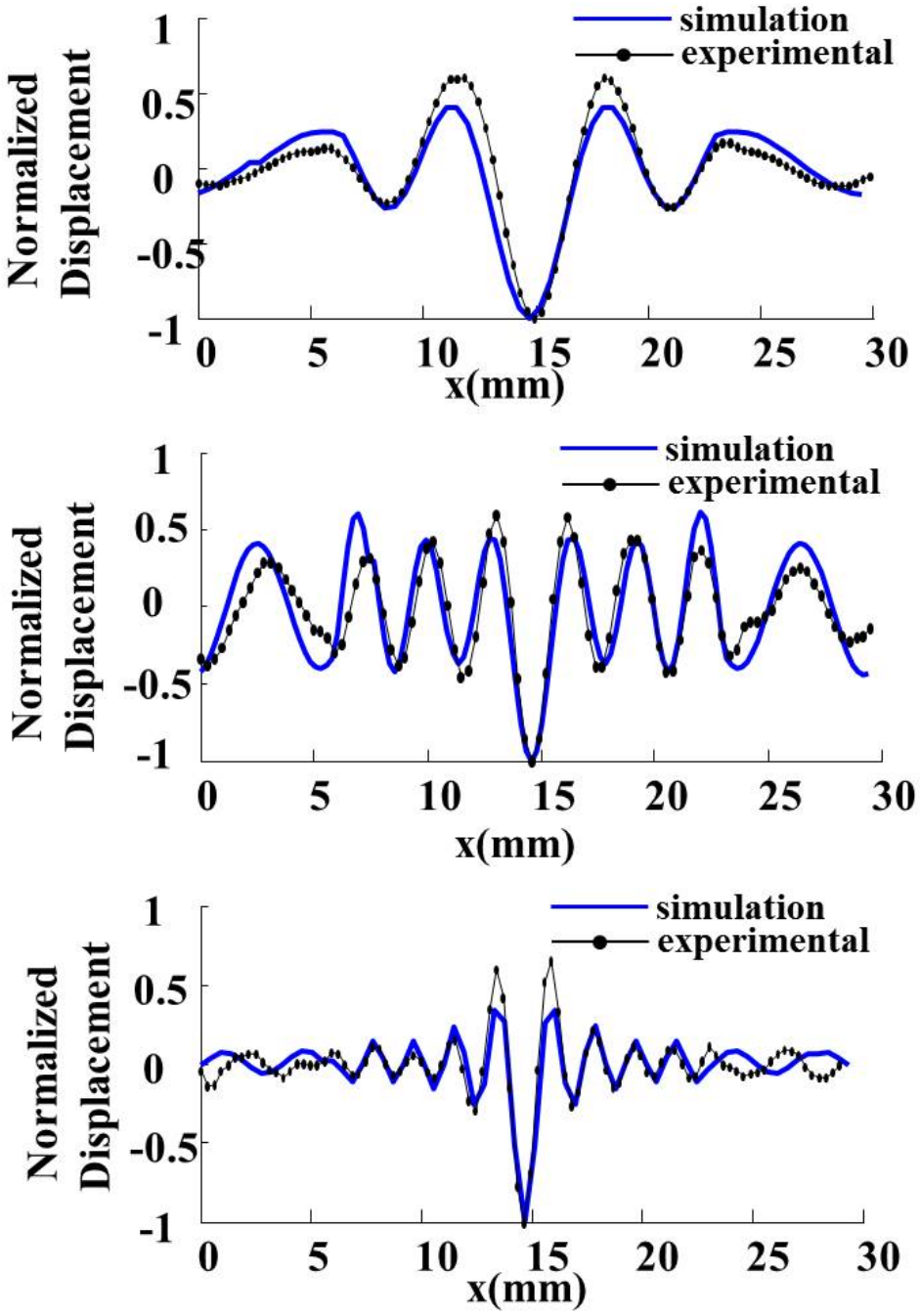

Figure 35. Comparison of the theoretic simulation and experimental displacements along the dotted white line indicated in Figure 33 and Figure 34.

cylindrical phantom is first discussed as that comparative analysis will inform the ball in tube discussion.

In the coronal view of the simple cylinder phantom (Figure 31) the vertically polarized waves are seen to be not perfectly straight up and down as the closed form analytic solution predicts they should be. This is more pronounced at the lower frequency, 250 Hz, than at 500 and 750 Hz. However, as the frequency goes up, the edge effects seem to play a larger role, i.e. the waves become distorted at the top and bottom of the cylinder. That highlights the key shortcoming of this model. It is assumed that the cylinder is infinitely long in the modeling. This limits the region, in which the models are of any predictive value, to the central region, clearly shown by the agreement found in the axial view (Figure 30) and the linear profiles (Figure 32). Even in that region, though, there isn't perfect consensus between theory and experiment. This is probably due to errors in estimation of the material's shear moduli, which are the inputs for the forward problem. Still, though, the discrepancy is toward the radial periphery of the phantom in all the frequencies. This is true in the multiply connected phantom, too.

As with the simple cylinder, in the case of the multiply connected ball in tube good agreement is found between the predicted wave field of the analytic solution and the experimentally obtained one, in the axially and radially central region. Again, the axial images and line profiles show this phenomenon (Figure 33 and Figure 35, respectively). Edge effects likely play a role in distorting the wave from the ideal, but in the ball in tube phantom there are two opportunities for miss-characterizing the shear moduli inputs, namely the embedding gel and the spherical heterogeneity. Adjusting, for instance, $\mathfrak{Im}\mu_2$, when solving the forward problem

to better match the experimental data will change the entire linear profile for the displacement of each region depends on the shear moduli of *both* regions. The next research step is to formulate the model of chapter 3 that it may be used to solve the inverse problem. For now we have validated the chapter 3 model with a custom built multiply connected hydrogel phantom. This is a non-trivial task. The chapter 3 model accounts for all wave fields through the interior of the viscoelastic solid, predicting very intricate wave patterns that were able to have been largely replicated. This opens the door to a new level of precision with regard to fine tuning all aspects of MR elastography, e.g. hardware, pulse sequences, etc.

This work also has the potential to enrich the field of tissue engineering. Spheres of sodium alginate are used as a scaffold on which to grow engineered cartilage and have already been successfully used to treat osteoarthritis (92). Magnetic resonance imaging parameters, e.g. T_1 and T_2, have shown promise as biomarkers to non-invasively monitor the grown and development of engineered tissue (93). Yet another was sought, i.e. the complex shear moduli.

4.6 Concluding Remarks

In this study the construction, testing, and analysis of an axially symmetric, heterogeneous, multiply connected hydrogel phantom was described in the context of MR elastography. The results were validated by comparison of the analytic solution of a similar albeit idealized geometry. Future work will include formulating the math that this phantom may be used for inverse modeling, investigating the behavior of a wider range of viscoelastic materials as etiher the ball or the tube, and generalizing the assumptions in the analytic solution to include all orders of the calculus operators (79; 41)

CHAPTER 5

CLOSING

We have reached the end of my original contributions to the fields of MR elastography and imaging in general. It certainly is not all there is to say on the matter nor indeed all that I have learned, but demonstrates my ability as a scientists, researcher, engineer.

5.1 Recapitulation

In the first study I designed, modeled, built, and tested a hydrogel phantom made of two centric cylinders of differing complex shear moduli. I showed that my mathematical analysis is useful for inverse modeling despite not perfectly modeling the phantom. In the second study I used multiple expansions to describe cylindrical and spherical waves in each others coordinate systems, that the problem of a ball in a tube may be solved analytically. This is the first time anyone has bothered with such a tedious mathematical analysis but probably will not be the last. In the third study we put the ball-in-tube model to work, solving the forward problem to validate the images we collected with out carefully designed ball-in-tube phantom.

5.2 Looking Forward

Let us now turn our gaze forward, and consider future work. It is true that more theory papers can be written by changing the ball-in-tube's boundary conditions, e.g. making the ball a spherical air pocket, but we can also change the shape of the inclusion from sphere to prolate or oblate spheroid (48; 94). The math would be not trivially different. I've only found two or so

papers relating cylinders and spheroids and they were in acoustic settings, so shear mechanical waves were not covered. Still, it is worth doing, I think. Another contribution stemming directly from this work is to add a vacuous third cylinder in the central cylinder in chapter 2. It could model a blood vessel and the surround tissue. Brinker et al have designed a concentric cylindrical phantom that allows for pre-stressing the elastic materials. I hope to adapt the work of Chapter 2 to include pre-stressed materials (95; 96; 97; 98). This work has many potential avenues to explore the effect of fractionalizing the calculus. At first I had wanted to analyze the growth of engineered tissue–spherical alginate beads seeded with chrondocites–and that is still a viable option. We can also apply fractional models to those tissues' rheological models as was done by Siegmar et al (99), Posnansky et al (100), and Guo et al (101). We could also investigate the effects of fractionalizing the dimensional space as it pertains to spheres and cylinders (102; 103).

5.3 Coda

I never though that I would be writing the end of a dissertation. I hope you liked it, my gentle floyds. I hope that you leaned something, that maybe you can take what is on these pages and apply it to your own work. I love to do science and I hope I have communicated at least that much. I hope to engender in others the sense of wonder and amazement I feel when I consider the fantastic mechanisms that govern the universe. Above all, I hope that I have contributed to the *healing* arts. That is, may this and all my work to follow be solely for the good of humankind.

CITED LITERATURE

1. Morse, P. and Feshbach, H.: Methods of Theoretical Physics, chapter 13, pages 1753–1901. International series in pure and applied physics. McGraw-Hill, 1953.

2. Moon, P. H. and Spencer, D. E.: Field Theory Handbook: Including Coordinate Systems, Differential Equations and Their Solutions, chapter Section 1, pages 12–17. Springer-Verlag, Berlin, 1961.

3. Haverman, R.: Applied Partial Differential Equations with Fourier Series and Boundary Value Problems, chapter 2, pages 35–88. Pearson Education, Inc., 2004.

4. Bell, W.: Special Functions for Scientists and Engineers, chapter 3 and 4, pages 42–155. Dover books on mathematics. Dover Publications, 2004.

5. Smith, N. and Webb, A.: Introduction to Medical Imaging: Physics, Engineering, and Clinical Applications, chapter 5, pages 204–281. Cambridge University Press, 2011.

6. Muthupillai, R., Lomas, D., Rossman, P., Greenleaf, J., Manduca, A., and Ehman, R.: Magnetic resonance elastography by direct visualization of propagating acoustic strain waves. Science, 269(5232):1854–1857, 1995.

7. Pauling, L. C.: General Chemistry, chapter 13, pages 475–477. Dover Publications, Inc., New York, 1988.

8. Everett, D. H.: Basic Principles of Colloid Science, chapter 13, pages 185–190. Royal Society of Chemistry, London, 1992.

9. Matsuhashi, T.: Agar. In Food Gels, ed. P. Harris, chapter 1, pages 1–51. Elsevier Science Publishing Ltd., 1990.

10. Johnston-Banks, F. A.: Gelatine. In Food Gels, ed. P. Harris, chapter 7, pages 233–289. Elsevier Science Publishing Ltd., 1990.

11. Watase, M. and Nishinari, K.: Rheological properties of agarose-gelatin gels. Rheologica Acta, 19(2):220–225, 1980.

12. Yang, F. and Zhu, K.-Q.: A note on the definition of fractional derivatives applied in rheology. Acta Mechanica Sinica, 27(6):866–876, 2011.

13. Brown, X. Q., Ookawa, K., and Wong, J. Y.: Evaluation of polydimethylsiloxane scaffolds with physiologically-relevant elastic moduli: interplay of substrate mechanics and surface chemistry effects on vascular smooth muscle cell response. Biomaterials, 26(16):3123–3129, 2005.

14. Palchesko, R. N., Zhang, L., Sun, Y., and Feinberg, A. W.: Development of polydimethylsiloxane substrates with tunable elastic modulus to study cell mechanobiology in muscle and nerve. PLOS ONE, 7(12):e51499, 2012.

15. Pfister, P. M., Wendlandt, M., Neuenschwander, P., and Suter, U. W.: Surface-textured peg-based hydrogels with adjustable elasticity: Synthesis and characterization. Biomaterials, 28(4):567–575, 2007.

16. Yaşar, T. K., Royston, T., and Magin, R.: Taking mr elastography (mre) to the microscopic scale (μmre). In 2011 IEEE International Symposium on Biomedical Imaging: From Nano to Macro, pages 1618–1623, March 2011.

17. Xie, H., Kim, K., Aglyamov, S. R., Emelianov, S. Y., ODonnell, M., Weitzel, W. F., Wrobleski, S. K., Myers, D. D., Wakefield, T. W., and Rubin, J. M.: Correspondence of ultrasound elasticity imaging to direct mechanical measurement in aging {DVT} in rats. Ultrasound in Medicine & Biology, 31(10):1351 – 1359, 2005.

18. Muthupillai, R., Rossman, P. J., Lomas, D. J., Greenleaf, J. F., Riederer, S. J., and Ehman, R. L.: Magnetic resonance imaging of transverse acoustic strain waves. Magnetic Resonance in Medicine, 36(2):266–274, 1996.

19. Muthupillai, R. and Ehman, R. L.: Magnetic resonance elastography. Nature Medicine, 2(5):601–603, 1996.

20. Plewes, D., Walker, C., and Foster, F.: Quantitative magnetic resonance imaging of ultrasound fields. In Ultrasonics Symposium, 1997. Proceedings., 1997 IEEE, volume 2, pages 1297–1300 vol.2, Oct 1997.

21. Walker, C., Foster, F., and Plewes, D.: Magnetic resonance imaging of ultrasonic fields. Ultrasound in Medicine & Biology, 24(1):137 – 142, 1998.

22. Doyley, M. M.: Model-based elastography: a survey of approaches to the inverse elasticity problem. Physics in Medicine and Biology, 57(3):R35–R73, 2012.

23. Perriñez, P., Kennedy, F., Van Houten, E., Weaver, J., and Paulsen, K.: Modeling of soft poroelastic tissue in time-harmonic mr elastography. Biomedical Engineering, IEEE Transactions on, 56(3):598–608, March 2009.

24. Othman, S. F., Xu, H., Royston, T. J., and Magin, R. L.: Microscopic magnetic resonance elastography (mre). Magnetic Resonance in Medicine, 54(3):605–615, 2005.

25. Othman, S. F., Zhou, X. J., Xu, H., Royston, T. J., and Magin, R. L.: Error propagation model for microscopic magnetic resonance elastography shear-wave images. Magnetic resonance imaging, 25(1):94–100, 2007.

26. Amador, C., Urban, M. W., Chen, S., Chen, Q., An, K.-N., and Greenleaf, J. F.: Shear elastic modulus estimation from indentation and sduv on gelatin phantoms. IEEE Transactions on Biomedical Engineering, 58(6):1706–1714, 2011.

27. Zhang, X., Qiang, B., and Greenleaf, J.: Comparison of the surface wave method and the indentation method for measuring the elasticity of gelatin phantoms of different concentrations. Ultrasonics, 51(2):157–164, 2011.

28. Henni, A. H., Schmitt, C., and Cloutier, G.: Three-dimensional transient and harmonic shear-wave scattering by a soft cylinder for dynamic vascular elastography. The Journal of the Acoustical Society of America, 124(4):2394–2405, 2008.

29. Schmitt, C., Hadj Henni, A., and Cloutier, G.: Ultrasound dynamic micro-elastography applied to the viscoelastic characterization of soft tissues and arterial walls. Ultrasound in medicine & biology, 36(9):1492–1503, 2010.

30. Schmitt, C., Hadj Henni, A., and Cloutier, G.: Characterization of blood clot viscoelasticity by dynamic ultrasound elastography and modeling of the rheological behavior. Journal of biomechanics, 44(4):622–629, 2011.

31. Doyley, M. M., Perreard, I., Patterson, A. J., Weaver, J. B., and Paulsen, K. M.: The performance of steady-state harmonic magnetic resonance elastography when applied to viscoelastic materials. Medical physics, 37(8):3970–3979, 2010.

32. Qin, E. C., Sinkus, R., Geng, G., Cheng, S., Green, M., Rae, C. D., and Bilston, L. E.: Combining mr elastography and diffusion tensor imaging for the assess-

ment of anisotropic mechanical properties: a phantom study. Journal of Magnetic Resonance Imaging, 37(1):217–226, 2013.

33. Yin, Z., Magin, R. L., and Klatt, D.: Simultaneous mr elastography and diffusion acquisitions: Diffusion-mre (dmre). Magnetic Resonance in Medicine, 71(5):1682–1688, 2014.

34. Khan, A. A., Dai, Z., Cortina, S., Chamon, W., and Royston, T. J.: Localized elastography map of human cornea through surface vibrations. In ASME 2013 International Mechanical Engineering Congress and Exposition, page V03BT03A049. American Society of Mechanical Engineers, 2013.

35. Yaşar, T. K., Royston, T. J., and Magin, R. L.: Wideband mr elastography for viscoelasticity model identification. Magnetic Resonance in Medicine, 70(2):479–489, 2013.

36. Okamoto, R. J., Clayton, E. H., and Bayly, P. V.: Viscoelastic properties of soft gels: comparison of magnetic resonance elastography and dynamic shear testing in the shear wave regime. Physics in Medicine and Biology, 56:6379–6400, 2011.

37. Mow, C. and Pao, Y.: Diffraction of Elastic Waves and Dynamic Stress Concentrations, chapter 3, pages 217–220. Rand Corporation research study. Crane, Russak, 1973.

38. Doublier, J. L., Launay, B., and Cuvelier, G.: Viscoelastic properties of food gels. In Viscoelastic Properties of Food, eds. M. A. Rao and J. F. Steffe, chapter 14, pages 371–434. Elsevier Science Publishing Ltd., 1992.

39. Muthukumar, M.: Dynamics of polymeric fractals. The Journal of chemical physics, 83(6):3161–3168, 1985.

40. Magin, R. L.: Fractional calculus models of complex dynamics in biological tissues. Computers & Mathematics with Applications, 59(5):1586–1593, 2010.

41. Magin, R.: Fractional Calculus in Bioengineering. Begell House Publishers, 2006.

42. Yaşar, T. K., Klatt, D., Royston, T. J., and Magin, R. L.: Selective spectral displacement for multifrequency mre. Physics in Medicine and Biology, 58:5771–5781, 2013.

43. Knight, R. C.: The potential of a sphere inside an infinite circular cylihnder. Quarterly Journal of Math (Oxford series), 7:124–133, 1936.

44. Kubenko, V. and Kruk, L.: Pulsating liquid flow past a spherical body in an infinite cylinder. International Applied Mechanics, 35(6):555–560, 1999.

45. Kubenko, V. and Dzyuba, V.: Resonant phenomena in a cylindrical shell containing a spherical inclusion and immersed in an elastic medium. International Applied Mechanics, 42(7):797–809, 2006.

46. Linton, C. M.: Multipole methods for boundary-value problems involving a sphere in a tube. IMA Journal of Applied Mathematics, 55(2):187–204, 1995.

47. Smythe, W. R.: Flow around a sphere in a circular tube. Physics of Fluids (1958-1988), 4(6):756–759, 1961.

48. Smythe, W. R.: Flow around a spheroid in a circular tube. Physics of Fluids (1958-1988), 7(5):633–638, 1964.

49. Cai, X. and Wallis, G. B.: Potential flow around a row of spheres in a circular tube. Physics of Fluids A: Fluid Dynamics (1989-1993), 4(5):904–912, 1992.

50. Ursell, F.: Trapped modes in a circular cylindrical acoustic waveguide. Proceedings of the Royal Society of London. Series A: Mathematical and Physical Sciences, 435(1895):575–589, 1991.

51. Linton, C. M.: Acoustic scattering by a sphere in a circular cylindrical waveguide. The Quarterly Journal of Mechanics and Applied Mathematics, 48(2):211–235, 1995.

52. Zhuk, A. P., Kubenko, V. D., and Zhuk, Y. A.: Acoustic radiation force on a spherical particle in a fluid-filled cavity. The Journal of the Acoustical Society of America, 132(4):2189–2197, 2012.

53. Lee, D.-S.: Scattering of torsional waves by a spherical cavity in a long circular elastic cylinder. Acta Mechanica, 164(1-2):47–59, 2003.

54. Golovchan, V.: Torsional waves in an elastic cylinder with spherical cavities. Soviet Applied Mechanics, 12(11):1112–1118, 1976.

55. Kubenko, V. and Dzyuba, V.: The acoustic field in a rigid cylindrical vessel excited by a sphere oscillating by a definite law. International Applied Mechanics, 36(6):779–788, 2000.

56. Kubenko, V. D. and Dzyuba, V. V.: Interaction between an oscillating sphere and a thin elastic cylindrical shell filled with a compressible liquid: internal axisymmetric problem. International Applied Mechanics, 37:222–230, 2001.

57. Kubenko, V. and Dzyuba, V.: Dynamic interaction of an oscillating sphere and an elastic cylindrical shell filled with a fluid and immersed in an elastic medium. International Applied Mechanics, 40(9):1002–1011, 2004.

58. Kubenko, V., Dzyuba, V., and Yansen, I.: Interaction of differently shaped bodies in a potential flow of perfect compressible fluid: Axisymmetric internal problem. International Applied Mechanics, 42(9):976–988, 2006.

59. Hasheminejad, S. M. and Hosseini, H.: Nonaxisymmetric interaction of a spherical radiator in a fluid-filled permeable borehole. International Journal of Solids and Structures, 45(1):24 – 47, 2008.

60. Hasheminejad, S. M. and Hosseini, H.: Dynamic interaction of a spherical radiator in a fluid-filled cylindrical borehole within a poroelastic formation. Mechanics Research Communications, 35(3):158 – 171, 2008.

61. Hosseini, H. and Namazi, N.: Acoustic scattering of spherical waves incident on a long fluid-saturated poroelastic cylinder. Acta Mechanica, 223(10):2075–2089, 2012.

62. Li, T. and Ueda, M.: Sound scattering of a spherical wave incident on a cylinder. The Journal of the Acoustical Society of America, 87(5):1871–1879, 1990.

63. Piquette, J. C.: Spherical wave scattering by an elastic solid cylinder of infinite length. The Journal of the Acoustical Society of America, 79(5):1248–1259, 1986.

64. Ström, S.: Introduction to integral representations and integral equations for time-harmonic acoustic, electromagnetic and elastodynamic wave fields. In Field Representations and Introduction to Scattering, eds. V. Varadan, A. Lakhtakia, and V. Varadan, Mechanics and Mathematical Methods. North-Holland, 1991.

65. Waterman, P. C.: Matrix theory of elastic wave scattering. The Journal of the Acoustical Society of America, 60(3):567–580, 1976.

66. Olsson, S.: Transmission and reflection of elastic waves by a spherical obstacle in an infinite circular cylindrical rod. The Quarterly Journal of Mechanics and Applied Mathematics, 47(4):583–606, 1994.

67. Olsson, S.: Point force excitation of an elastic infinite circular cylinder with an embedded spherical cavity. The Journal of the Acoustical Society of America, 93(5):2479–2488, 1993.

68. Olsson, S.: Point force excitation of a thick-walled elastic infinite pipe with an embedded inhomogeneity. Journal of Engineering Mathematics, 28(4):311–325, 1994.

69. Kim, J. I., Schmiedmayer, J., and Schmelcher, P.: Quantum scattering in quasi-one-dimensional cylindrical confinement. Phys. Rev. A, 72:042711, Oct 2005.

70. Otey, C. and Fan, S.: Numerically exact calculation of electromagnetic heat transfer between a dielectric sphere and plate. Physical Review B, 84(24):245431, 2011.

71. Chree, C.: The equations of an isotropic elastic solid in polar and cylindrical co-ordinates, their solution and application. Proceedings of the Cambridge Philosophical Society, Mathematical and physical sciences, 14:250–369, 1889.

72. Mow, C. and Pao, Y.: Diffraction of Elastic Waves and Dynamic Stress Concentrations, chapter 6, pages 601–612. Rand Corporation research study. Crane, Russak, 1973.

73. Erofeenko, V. T.: Relations between main solutions of helmholtz and laplace equations in spherical and cylindrical coordinates. Proc. Natl. Acad. Sci. Belorussian SSR, 4:42–46, 1972. in Russian.

74. Han, G., Han, Y., and Zhang, H.: Relations between cylindrical and spherical vector wavefunctions. J. Opt. A: Pure Appl. Opt., 10:[Art 015006], 2008.

75. Pogorzelski, R. J. and Lun, E.: On the expansion of cylindrical vector waves in terms of spherical vector waves. Radio Science, 11(10):753–761, 1976.

76. Graff, K.: Wave Motion in Elastic Solids, chapter 7, pages 400–407. Dover Books on Engineering Series. Dover Publications, 1975.

77. Dixon, A. C.: On a class of matrices of infinite order and on the existence of "matricial" functions on a riemann surface. Transactions of the Cambridge Philosophical Society, 19:190–233, 1904.

78. Silverman, R. A.: Introductory Complex Analysis, chapter 12, pages 247–269. Dover books on advanced mathematics. Dover Publications, 1972.

79. Oldham, K. B. and Spanier, J.: The Fractional Calculus: Theory and Applications of Differentiation and Integration to Arbitrary Order. Dover Publications, Inc., 2006.

80. Holm, S. and Näsholm, S. P.: A causal and fractional all-frequency wave equation for lossy media. The Journal of the Acoustical Society of America, 130(4):2195–2202, 2011.

81. Näsholm, S. P. and Holm, S.: Linking multiple relaxation, power-law attenuation, and fractional wave equations. The Journal of the Acoustical Society of America, 130(5):3038–3045, 2011.

82. Sarvazyan, A., Hall, T. J., Urban, M. W., Fatemi, M., Aglyamov, S. R., and Garra, B. S.: An overview of elastography–an emerging branch of medical imaging. Current Medical Imaging Reviews, 7(4):255–282, 2011.

83. Madsen, E. L., Hobson, M. A., Shi, H., Varghese, T., and Frank, G. R.: Tissue-mimicking agar/gelatin materials for use in heterogeneous elastography phantoms. Physics in medicine and biology, 50(23):5597, 2005.

84. Madsen, E. L., Frank, G. R., Hobson, M. A., Shi, H., Jiang, J., Varghese, T., and Hall, T. J.: Spherical lesion phantoms for testing the performance of elastography systems. Physics in medicine and biology, 50(24):5983, 2005.

85. Biot, M. A.: Theory of propagation of elastic waves in a fluid-saturated porous solid. The Journal of the Acoustical Society of America, 28(2):168–191, 1956.

86. Doyley, M. M., Van Houten, E. E., Weaver, J. B., Poplack, S., Duncan, L., Kennedy, F., and Paulsen, K. D.: Shear modulus estimation using parallelized partial volumetric reconstruction. IEEE Transactions on Medical Imaging, 23(11):1404–1416, 2004.

87. Van Houten, E., Paulsen, K., Miga, M., Kennedy, F., Weaver, J., et al.: An overlapping subzone technique for mr-based elastic property reconstruction. Magnetic Resonance in Medicine, 42(4):779–786, 1999.

88. Van Houten, E. E., Miga, M. I., Weaver, J. B., Kennedy, F. E., and Paulsen, K. D.: Three-dimensional subzone-based reconstruction algorithm for mr elastography. Magnetic Resonance in Medicine, 45(5):827–837, 2001.

89. Sack, I., Rump, J., Elgeti, T., Samani, A., and Braun, J.: Mr elastography of the human heart: noninvasive assessment of myocardial elasticity changes by shear wave amplitude variations. Magnetic Resonance in Medicine, 61(3):668–677, 2009.

90. Knutsson, H., Westin, C.-F., and Granlund, G.: Local multiscale frequency and bandwidth estimation. In Image Processing, 1994. Proceedings. ICIP-94., IEEE International Conference, volume 1, pages 36–40. IEEE, 1994.

91. Manduca, A., Oliphant, T. E., Dresner, M., Mahowald, J., Kruse, S., Amromin, E., Felmlee, J. P., Greenleaf, J. F., and Ehman, R. L.: Magnetic resonance elastography: non-invasive mapping of tissue elasticity. Medical image analysis, 5(4):237–254, 2001.

92. Almqvist, K. F., Dhollander, A. A. M., Verdonk, P. C. M., Forsyth, R., Verdonk, R., and Verbruggen, G.: Treatment of cartilage defects in the knee using alginate beads containing human mature allogenic chondrocytes. The American Journal of Sports Medicine, 37(10):1920–1929, 2009.

93. Xu, H., Othman, S. F., and Magin, R. L.: Monitoring tissue engineering using magnetic resonance imaging. Journal of bioscience and bioengineering, 106(6):515–527, 2008.

94. Cooke, J. C.: Some relations between bessel and legendre functions. Monatshefte für Mathematik, 60(4):322–328, 1956.

95. Tang, S.: Wave propagation in initially-stressed elastic solids. Acta Mechanica, 4(1):92–106, 1967.

96. Tolstoy, I.: On elastic waves in prestressed solids. Journal of Geophysical Research: Solid Earth (1978–2012), 87(B8):6823–6827, 1982.

97. Wijeyewickrema, A., U. Y. and Kayestha, P.: Wave propagation in a prestressed compressible elastic layer with constrained boundaries. Journal of Mechanics of Materials and Structures, 3(10):1963–1976, 2008.

98. Brinker, S., Kearney, S., Royston, T., and Klatt, D.: Effects of quasistatic internal pressure loads on a multi-layered pressure vessel phantom in mr elastography. In 16th International Conference on Experimental Mechanics. European Society for Experimental Mechanics, 2014. in press.

99. Kempfle, S., Schäfer, I., and Beyer, H.: Fractional calculus via functional calculus: theory and applications. Nonlinear Dynamics, 29(1-4):99–127, 2002.

100. Posnansky, O., Guo, J., Hirsch, S., Papazoglou, S., Braun, J., and Sack, I.: Fractal network dimension and viscoelastic powerlaw behavior: I. a modeling approach based on a coarse-graining procedure combined with shear oscillatory rheometry. Physics in medicine and biology, 57(12):4023–4040, 2012.

101. Guo, J., Posnansky, O., Hirsch, S., Scheel, M., Taupitz, M., Braun, J., and Sack, I.: Fractal network dimension and viscoelastic powerlaw behavior: Ii. an experimental study of structure-mimicking phantoms by magnetic resonance elastography. Physics in Medicine and Biology, 57(12):4041–4053, 2012.

102. Hussain, A., Ishfaq, S., and Naqvi, Q. A.: Fractional curl operator and fractional waveguides. Progress In Electromagnetics Research, 63:319–335, 2006.

103. Zubair, M., Mughal, M. J., and Naqvi, Q. A.: An exact solution of the cylindrical wave equation for electromagnetic field in fractional dimensional space. Progress In Electromagnetics Research, 114:443–455, 2011.

104. Kubenko, V. and Dzyuba, V.: Diffraction of a plane acoustic wave by a rigid sphere in a cylindrical cavity: An axisymmetric problem. International Applied Mechanics, 45(4):424–432, 2009.

105. Oudry, J., Chen, J., Glaser, K. J., Miette, V., Sandrin, L., and Ehman, R. L.: Cross-validation of magnetic resonance elastography and ultrasound-based transient elastography: A preliminary phantom study. Journal of Magnetic Resonance Imaging, 30(5):1145–1150, 2009.

106. Palmeri, M. L., McAleavey, S. A., Fong, K. L., Trahey, G. E., and Nightingale, K. R.: Dynamic mechanical response of elastic spherical inclusions to impulsive acoustic radiation force excitation. Ultrasonics, Ferroelectrics and Frequency Control, IEEE Transactions on, 53(11):2065–2079, 2006.

VITA

Education

- Ph.D. in Bioengineering, 2014, University of Illinois at Chicago
- M.S. in Bioengineering, 2009, University of Vermont
- B.S.E. in Bioengineering, 2006, Arizona State University

Abstracts

- **Benjamin L. Schwartz**, and Jason H. T. Bates "Multi-compartment modeling of heterogeneity during bronchoconstriction in mice." Poster session presented at: Annual Meeting of the Biomedical Engineering Society. October 2008, St. Louis, MO.
- **Benjamin L. Schwartz**, Lara Ansari, Heta Chokshi, Lora Gjoni, and Richard L. Magin. "Diffraction of a Cylindrical Wave by an Elastic Sphere Embedded in a Cylindrical Elastic Medium: An Axisymmetric Problem." Poster session presented at: Annual Meeting of the Biomedical Engineering Society. October 2012, Atlanta, GA.
- **Benjamin L. Schwartz**, Shelley Kerwell, Vivian Sandoval, Kruti Shah, Kaya Yaşar, and Richard L. Magin. "New Phantoms for Evaluating micro-Magnetic Resonance Elastography (μMRE)." Poster session presented at: Annual Meeting of the Biomedical Engineering Society. September 2013, Seattle, WA.

Papers

- **Benjamin L. Schwartz**, Ron C. Anafi, Minara Aliyeva, John A. Thompson-Figueroa, Gilman B. Allen, Lennart K. A. Lundblad, and Jason H. T. Bates. "Effects of Central Airway Shunting on the Mechanical Impedance of the Mouse Lung." *Ann Biomed Eng*, January 2011, 39(1):497-507.
- **Benjamin L. Schwartz**, Yifei Liu, Thomas J. Royston, and Richard L. Magin. "Difraction of a cylindrical transverse wave by an elastic spherical inclusion: an axisymmetric problem." *J Acoust Soc Am*, In Review.
- **Benjamin L. Schwartz**, Ziying Yin, Temel K. Yaşar, Yifei Liu, Altaf A. Khan, Allen Q. Ye, and Richard L. Magin. "Inverse modeling of concentric cylindrical phantom with MR elastography." *IEEE Trans Biomed Eng*, In Preparation.
- **Benjamin L. Schwartz**, Ziying Yin, and Richard L. Magin. "Comparison of theoretic and experimental models for elastodynamic wave propagation in gel tissue phantoms." *Phys Med Biol*, In Preparation.